# DIFFUSION AND MOLECULAR ASSOCIATION IN ARTIFICIAL PROTEIN HYDROGELS

Thesis by

Peter B. Rapp

In Partial Fulfillment of the Requirements

*for the degree of*

Doctor of Philosophy in Chemical Engineering


CALIFORNIA INSTITUTE OF TECHNOLOGY

Pasadena, California

2017

(Defended May 31, 2017)

Peter B. Rapp
ORCID: 0000-0002-9586-2126

*To Kara*:

Some bonds are not reversible.

# ACKNOWLEDGEMENTS

First and before anyone else, to my wife Kara: you are without equal. You handle all seasons, situations and stress levels of your husband with stability, grace, warmth, and encouragement. Without you I am nothing. Likening our marriage to the midblock of a telechelic polymer, I am the dangling chain end and you keep me tethered to the network called home, saving me from the perilous free state of bachelordom. An asymmetric distribution of labor permits me to still indulge in these itinerant musings.

I feel tremendously grateful for the opportunity to have studied at Caltech, a place that I believe stands as one of the best institutes dedicated to knowledge and scientific discovery of the most rigorous and fundamental kind. This institute is made truly remarkable by its people, many of whom have shaped me in meaningful ways that I did not expect. This short list of some of them does not sufficiently express the appreciation, admiration and respect that I have for them and many others who will go unmentioned.

David Tirrell has been an unforgettable advisor, scientific role model, and friend. He is the best kind of mentor and scientist there is: humble, creative, patient, easy to please and impossible to satisfy. He has always cheerfully supported my impulsive experimental undertakings, and has always been there when I needed him. None other than Jesus Himself said that “a student is not above his teacher, but everyone when he is fully trained will be like his teacher”. If the latter is at all applicable to my present situation then I am very lucky.

Among those who contributed directly to this work, Ahmad Omar has been a wonderful contributor, and I am indebted to him for his deep theoretical insights. It is thanks to Dave’s

patience, and Ahmad's rigor, that the novel theory presented in Chapter 2 was born. Bradley Silverman was an enthusiastic contributor to many experimental aspects of the FRAP work, and the data-sets we generated together were so large that I literally could not have examined them had he not also written several powerful scripts for high-throughput data processing. Maren Buck was my first post-doctoral mentor when I joined the lab, and without realizing it, she single-handedly defined the entire course of my Ph. D. by one day suggesting that I try labeling one of her proteins with fluorescein and photobleaching it. 5 plus years and 500 plus FRAP traces later, I remain grateful.

Each of my committee members has also played a central role in my scientific formation. Zhen-Gang Wang gave me a deep love for thermodynamics and polymer physics (maybe even statistical mechanics?), and has been a generous contributor both in terms of time and insight. Sarkis Mazmanian got me hooked on mucosal immunology, an addiction that I still have not yet managed to kick. I am thankful for the risk he took with me several years ago, allowing me to join his lab and collaborate so closely. None of our exciting and challenging work together has been reported here, but I am hopeful that some of it will be reported soon. Mark Davis has given valuable advice at many times, and his encouragement to explore the temperature dependence of the chain diffusivity led to the serendipitous discovery of the phase behavior described in Chapter 3.

So much more could said, but the key point is that one is born hungry for knowledge and is fed by others. Moreover, good men carry success well, for the most fruitful branches bow the lowest. Why then, I wonder, are we so seldom prostrate?

# ABSTRACT

Artificial proteins may be programmed to reversibly self-assemble into water-soluble networks, or “hydrogels”, by encoding them with terminal coiled-coil forming domains. Such networks are model viscoelastic materials. The well-defined molecular structures adopted by proteins, combined with their facile preparation by recombinant synthesis, invite a careful exploration of the relationship between protein sequence and the resulting network properties.

This work explores the relationship between network reorganization and diffusion from the perspective of single chains, using artificial elastin-like proteins as a model system. We make use of fluorescence recovery after photobleaching (FRAP), a classic biophysical technique, to measure chain mobilities as a function of network structure and probe architecture. Reversible network association is demonstrated to control the effective diffusivity of network-bound chains, and a novel mechanism of chain transport is proposed: the chains naturally partition into various bound states, and move by “hopping” from site to site in between binding events.

A careful analysis of the equilibrium constants that control this partioning leads to the conclusion that the sequential binding of identical chain ends to the network is inherently asymmetric: the first association is always stronger than the second. This binding asymmetry is shown to arise from a strong entropic penalty for chain entry into the fully bound state due to local network structure. We derive a simple equation predicting the degree of binding asymmetry as a function of network geometry from equilibrium

statistical mechanics. A large set of self-diffusivity measurements on a series of model telechelic proteins finds good agreement with this new theory. Generalized binding asymmetry for chains with many associative domains also holds.

Finally, the inherent viscoelasticity of the elastin-like network is found to couple with an entropically driven phase separation above a critical temperature set point. Relaxation of the viscoelastic stress throughout the process of phase domain segregation is found to induce highly dynamic phase patterns. The time evolution of these patterns illustrates that a delicate balance of surface tension and viscoelastic stress controls pattern formation in viscoelastic materials.

# PUBLISHED CONTENT AND CONTRIBUTIONS

CHAPTER 1 is published as an article in the Journal of the American Chemical Society, and may be cited as follows:

Peter B. Rapp, Ahmad K. Omar, Jeff J. Shen, Maren E. Buck, Zhen-Gang Wang, and David A. Tirrell. "Analysis and Control of Chain Mobility in Protein Hydrogels." *Journal of the American Chemical Society* **2017** 139 (10), 3796-3804.

DOI: 10.1021/jacs.6b13146

*Author contributions: P.B.R. and D.A.T. designed the experiments and wrote the chapter. P.B.R. performed the experiments and analyzed the data. A.K.O. and Z.G.W. designed and implemented the simulations. J.J.S. performed amino acid synthesis. M.E.B. cloned the proteins.*

CHAPTER 2 was written in close collaboration with Ahmad K. Omar, who developed the statistical-mechanical framework for interpreting the experimental results. Bradley K. Silverman provided critical support in obtaining and analyzing the large data sets.

CHAPTER 3 describes the discovery of unusual phase behavior in a protein polymer originally designed by Maren E. Buck. Quantitative analysis of the phase patterns was performed by Bradley K. Silverman.

# TABLE OF CONTENTS

# LIST OF FIGURES

# LIST OF TABLES

*Chapter 1*

# ANALYSIS AND CONTROL OF CHAIN MOBILITY IN PROTEIN HYDROGELS

## 1.1 Abstract

Coiled-coil domains can direct the assembly of protein block copolymers into physically crosslinked, viscoelastic hydrogels. Here we describe the use of fluorescence recovery after photobleaching (FRAP) to probe chain mobility in reversible hydrogels assembled from engineered proteins bearing terminal coiled-coil domains. We show that chain mobility can be related to the underlying dynamics of the coiled-coil domains by application of a 3-state "hopping" model of chain migration. We further show that genetic programming allows the effective mobility of network chains to be varied 500-fold through modest changes in protein sequence. Destabilization of the coiled-coil domains by site-directed mutagenesis increases the effective diffusivity of probe chains. Conversely, probe mobility is reduced by expanding the hydrophobic surface area of the coiled-coil domains through introduction of the bulky leucine surrogate homoisoleucine. Predictions from the 3-state model imply asymmetric sequential binding of the terminal domains. Brownian Dynamics simulations suggest that binding asymmetry is a general feature of reversible gels, arising from a loss in entropy as chains transition to a conformationally restricted bridged state.

## 1.2 Introduction

Protein engineering enables the design and synthesis of monodisperse polymers with functional domains drawn from nature or created de novo (*1*). Because protein polymers are

made by expression of artificial genes, they can be modified easily and systematically by editing of their DNA coding sequences. In this manner, proteins have been engineered with binding domains that drive them to self-assemble into physically crosslinked networks (*2*). The non-covalent nature of domain association in these networks permits the constituent proteins to exchange binding partners. Such processes are common in polymeric systems; for example, block copolymer micelles in solution exchange chains at rates that are highly dependent on the architectures of the individual blocks (*3*, *4*), and telechelic polymers with hydrophobic endgroups form micellar networks that relax via chain disengagement from interconnected micelles (*5*). Exchange of polymeric strands also plays essential roles in biological processes, including repair of double-stranded DNA breaks by homologous recombination (*6*, *7*).

Strand exchange dynamics are particularly important in governing the viscoelastic properties of hydrogels assembled from proteins that carry amphipathic α-helical domains (*2*, *8*, *9*). Amphipathic helices are ubiquitous in nature, and often function by driving protein aggregation through the formation of coiled-coil bundles (*10-12*). Hydrogels assembled from coiled-coil proteins are reversible: they can disassemble and reassemble rapidly in response to external stimuli such as temperature changes or mechanical shear (*2*). These hydrogels are also shear thinning, injectable and potentially useful for delivery of cellular or molecular therapeutics (*13*). Because strand exchange underlies the physical behavior of the network, tuning the strand exchange rate is essential for optimizing hydrogel performance.

Characterization of strand exchange in coiled-coil systems has largely been limited to

chromatographic analyses of equilibrium solutions (*10*, *14*, *15*), stopped-flow spectroscopy (*16*), and fluorescence dequenching experiments (*9*, *17*). These techniques are most useful for analysis of dilute solutions, and cannot be applied directly to hydrogels. In contrast, fluorescence recovery after photobleaching (FRAP) is routinely used to assess macromolecular diffusion and binding in crowded environments such as the cellular milieu (*18*). For example, FRAP has been used to measure rates of binding of leucine-zipper transcription factors to chromatin in live cells (*19*). The method requires only minor perturbation of the system of interest through sparse labeling with fluorescent dyes, and is amenable to analysis by models that permit simultaneous determination of diffusion coefficients and binding constants (*18*, *20*). Although FRAP has been used to probe chain mobility in polymer networks, strand exchange has either not been important in these systems (e.g. in covalently crosslinked networks) (*21*, *22*), or has not been quantified (*23*-*26*). The technique is commonly used only to estimate effective chain diffusivity, and when interchain binding is present, it is typically assessed qualitatively.

This chapter describes the use of FRAP to characterize the interplay between strand exchange and chain mobility in associative protein hydrogels. The gels were formed from an engineered triblock protein (designated "PEP") composed of two identical coiled-coil domains ("P") at the N- and C-termini, flanking a water-soluble midblock ("E") consisting of elastin-like polypeptide repeats (**Supplementary Table 1.1**). The P domain is derived from the N-terminal fragment of rat cartilage oligomeric matrix protein (COMP), and has been reported to form homopentameric coiled-coil bundles (*8*, *27*). Association of the P domains drives the reversible assembly of PEP into optically transparent, physically

crosslinked networks. The viscoelastic behavior of PEP networks is analogous to that of other networks assembled by association of coiled-coil domains (*13*).

Here we use FRAP to determine diffusion coefficients and equilibrium binding constants of fluorescently labeled PEP chains in PEP hydrogels. We find that the mobility of PEP chains is significantly reduced by reversible network association. To gain insight into the mechanism of chain mobility, we elaborate a previously developed 2-state reaction-diffusion model for FRAP into a 3-state "hopping" model of chain migration (*18*, *20*). We find experimentally and in coarse-grained Brownian Dynamics simulations of gel-forming telechelic polymers that binding of one of the P domains in PEP reduces binding of the second. Finally, we show that tracer chain mobility is highly sensitive to structural changes in the coiled-coil endblocks. Taken together, our results furnish a new framework for understanding and controlling chain mobility in reversible polymer networks.

## 1.3 Experimental

### 1.3.1 Hydrogel Preparation

All protein concentrations are reported in % (*w*/*v*). To prepare a 10% (*w*/*v*) gel, 100 $\mu$L of phosphate buffer (100 mM, pH 7.2 – 7.4) was added directly to 10 mg of lyophilized PEP and the suspension was placed on ice to promote gelation. After 2 – 4 h on ice, hydration was usually complete as evidenced by the formation of an optically clear gel. In order to ensure network homogeneity, gels were typically heated above the gel-sol transition temperature (~75 °C for a 10% gel) by submerging them in boiling water for 30 – 60 s. Upon heating, even concentrated solutions of PEP (up to 30%) became viscous liquids. After heating,

samples were immediately placed back on ice to allow gels to reform. Alternatively, samples could be left on ice for 24 – 48 h without heating in order to obtain completely homogenous gels. Fluorescent hydrogels were prepared by adding low concentrations (typically mass ratios of 1:50 or 1:100 were used) of fluorescein-labeled probe chains to PEP networks.

### 1.3.2 Fluorescence Recovery after Photobleaching

Fluorescent hydrogels were placed between two glass slides separated by 120 $\mu$m spacers (Secure-Seal spacer, 9 mm × 0.12 mm, Life Technologies). Photobleaching experiments were performed on a Zeiss LSM 5 Exciter inverted confocal microscope equipped with the following laser lines: 458, 488, 514, 543 and 633 nm. All lasers were typically applied during the bleaching period. Cylindrical bleach volumes of defined radius were created using the bleach applet in the Zen 2009 confocal microscopy software suite (Zeiss). A 20X objective was used for the large spot size experiments ($a$ = 12.5 – 25 μm). 2000 iterations at a scan rate of 1.61 $\mu$s per pixel resulted in a well-resolved cylindrical bleach volume that penetrated the entire gel. Fluorescence recovery in the photobleached spot was monitored between 500 and 530 nm with a wide pinhole on a single z-slice in the center of the hydrogel. Images were typically collected at a rate of 1 $s^{-1}$ and at a resolution of 256 × 256 pixels. Fluorescence intensities within the photobleached spot were quantified using the Zen region-of-interest "mean ROI" applet. To account for non-specific photobleaching caused by image acquisition during spot recovery, all curves were normalized to the fluorescence intensity of a region far from the photobleached spot. Quantitative analysis of the fluorescence recovery curves was performed in MATLAB.

## 1.4 Results and Discussion

### 1.4.1 Reversible PEP hydrogels show fluorescence recovery after photobleaching

To probe chain mobility in PEP hydrogels, we generated a series of fluorophore-labeled probes that would associate with network junctions in a defined manner, without affecting the rheological behavior of the network. We first performed site-directed mutagenesis on PEP to introduce a single cysteine residue into the elastin-like midblock, resulting in $PE_CP$ (**Supplementary Table 1.1**). The absence of other cysteines in the protein enabled site-specific conjugation of fluorescein-5-maleimide (*f5m*) to the central thiol via Michael-type addition (**Figure 1.1A** and **Supplementary Figure 1.1**). The $PE_CP$-*f5m* conjugate yielded homogeneous, fluorescent gels when added at low concentrations into PEP networks (typically $PE_CP$ to PEP ratios of 1:50-100 were used). Using oscillatory shear rheometry, we verified that the rheological behavior of PEP gels was minimally perturbed by this labeling strategy (**Supplementary Figure 1.2**).

Next we prepared fluorescent PEP hydrogels of defined thickness (~120 μm), and photobleached cylindrical volumes in each gel using a standard confocal microscope. In 10% weight-to-volume (*w*/*v*) gels, we observed steady recovery of fluorescence intensity within the photobleached spot (**Figure 1.1B**). Fluorescence recovery results from diffusion of unbleached fluorophore into the photobleached region, and confirms that $PE_CP$ chains are mobile within PEP networks. Consistent with our hypothesis that $PE_CP$ is associated with the network, we observed accelerated rates of fluorescence recovery in networks solubilized with 8 M urea, a common protein denaturant.

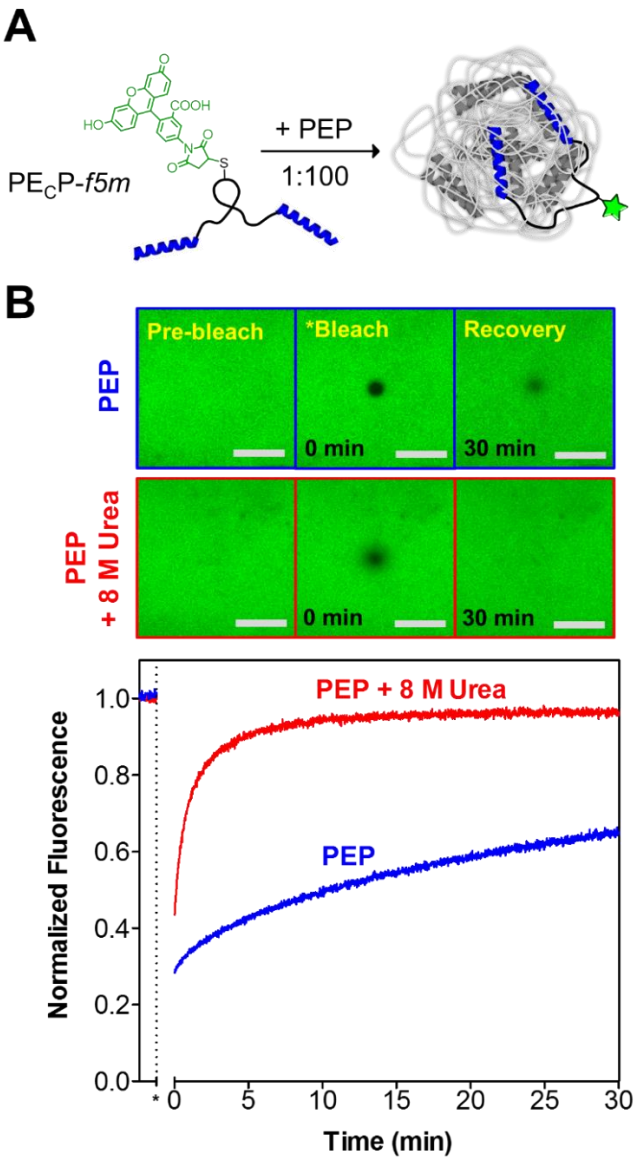


**Figure 1.1. Fluorescence recovery after photobleaching in labeled PEP hydrogels.** (**A**) Labeling of PEP hydrogels was achieved by addition of a fluorescent PEP analogue (PE$_C$P-*f5m*) at low concentrations. (**B**) FRAP in 10% *w/v* PEP hydrogels as monitored by confocal microscopy. A circular bleach spot with a radius of 12.5 μm recovers slowly over a period of 30 min (blue curve). The same network solubilized in 8 M urea shows accelerated fluorescence recovery (red curve). Scale bar 100 μm.

### 1.4.2 Quantitative analysis of chain mobility.

Gels were prepared at protein concentrations ranging from 2% to 10% *w*/*v* (gelation in PEP solutions occurs near 3%). As expected, the rate of fluorescence recovery after photobleaching decreased with increasing protein concentration (**Figure 1.2A**). To quantify chain mobility, we fit the experimental FRAP curves to a model that attributes fluorescence recovery to diffusion only (see **Supplementary Equations 23**, **25** and **30**). Such an analysis is similar to standard FRAP analyses of diffusion in polymer networks (*22*, *23*, *25*, *26*, *28*), and results in a single parameter termed $D_{eff}$, the effective diffusion coefficient (*18*). In the case of PEP networks, fluorescence recovery represents diffusion slowed by binding; $D_{eff}$ provides a measure of the mobility of polymer chains for which Brownian motion is constrained by reversible network association. The effective diffusion model yielded good fits to the fluorescence recovery curves (**Figure 1.2**), enabling us to estimate $D_{eff}$ for each gel. $D_{eff}$ decreases steeply with increasing protein concentration, dropping from $1.3 \times 10^{-8}$ $cm^2\ s^{-1}$ in viscous 2% solutions to $2.3 \times 10^{-10}$ $cm^2\ s^{-1}$ in 10% gels (**Figure 1.2B**).

We attribute the slower recovery at higher protein concentrations primarily to the increased concentration of binding sites, although changes in network topology such as loop suppression and chain entanglement may also suppress chain release from junctions (*5*, *8*, *29*). To explore whether the effective diffusivity is controlled by reversible endblock binding, we measured chain mobility as a function of the concentration of the protein denaturant urea. At a fixed protein concentration of 10%, the rate of fluorescence recovery increased abruptly with increasing concentration of urea (**Figure 1.2C**); addition of 2 M urea increases $D_{eff}$ by 9-fold (**Figure 1.2D**). The abruptness of the change suggests that modest concentrations of

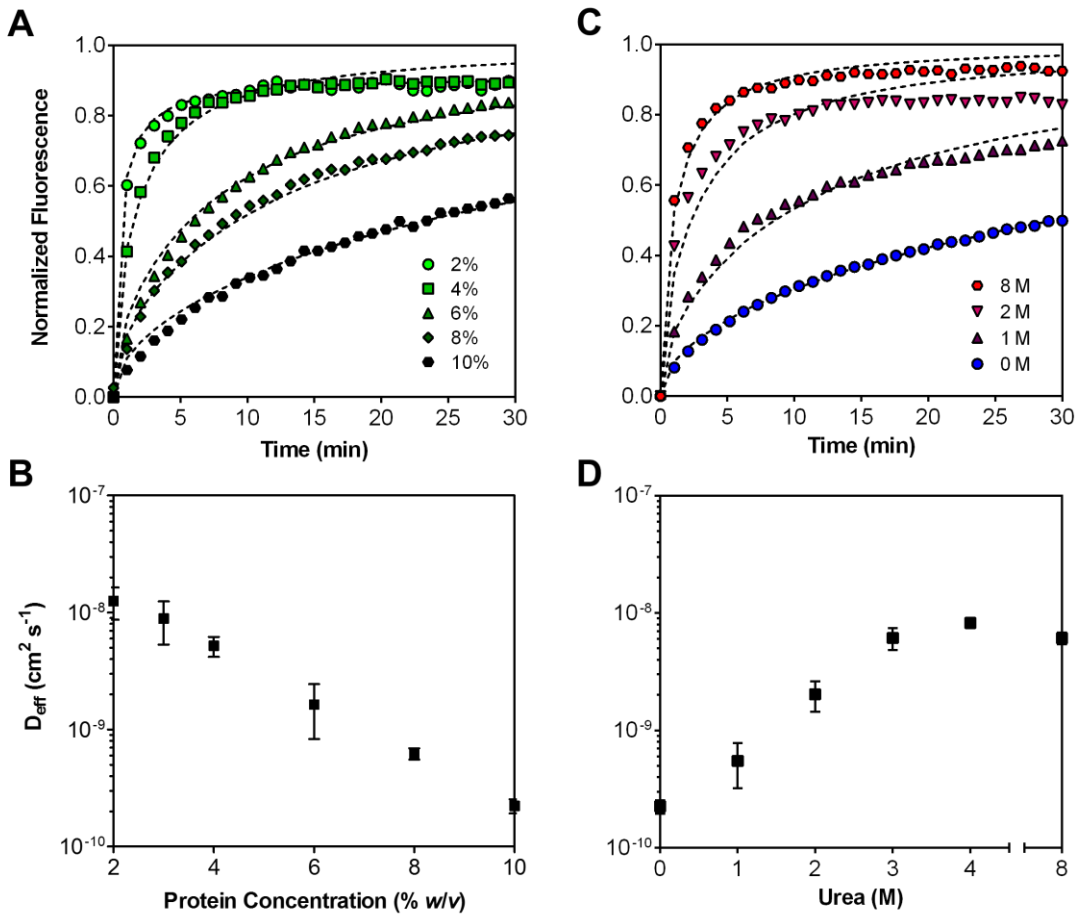


**Figure 1.2. Quantitative analysis of chain mobility.** The rate of fluorescence recovery after photobleaching in PEP hydrogels depends on gel density and concentration of denaturant. (**A**) FRAP curves generated from gels prepared at protein concentrations ranging from 2% to 10%, showing that the recovery rate decreases with increasing gel density. (**B**) Quantification of effective chain mobility as a function of gel density. $D_{eff}$ varies inversely with gel density. (**C**) FRAP curves generated from 10% protein solutions prepared in increasing concentrations of urea. Fluorescence recovery rates increase with increasing amounts of urea, indicating disruption of interchain binding. (**D**) Quantification of the urea recovery curves. $D_{eff}$ rises with increasing concentrations of urea, eventually reaching a plateau above 3 M. Error bars represent mean ± standard deviation ($n \geq 3$ recovery curves from at least two gels). Dashed curves in A and B represent fits generated from the effective diffusion model.

urea are sufficient to inhibit association of the N- and C-terminal domains of PEP. Disruption of interchain binding destroys network integrity; samples prepared in high concentrations of urea (greater than 2 M) were viscous liquids.

### 1.4.3 3-state "hopping" model of chain migration in reversible hydrogels

Although the preceding analysis provides a useful description of chain mobility in PEP networks, it does not separate the effects of diffusion and interchain association. We sought to distinguish the roles of diffusion and binding in PEP networks. To this end, we formulated a model that captures both the diffusive and reactive elements of strand exchange in a physical molecular network. Our model is an extension of a 2-state reaction-diffusion model originally developed by Sprague et al., which relates the rate of fluorescence recovery to an equilibrium between two states: one free and one bound (*18*). Because each PEP chain has two terminal P domains, we chose to model network association as an equilibrium involving three sequential states (represented schematically in **Figure 1.3A**):

$$f \underset{}{\overset{K_1}{\rightleftharpoons}} d \underset{}{\overset{K_2}{\rightleftharpoons}} b \qquad \textbf{(Eq. 1)}$$

In the free state (*f*) neither P domain is bound to another and the chain can diffuse throughout the network with a self-diffusivity $D_f$. If both P domains on the chain join coiled-coil bundles, the chain enters the bound state (*b*) and becomes fully network-associated. We also consider an intermediate dangle state (*d*) in which only one of the P domains is tethered to the network. We distinguish the diffusion coefficient of free chains $D_f$ from the effective diffusion coefficient $D_{eff}$, which represents diffusion slowed by binding. Because $D_f$ represents free diffusion in the absence of binding, $D_{eff}$ will be smaller than $D_f$ whenever binding interactions

are significant. We now make several simplifying assumptions. First, we assume that both binding processes ( $f \rightleftharpoons d$ and $d \rightleftharpoons b$ ) achieve equilibrium, and that both are governed by the same equilibrium constant ($K_1 \approx K_2 = k_{on}^*/k_{off}$). Note that $k_{on}^* = k_{on}S_{eq}$ is a pseudo-first-order rate constant calculated from the true association rate constant $k_{on}$ (a second-order rate constant) by assuming a constant concentration of binding sites $S_{eq}$ (*18*). We also assume that each P domain has a single binding mode, and that chain mobility in either of the two associated states (*d* or *b*) is negligible ($D_d = D_b \approx 0$). The physical picture is therefore one in which chains are constrained to migrate by "hopping" from site to site, but are otherwise fixed in space (**Figure 1.3B**). The distance a chain travels during such a transition (the "hopping radius") is:

$$R^* = \sqrt{\frac{6D_f}{k_{on}^*}} \qquad \textbf{(Eq. 2)}$$

A material balance on **Eq. 1** results in a system of three coupled reaction-diffusion equations that can be used to model experimental FRAP curves and to estimate the three parameters in the model ($k_{on}^*$, $k_{off}$ and $D_f$). We sought an analytical solution to the 3-state reaction-diffusion model. Following Sprague et al. for the 2-state model (*18*), Laplace transformation of **Eq. 1** yielded an analytical solution involving modified Bessel functions in Laplace space (see **Supporting Information** for details). When binding is neglected ($k_{on}^* \rightarrow 0$ and $k_{off} \rightarrow \infty$), the new solution reduces to the previously reported closed-form solution for free diffusion in a circular bleach spot (*18*, *30*). Numerical inversion of the Laplace-domain solution using the MATLAB routine *invlap.m* produces the time-domain response (*31*), providing estimates

of model parameters by comparison with experimental curves. FRAP curves simulated using the 3-state model were fit to experimental curves using the MATLAB routine *nlinfit.m*, as well as a custom curve-fitting algorithm that gave comparable results (**Supplementary Figure 1.5**). With this approach, we found it difficult to obtain reliable estimates of all three model parameters from a single curve. Therefore, we simplified our curve-fitting procedure by first estimating $D_f$ in a separate FRAP experiment using a non-binding elastin-like probe where the P domain endblocks were replaced by an irrelevant "A" peptide that does not form coiled-coils (see **Supplementary Table 1.1** for sequence) (*32*, *33*).

Recovery rates observed with the non-binding "$AE_CA$" probe were 20- to 50-fold faster than those observed with the $PE_CP$ probe (**Figure 1.3C** and **Supplementary Figure 1.6**). This provides further evidence that chain mobility is substantially reduced by reversible association of the coiled-coil domains. By attributing the recovery of $AE_CA$ to diffusion alone, we estimated that $D_f$ for an unbound PEP chain is approximately $1.59 \times 10^{-8}$ $cm^2$ $s^{-1}$ in a 10% gel (assuming $D_f \sim M^{-3/5}$ for a polymer chain in good solvent) (*28*). This value is similar to $D_{eff}$ in dilute solutions of PEP (**Figure 1.2C**), and is within range of the diffusivities reported for macromolecules in other hydrogels. For example, dextran probes of similar molecular weight diffuse through dextran solutions and gels at approximately $10^{-7}$ $cm^2$ $s^{-1}$, and unbound globular proteins diffuse through poly(ethylene glycol) gels at rates of $10^{-7}$ – $10^{-9}$ $cm^2$ $s^{-1}$, depending on the hydrodynamic radius of the protein and the mesh size of the network (*22*, *28*, *34 – 36*).

Next we sought to estimate $k_{on}^*$ and $k_{off}$ for $PE_CP$. A grid of all possible ($k_{on}^*$, $k_{off}$) values was

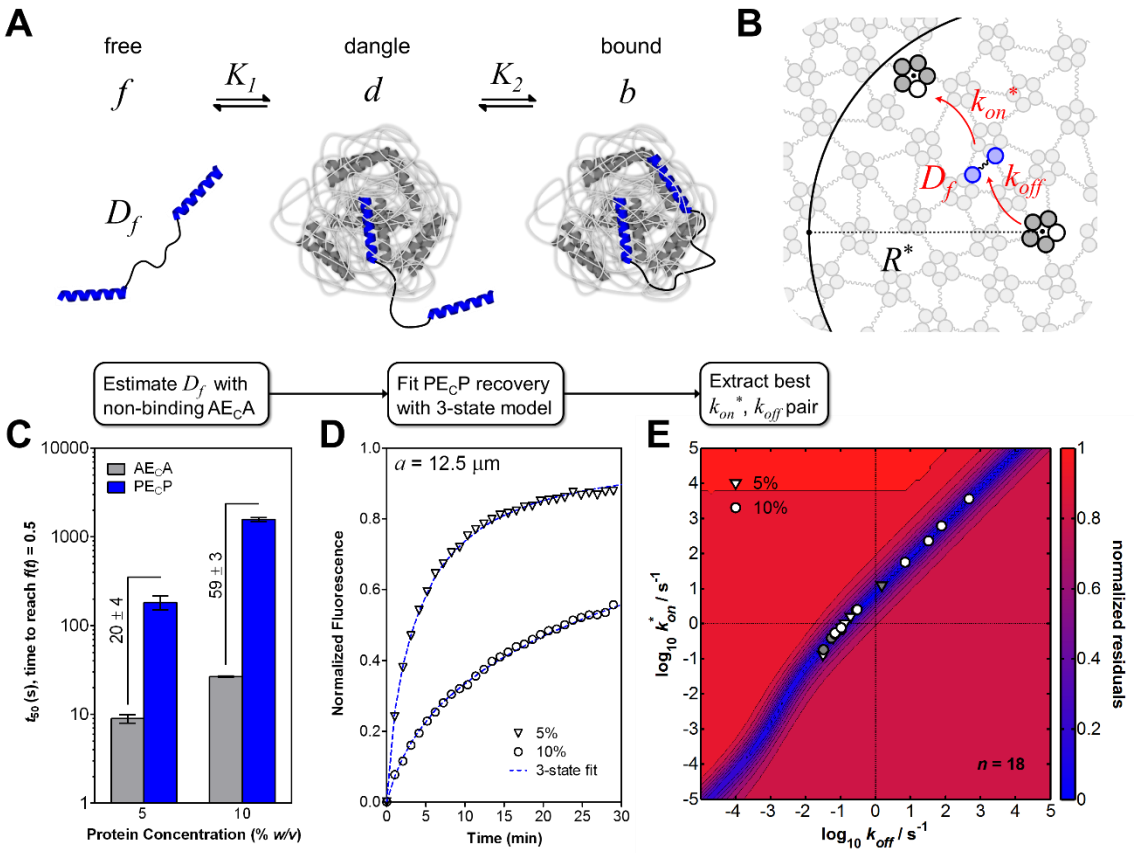


**Figure 1.3. A 3-state reaction-diffusion analysis of chain migration in reversible hydrogels.** (**A**) Illustration of the 3-state "hopping" model. (**B**) After a chain dissociates from an initial binding site (at a rate determined by $k_{off}$), it reassociates with a new junction at a rate determined by $k_{on}^*$. The average distance a free chain diffuses ("hops") before rebinding is $R^*$. (**C**) $AE_CA$, a non-binding probe without terminal coiled-coils shows rapid fluorescence recovery compared to the associative probe $PE_CP$ (vertical text shows fold-change ± standard deviation, $n$ = 3 recovery curves measured in one gel preparation for each probe). (**D**) The 3-state model yields excellent fits to the normalized recovery curves for a bleach spot radius ($a$) of 12.5 μm. (**E**) Contour map showing normalized residuals of a representative 3-state model fit to a recovery curve from a 10% gel ($a$ = 12.5 μm) for a wide range of $k_{on}^*$ and $k_{off}$ values. Points on the map represent ($k_{on}^*$, $k_{off}$) pairs obtained from independent photobleaching experiments performed in multiple gels ($a$ = 12.5 μm, $n$ = 12). Shaded symbols are experiments performed with a larger spot size ($a$ = 25 μm, $n$ = 6). The values of $k_{on}^*$ obtained from 5% gels were multiplied by 2 in order to compare them with values from 10% gels on the same map.

sampled in log space (typically in increments of $10^{0.1}$ between $10^{-5}$ and $10^{5}$ s) in order to find the pair that minimized the residuals between the simulated and experimental curves. This pair was then supplied as the initial guess in the MATLAB algorithm *nlinfit.m*, which finally produced a unique ($k_{on}^{*}$, $k_{off}$) pair corresponding to the best fit (*18*). Excellent fits to experimental FRAP curves were obtained with this procedure (**Figure 1.3D**). Within the range of bleach spot radii that we explored ($a$ = 1 – 25 μm), the quality of the fit was relatively insensitive to the individual values of the rate constants, but strongly dependent on their ratio (**Figure 1.3E**). For a 10% gel and spot radius of 12.5 μm, the data lie along a line with slope $k_{on}^{*}/k_{off}$ = 7.4 ± 0.9, whereas $k_{on}^{*}$ itself ranges from 0.2 $s^{-1}$ to 3.6 × $10^{3}$ $s^{-1}$.

To obtain estimates of the individual values of the rate constants, we made the assumption that $k_{off}$ corresponds to the network relaxation rate measured by oscillatory shear rheometry (**Supplementary Figure 1.2**, $k_{off} \approx \omega_c$), and used the ratio of $k_{on}^{*}$ to $k_{off}$ to obtain $k_{on}^{*}$. This provides $k_{off}$ = 0.51 ± 0.02 $s^{-1}$ and $k_{on}^{*}$ = 3.8 ± 0.5 $s^{-1}$, suggesting a relatively weak binding equilibrium for the P domain. Strand exchange rates ($k_{off}$) reported for coiled-coils vary widely, e.g., 3 × $10^{-3}$ $s^{-1}$ (GCN4) (*37*), 3 × $10^{-4}$ $s^{-1}$ – 0.7 $s^{-1}$ (model leucine zippers) (*16*), 0.2 $s^{-1}$ (Fos/Jun) (*38*), 1 × $10^{-4}$ $s^{-1}$ (α-tropomyosin) (*39*), 6 × $10^{-7}$ $s^{-1}$ – 5 × $10^{-3}$ $s^{-1}$ (4-helix bundle proteins) (*9*, *40*, *41*). Refolding and association rates ($k_{on}^{*}$) are typically much faster (e.g., for Fos/Jun and GCN4, roughly 1 $s^{-1}$ even at low μM concentrations, resulting in dissociation-limited exchange kinetics with $K_d$ on the order of 0.01 – 1 μM for these zippers) (*16*, *38*, *42*). By comparison, all fits in **Figure 1.3E** give an average dissociation constant of $K_d$ = 173 ± 29 μM. This leads to a free energy of network association $\Delta G_a$ = -5.1 ± 0.1 kcal $mol^{-1}$. This number is within range of the Gibbs free energy of pentamer formation for native P ($\Delta G°$ =

-4.3 kcal $mol^{-1}$) estimated from thermal denaturation curves using circular dichroism spectroscopy, and is similar in magnitude to folding energies for other weakly associating coiled-coil structures (*43*, *44*).

Sprague et al. showed that, for the 2-state reaction-diffusion model, the full model may be simplified to the single-parameter effective diffusion model (*i.e.*, $D_{eff}$ alone gives good fits) whenever the dimensionless constant $k_{on}^{*}a^2/D_f$ is significantly greater than unity (*18*). This constraint ensures that binding is rapid relative to the characteristic diffusion time of the experiment. An important characteristic of this regime is that the rate of fluorescence recovery is insensitive to the individual values of $k_{on}^{*}$ and $k_{off}$, and depends only on their ratio. Using the above estimates for $k_{on}^{*}$ and $D_f$, we find that $k_{on}^{*}a^2/D_f \sim 10^2$ when $a$ = 12.5 $\mu$m. This suggests that all of the FRAP experiments reported here lie in the effective diffusion regime. This explains the imprecision in the estimates of $k_{on}^{*}$ and $k_{off}$ derived from our FRAP experiments (**Figure 1.3E**), and our ability to generate good fits of our FRAP curves using $D_{eff}$ alone (**Figure 1.2A**).

### 1.4.4 Predicting the hopping mobility with the 3-state model

Given that $k_{on}^{*}a^2/D_f >> 1$ (see the above discussion), we can assume local equilibrium during the fluorescence recovery process. Under this assumption, it can be shown that for a chain with $N$ associative domains (i.e., for an "$N$+1"-state hopping model, see **Supporting Information**), the ratio $D_f/D_{eff}$ is given by

$$\frac{D_f}{D_{eff}} = 1 + K_1 + K_1K_2 + \cdots + \prod_{i=1}^{N} K_i \qquad \textbf{(Eq. 3)}$$

This allows us to predict the hopping mobility $D_{eff}$ for a chain with any number of associative domains, provided $D_f$ and the equilibrium constants are known. In the case of the 3-state model (**Eq. 3**, $N = 2$) if only one of the equilibrium constants is known, it is possible to make inferences about the relative magnitudes of $K_1$ and $K_2$ by comparing predictions from **Eq. 3** to experimental mobilities. We therefore designed a "$PE_C$" probe that could associate with the network only once. The recovery curve of $PE_C$ should reflect the equilibrium between free and dangling chains, thus providing an independent measurement of $K_1$. We also refined our estimates of $D_f$ by measuring the recovery rate of a non-binding "$E_C$" probe comprising only the elastin-like midblock. As before, we assume $D_f \sim M^{-3/5}$ in order to estimate $D_f$ for the larger, associative probes.

The fluorescence recovery curves for these probes are shown in **Figure 1.4A**. From the $E_C$ probe we estimated $D_f$ for $PE_CP$ as $2.94 \pm 0.35 \times 10^{-8}$ cm$^2$ s$^{-1}$. This is roughly 2-fold larger than the value estimated from the recovery rate of $AE_CA$, and suggests a slight tendency for the A domain to self-associate. Fitting the $PE_C$ recovery with a 2-state model (**Eq. 3**, $N = 1$) provides $K_1 = 26.5 \pm 4.5$. Under the assumption that $K_1 = K_2$, this estimate can be applied directly to the 3-state model (**Eq. 3**, $N = 2$) in order to predict $D_{eff}$ for $PE_CP$. This approach substantially under-predicts the observed mobility (**Figure 1.4B**, $D_{obs} = 5.1 \times D_{pred}$). Moreover, fitting the $PE_CP$ recovery with a 3-state model without prior knowledge of $K_1$ (again assuming equivalence of $K_1$ and $K_2$) provides $K_1 = K_2 = 11.7 \pm 1.8$. These data are summarized in **Table 1.1**.

We hypothesized that the disparity in the values of $K_1$ obtained from the $PE_C$ and $PE_CP$

probes might reflect a difference in the values of the equilibrium constants for sequential binding of the two P domains of $PE_CP$ (**Figure 1.3A**), with $K_1$ greater than $K_2$. To test this hypothesis, we performed coarse-grained Brownian Dynamics simulations of gel-forming telechelic polymers (see **Supporting Information** for details). We used a Kremer-Grest bead-spring model with "sticky" beads at the chain ends interacting through an attractive Lennard-Jones potential (*45*). **Figure 1.4C** shows a representation of a gel comprised of chains with a length of 100 beads. The stickers cluster to form distinct network junctions, which we define as groups of neighboring stickers. By analogy to the 3-state model, we define the state of a simulated chain by specifying whether its stickers are both free from junctions (*f*) or both attached to junctions (*b*), or if only one sticker is bound (*d*). $K_1$ and $K_2$ are then obtained by computing the fraction of chains in each state.

We find that a majority of the chains in our simulation are fully bound ($[b]_{eq}$ = 0.86, see also **Supplementary Figure 1.7**), in good agreement with the fraction of bound PEP chains estimated by FRAP (**Table 1.1**, $[b]_{eq}$ = 0.91). Importantly, asymmetry in the two binding constants is apparent in the simulation, with $K_1$ = 21.2, $K_2$ = 6.3, and $K_1/K_2$ = 3.4. We can also isolate $K_1$ and $K_2$ from our FRAP data by assigning the $k_{on}^*/k_{off}$ ratio obtained from $PE_C$ to $K_1$, and then resolving the discrepancy between $D_{pred}$ and $D_{obs}$ for $PE_CP$ by treating $K_2$ as an adjustable parameter (**Eq. 3**). Interpreting the FRAP data in this way provides $K_1$ = 26.5 ± 4.5, $K_2$ = 6.0 ± 2.1, and $K_1/K_2$ = 4.4 ± 1.7, in good agreement with the simulation. These observations are consistent with the hypothesis that reversible binding of a telechelic polymer to a macromolecular network is inherently asymmetric: the second binding event is disfavored relative to the first.

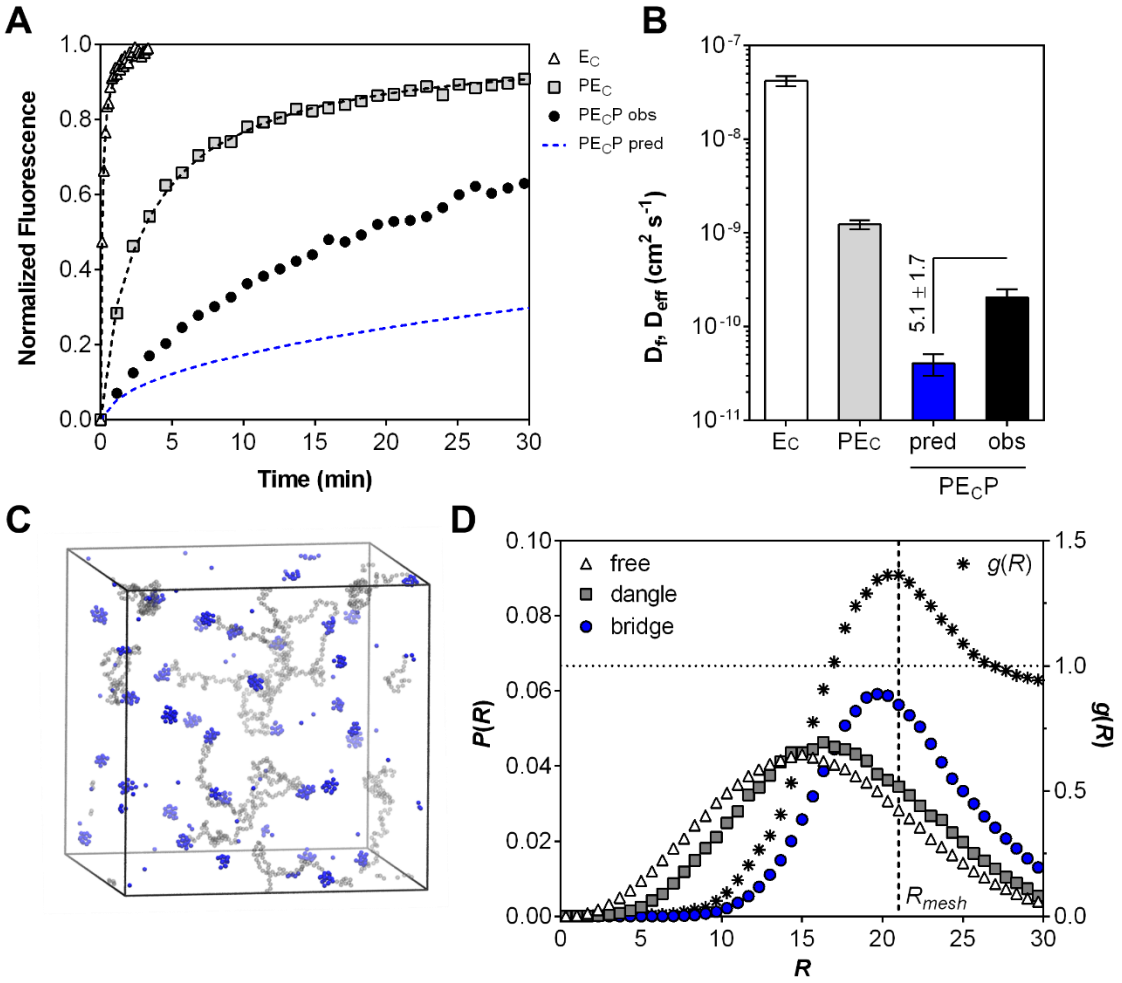


**Figure 1.4. Predictions from the 3-state model imply binding asymmetry in PEP hydrogels.** (**A**) FRAP experiments on $E_C$ and $PE_C$ probes provide independent estimates of $D_f$ and $K_1$ that, together with **Eq.** (**3**), predict $D_{eff}$ and the recovery rate of $PE_CP$ (blue dashed line). The experimentally observed recovery rate is higher than predicted, suggesting asymmetric sequential binding where $K_1 > K_2$. Fits to the $E_C$ and $PE_C$ curves were generated with 1-state (**Eq. 3**, $N = 0$) and 2-state (**Eq. 3**, $N = 1$) effective diffusion models, respectively (black dashed lines). (**B**) Assuming $K_1 = K_2$ under-predicts the observed $D_{eff}$ for $PE_CP$ by roughly 5-fold (mean ± SD, $n \geq 2$ gel preparations per probe). (**C**) Snapshot of a simulated gel with stickers (blue) connected by non-sticker beads (grey). The non-sticker beads of only 10 chains are shown for clarity. (**D**) Origin of the binding asymmetry. The radial distribution function of network junctions $g(R)$ is shown together with the chain end-to-end distributions $P(R)$ for the three states (bins of $\Delta R = 0.67$ were used in computing the distributions).

Free and dangling chains can adopt a substantial set of conformations at distances $R < R_{mesh}$, the location of maximum junction density. These conformations are lost upon entry into the bridge state.

---

We propose that the inequality of $K_1$ and $K_2$ arises from a difference in the entropic penalties associated with successive binding events. In transitioning from the free to the dangle state, a chain becomes restricted to a fraction of the system volume, and loses entropy in proportion to the change in accessible volume. The subsequent transition from dangle to bridge causes a similar entropic loss, but with the additional constraint that the volume accessible to the remaining chain end also depends on the junction spacing. Gelation promotes a depletion of neighboring junctions below the characteristic mesh size of the gel. Dangling chains must discard the rich set of conformations accessible below this length scale when they bridge neighboring junctions.

The effects of network structure on chain conformation are apparent in our simulation. **Figure 1.4D** compares the distributions of chain end-to-end distances $P(R)$ for the three major states to $g(R)$, the junction radial distribution function. Free and dangling chains can access a substantial set of conformations at distances $R < R_{mesh}$, the location of maximum junction density. In contrast, bridged chains are restricted to a narrower set of end-to-end distances that correspond closely to $R_{mesh}$. Mild chain stretching in the bridged state is also apparent, which may enhance the degree of binding asymmetry we observe (the average end-to-end distance of bridged chains $R_b$ exceeds that of dangling chains $R_d$ by a factor of 1.2). However, substantial conformational freedom may still be lost in transition from dangle to bridge, even in the absence of chain stretching.

An intriguing possibility is that, in addition to hopping, the diffusivity of a $PE_CP$ probe may be enhanced by "walking"; *i.e.*, by cycling between the dangle and bound states *d* and *b*. In this process, the chain migrates through the network in discrete steps that correspond to the average distance between binding sites. A simple scaling analysis argues that this diffusive mode is not significant in PEP gels. Consider a chain with both ends bound to the network. The characteristic diffusivity of this chain can be estimated as $D_b \sim R_b^2/\tau_b$, where $\tau_b \approx k_{off}^{-1}$ is the average lifetime of the bound state. The expected contribution of this state to $D_{eff}$ is $[b]_{eq}D_b$. As before, we obtain $k_{on}^*$ and $k_{off}$ for each state by setting $k_{off}$ equal to the relaxation rate obtained from rheometry (**Supplementary Figure 1.2**), then using the $k_{on}^*/k_{off}$ ratios calculated from FRAP (**Table 1.1**). Independent estimates of $R_b$ from Flory theory ($R \sim bN^{3/5}$) (*28*), light-scattering measurements on unstructured amino acid midblocks (*46*), and a geometric argument based on binding site density suggest $R_b$ = 7.8 – 13.7 nm for an ideal PEP network. These estimates provide $[b]_{eq}D_b \approx 0.0023D_{eff}$ for bound chains and $[d]_{eq}D_d \approx 0.0029D_{eff}$ for dangling chains, whereas $[f]_{eq}D_f \approx 1.00D_{eff}$. Other modes of bound mobility, including diffusion of chains in large-scale clusters, are excluded by a similar analysis.

We can appreciate why hopping dominates the mobility of PEP chains by considering the hopping radius $R^*$ in relation to $R_b \approx R_{mesh}$. From **Eq. 2** we estimate that the average distance of a hop is $R^*$ = 1100 ± 240 nm, roughly 100-fold larger than $R_{mesh}$. Hence an escaped chain can diffuse many times its own length (past multiple potential binding sites) before rebinding. This result is consistent with a conceptual picture of a network linked together through well-formed coiled-coil junctions, in which most potential binding sites are fully occupied. Recently, Tang et al. invoked a non-zero bound state mobility in order to explain anomalous

self-diffusion behavior observed by forced Rayleigh scattering (FRS) in a reversible protein hydrogel assembled from chains with four coiled-coil P blocks per chain (*47*). Bound mobility (possibly in the form of large clusters) is likely to be more significant in these gels, due to the much smaller fraction of free chains.

### 1.4.5 Tuning chain mobility with protein engineering

Reversible network association of the P domain reduces the effective diffusivity of PEP chains by two orders of magnitude. Given the programmability of coiled-coil assembly (*48*), we imagined that it should be possible to control the effective diffusivity of a PEP chain by tuning the binding affinity of the P domain. In solution, coiled-coil assembly is driven by hydrophobic interactions between P domains (*43*). In the pentameric bundle, 48% of the total solvent-accessible area arising from the five individual helices is buried, demonstrating the critical role played by hydrophobic interactions in stabilizing the pentamer (*27*). We hypothesized that the hydrophobic leucine (Leu) contacts known to direct oligomerization of the P domain are also critical for reversible network association of a PEP chain.

Site-directed mutagenesis was performed on both ends of the original $PE_CP$ probe to examine whether replacement of critical Leu residues would increase chain mobility. Guided by previous mutagenesis studies on the P domain (*43*), we made a single Leu → Ala mutation (L37A) within each terminal coil, which we predicted would reduce the thermodynamic driving force for oligomerization of the probe. L37 occupies the *a*-position of one of the heptad repeats of P (**Figure 1.5A**). Residues at the *a*-positions line the hydrophobic interior of the pentameric helical bundle, and their mutation to Ala destabilizes the assembly (*43*).

We observed more rapid fluorescence recovery in PEP networks labeled with $PE_CP$-L37A as compared to unmodified $PE_CP$ (**Figure 1.5A**). We attribute the faster recovery behavior to a reduction in the strength of association of the mutant probe with network junctions, consistent with the previously reported low helicity and monomeric oligomerization state of P domains carrying the L37A mutation (*43*).

The enhanced mobility of the $PE_CP$-L37A probe illustrates the importance of hydrophobic interactions in network assembly, and suggests that increasing the hydrophobic character of the P domain should reduce chain mobility by increasing the strength of network association. We previously reported that replacement of Leu by (*2S,4S*)-2-amino-4-methylhexanoic acid (homoisoleucine, Hil), a leucine surrogate with expanded hydrophobic surface area, significantly increases the thermostability of dimeric coiled-coil assemblies (*49*). We hypothesized that replacement of the Leu residues in $PE_CP$ by Hil (**Figure 1.5A**) might reduce probe mobility.

To test this hypothesis, we prepared $PE_CP$-Hil probes in which ca. 92% of all Leu residues were replaced by Hil (see **Supplementary Figures 1.8**, **1.9** and **Supplementary Table 1.2** for details). In contrast to the accelerated recovery behavior of the $PE_CP$-L37A mutant probe, recovery of the $PE_CP$-Hil probe was slower than that of $PE_CP$ (**Figure 1.5B**). Moreover, probes containing both Hil and Leu exhibited intermediate rates of recovery (ca. 53% replacement, **Supplementary Figure 1.10**). This confirms that the reduced rate of fluorescence recovery derives from a differential association of the $PE_CP$-Hil probes with the PEP network junctions.

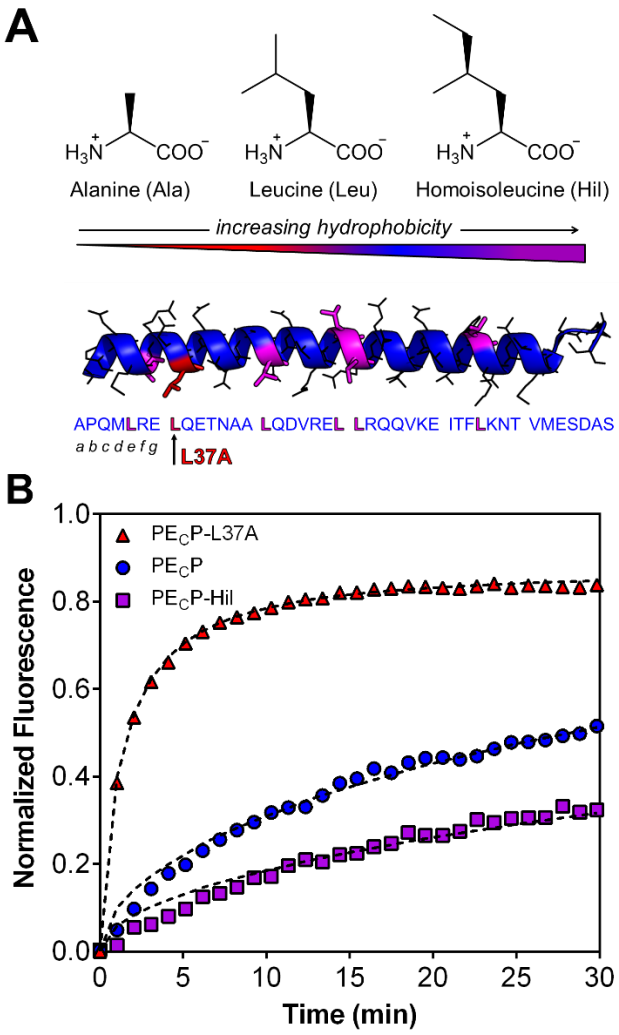


**Figure 1.5. Genetic manipulation of the P domain controls the effective mobility of PE$_C$P probes.** (**A**) PyMOL rendering of a single P domain α-helix showing the location of key Leu residues (purple). An Ala mutation at position 37 (red) is known to destabilize binding, and was predicted to increase probe mobility. Global replacement of Leu with the non-canonical amino acid Hil was predicted to increase the hydrophobic surface area of the probe and decrease its mobility. (**B**) FRAP of the engineered probes. PE$_C$P-L37A shows accelerated fluorescence recovery relative to PE$_C$P, whereas PE$_C$P-Hil shows slower recovery. Dashed lines depict fits generated from the effective diffusion model.

**Table 1.1. Summary of FRAP results determined from engineered probes in 10% PEP hydrogels.** Values represent mean ± standard deviation ($a$ = 10 – 12.5 μm, $n \geq 4$ recovery curves from at least two gel preparations per probe). Results for the $PE_C$ probe are determined from the 2-state model (**Eq. 3**, $N$ = 1); $k_{on}^*/k_{off}$ for this probe reflects $K_1$. Results for $PE_CP$-type probes are calculated from the 3-state model (**Eq. 3**, $N$ = 2) with $D_f = 2.9 \pm 0.4 \times 10^{-8}$ cm$^2$ s$^{-1}$, and assuming $K_1 = K_2 = k_{on}^*/k_{off}$.

| ***Probe*** | ***Mw* (kDa)** | $D_f$, $D_{eff}$ ($10^{-10}$ cm$^2$ s$^{-1}$) | $k_{on}^*/k_{off}$ | $[f]_{eq}$ | $[b]_{eq}$ | $K_d$ (μM) | $\Delta G_a$ (kcal mol$^{-1}$) |
|---|---|---|---|---|---|---|---|
| $AE_CA$ | 20.9 | 270 ± 190 | - | 1.000 | - | - | - |
| $E_C$ | 17.7 | 420 ± 50 | - | 1.000 | - | - | - |
| $PE_C$ | 25.4 | 12.3 ± 1.4 | 26.5 ± 4.5 | 0.036 | - | 47 ± 5 | -5.9 ± 0.1 |
| $PE_CP$ *pred* | 32.2 | 0.4 ± 0.1 | 26.5 ± 4.5 | - | - | - | - |
| $PE_CP$ *obs* | 32.2 | 2.1 ± 0.5 | 11.7 ± 1.8 | 0.007 | 0.914 | 108 ± 13 | -5.4 ± 0.1 |
| $PE_CP$-L37A | 32.1 | 51 ± 17 | 1.9 ± 0.7 | 0.174 | 0.531 | 720 ± 190 | -4.3 ± 0.2 |
| $PE_CP$-Hil | 32.4 | 0.68 ± 0.09 | 20.3 ± 1.4 | 0.002 | 0.951 | 62 ± 4 | -5.7 ± 0.04 |

## 1.5 Conclusion

We have reported a FRAP-based method for characterizing strand exchange and polymer self-diffusivity in associative protein hydrogels. The application of this method relies on a novel 3-state reaction-diffusion model of the strand exchange process. In this model, polymer chains move by a process called "hopping": the chains are free to diffuse spatially throughout the polymer network, unless trapped by reversible association with network junctions. This model fits our experimental FRAP curves well, and permits extraction of diffusion coefficients and equilibrium constants. We find that reversible network association exerts significant control over the effective mobility of individual chains. This allows the effective

mobility "$D_{eff}$" to be tuned over a 500-fold range for probes that are all nominally the same size (**Table 1.1**), via simple changes in chain sequence. The formalism of the 3-state model also enables explicit prediction of $D_{eff}$ from an underlying knowledge of the binding strength $k_{on}^{*}/k_{off}$ and the free diffusivity $D_f$. The hopping mobility predicted by this formalism significantly underestimates the observed mobility. We interpret this discrepancy as indicating inequality of the equilibrium constants that control sequential binding to the network. Brownian Dynamics simulations support this interpretation, and suggest that the asymmetry in binding arises from an entropic constraint on the association of dangling chains due to local network structure. Importantly, such binding asymmetry is likely to be a general feature of reversible gels. Rigorous testing of this hypothesis is described in Chapter 2. Taken together, our results demonstrate that FRAP is well-suited to probing diffusion and binding in protein hydrogels, and that facile protein engineering techniques afford a remarkable level of control over chain mobility in these systems.

### 1.6 Acknowledgments

We thank Steven Olsen and the Division of Chemistry and Chemical Engineering Instrument Shop for machining sample holders for the FRAP experiments. We also thank David Koos, Andres Collazo and the Biological Imaging Facility of the Caltech Beckman Institute for training and assistance in operating the confocal microscope. We thank John Bagert, Lawrence Dooling, and Cole DeForest for helpful discussions during the preparation of the chapter.

## 1.7 Supporting Information

### 1.7.1 Materials and Methods

**Plasmids.** PEP was encoded on a pET15b vector (*50*). Insertion mutagenesis was performed on pET-15b-PEP at the center of the elastin-like midblock to yield pET15b-$PE_CP$, i.e. PEP with a cysteine in the elastin domain. To construct the $PE_CP$-L37A mutant, site-directed mutagenesis was performed on both "L37" residues in pQE15b-$PE_CP$ using "QuikChange" mismatch primers amplified by PfuUltraII HS Fusion Polymerase (Agilent Technologies). The L37A mutations in both P blocks were confirmed by forward and reverse sequencing, and by MALDI-MS on trypsinized $PE_CP$-L37A. Incorporation of homoisoleucine (Hil) was achieved by placing $PE_CP$ into a modified pQE80L vector (pQE80L-LeuRS), containing a copy of the *leuRS* gene flanked by *Nhe*I sites downstream of the multiple-cloning site in pQE-80L. The pQE80L-LeuRS vector drives constitutive overexpression of leucyl-tRNA synthetase. Protein $PE_C$ encoded in pQE-80L was the kind gift of Larry Dooling. $AE_CA$ was the kind gift of Dr. Wenbin Zhang, and $E_C$ was prepared by QuikChange mutagenesis on a pQE80L plasmid encoding the E domain only. All plasmids used and their corresponding coding sequences are presented in **Supplementary Table 1.1**.

**Protein Expression and Purification.** Plasmids coding for the proteins of interest were transformed into either BL21 (DE3) competent *E. coli* or the leucine auxotroph DH10B (for Hil incorporation). In order to express the polymers, cells transformed with the relevant vectors were cultured overnight, and the overnight cultures (typically 10 mL) were used to

inoculate 1 L flasks containing Terrific Broth (TB) supplemented with 100 – 200 mg $ml^{-1}$ ampicillin. Cells were grown to an $OD_{600}$ of 0.7 – 1.0 and then induced with 1 mM isopropyl β-D-1 thiogalactopyranoside (IPTG). After 4-5 h, bacterial cultures were harvested by centrifugation for 5-10 min at 10,000*g*, and cells were lysed with 8 M urea. Cell lysates were freeze-thawed at least once before being subjected to high-power tip sonication for homogenization (50 mL of lysate from a 1 L culture was typically treated with 30-50 W for 10 min in 0.5 - 1 s pulses). Homogenized lysate was clarified by high-speed centrifugation (30,000*g* for 1 h) and then subjected to standard His-tag purification over Ni-NTA agarose beads (Qiagen). His-purified lysate was dialyzed against 4 L of distilled water at 4 °C. The water was changed repeatedly (5-6 times) over the course of several days. Typically the onset of cloudiness inside the dialysis bag was used as the dialysis endpoint, after which point the aqueous suspensions were lyophilized.

Synthesis of homoisoleucine (Hil, 2-amino-4-methylhexanoic acid, CAS 3570-21-6) was performed following a previously reported procedure (*49*). For expression of proteins containing Hil, we performed a medium-shift with the *E. coli* leucine auxotroph DH10B into Leu-depleted medium supplemented with Hil. Hil is activated by the *E. coli* leucyl-tRNA synthetase (LeuRS) at lower rates than Leu (*49*). In order to achieve high levels of substitution, we prepared a new expression cassette that encoded a constitutively expressed copy of LeuRS downstream of an inducible $PE_CP$ gene (**Supplementary Figure 1.8**). This pQE-80L-$PE_CP$-LeuRS plasmid enabled high levels of LeuRS expression when transformed into the *E. coli* leucine auxotroph DH10B. Expression of $PE_CP$ was then induced from this plasmid in minimal media supplemented with different ratios of Hil to

Leu. Single colonies of DH10B transformed with pQE-80L-$PE_CP$-LeuRS were used to inoculate 5 mL overnight cultures of M9 minimal medium containing glucose (0.4% w/v), thiamine HCl (35 mg $L^{-1}$), 1 mM $MgSO_4$, 0.1 mM $CaCl_2$, and all 20 amino acids (40 mg $L^{-1}$) supplemented with 200 mg $L^{-1}$ ampicillin. In large-scale (1 L) expressions, overnight cultures were inoculated into fresh M9 + 20 AA media and grown with agitation at 37 °C until the $OD_{600}$ reached 0.8 – 1.0. Cells were pelleted at 6,000*g* for 5-10 min at 4 °C, washed 3 times in ice-cold NaCl (0.9% w/v) and resuspended in fresh M9 media containing 500 $\mu$M of (2*S*,4*S*)-Hil with or without Leu. Cultures were then shaken at 37 °C for 15 min before induction with 1 mM IPTG. After 5 h, cells were harvested and the proteins purified as described above. The extent of replacement of Leu by Hil was estimated by MALDI mass spectrometry (**Supplementary Figure 1.9** and **Supplementary Table 1.2**). For $PE_CP$ expressed in Leu-depleted medium supplemented with 500 $\mu$M Hil, the extent of replacement was ca. 92%. The replacement level was reduced to 53% by including 100 $\mu$M Leu in the expression culture (see column "Leu + Hil" in **Supplementary Table 1.2**).

**Labeling of Probes with Fluorescein-5-Maleimide.** Fluorescent hydrogels were prepared by adding low concentrations of a fluorescently labeled PEP analogue to normal PEP networks. For example, PEP containing a single cysteine residue in its elastin-like midblock ($PE_CP$) was site-specifically conjugated to fluorescein. For conjugation, 100 $\mu$M $PE_CP$ was typically dissolved in 8 M urea, pH 7.5 – 8, supplemented with 100 mM $NaH_2PO_4$. Tris-(2-Carboxyethyl)phosphine Hydrochloride (TCEP, ThermoFisher Scientific) was added to a final concentration of 2 mM, giving a 20:1 ratio of reducing agent to protein. This solution was reduced for 30 min before addition of fluorescein-5-

maleimide (*f5m*, Pierce) to a final concentration of 1 mM. Fluorophore was incubated with protein for 2 – 4 h at room temperature in order to label free thiols. Afterward, iodoacetamide (IAM) was added to a final concentration of 2 mM to alkylate remaining thiols. Alkylation with IAM was typically performed overnight at 4 °C. Labeled polymer was separated from unreacted dye by purification over Ni-NTA agarose. The extent of polymer labeling was estimated to be roughly 0.5 moles label per mole of polymer based on absorption measurements at 488 nm and comparison to free fluorescein-5-maleimide in a solution of dilute (1% *v/v*) 2-mercaptoethanol. A small amount of $PE_CP$-*f5m* was mixed with solutions of unlabeled PEP. Solutions with $PE_CP$:PEP mass ratios of 1:50 or 1:100 were typically prepared. These solutions were dialyzed against distilled water and lyophilized. Similar to unlabeled networks, addition of phosphate buffer to lyophilized protein containing fluorescent $PE_CP$-*f5m* resulted in optically clear, fluorescent hydrogels after several hours on ice.

**Rheological Measurements**. Oscillatory shear rheometry was conducted on labeled and unlabeled PEP hydrogels using an ARES-RFS strain-controlled rheometer (TA Instruments) equipped with parallel-plate and cone-and-plate geometries. The outer edge of the plate was coated with mineral oil to minimize evaporation. Sample temperature was maintained at 25 °C. Strain sweeps identified a linear regime between 0.1 and 10% strain at 10 rad $s^{-1}$. Frequency sweeps were performed at a fixed strain amplitude of 1% between 0.1 and 100 rad $s^{-1}$.

**Fluorescence Recovery After Photobleaching**. After retrieval of the raw fluorescence recovery data from the Zen 2009 software, the data were typically normalized using two separate transformations. The following function normalizes the recovery curve to a range of [0, 1]:

$$f(t) = \frac{F(t)/F_{\infty}(t)}{F(t_0)/F_{\infty}(t_0)}$$

Following this first normalization, the data were typically scaled such that $f(t_0) = 0$ in order to enable fitting of the experimental curves to the simulated curves (which all begin at $f = 0$). This scaling was accomplished using

$$\bar{f}(t) = \frac{f(t) - \min[f(t)]}{\max[f(t)] - \min[f(t)]}$$

In some instances, the experimental curve given by scaled $f(t)$ appeared to not be recovering to its maximum value of 1, even after long times. This may be due to a small fraction of immobile probes in the network. In instances where full recovery was not observed, the simulated fluorescence recovery (generated by the model) was sometimes multiplied by a scalar constant $m$ representing the total fraction of mobile network chains in order to produce better fits to the data. In cases where this "mobile fraction" fit was required, $m$ was typically found to be between 0.8 and 1.0 (i.e. less than 20% of the chains were treated as immobile).

In experiments with the non-binding probes ($AE_CA$ and $E_C$), we frequently observed normalized fluorescence recovery values that moderately exceeded the pre-bleach spot

intensity (see **Supplementary Figure 1.6** below for an example). In these cases, the [min, max] scaling above was essential for properly experimental modeling.

### 1.7.2 Simulation Details

To explore possible binding asymmetry (differences between $K_1$ and $K_2$), we performed coarse-grained Brownian Dynamics simulations of gel-forming telechelic polymers. As described above, we used a standard Kremer-Grest model with beads at the ends of the chains ("stickers") interacting through a Lennard-Jones (LJ) potential that was truncated and shifted to zero at $2.5\sigma_{LJ}$ (such that the stickers experience the attractive portion of the potential) and assigned a well depth of $\epsilon_s$ (*45*). The LJ potential for all other bead pairs was truncated and shifted at $2^{1/6}\sigma_{LJ}$ (such that the potential is purely repulsive) and assigned a well depth of $\epsilon = kT$ (where $kT$ is the thermal energy). All lengths are expressed in units of the LJ diameter $\sigma_{LJ}$ which we set to unity. The chain connectivity is described with a FENE potential using a spring constant of $k$ = 30 and a fully stretched bond length of $R_0$ = 1.5 (both of which are expressed in terms of reduced LJ units $\epsilon = \sigma_{LJ} = 1$). We used a system box size of $V = L^3$ with $L = 4.1R_f$, where $R_f \approx 15.3$ is the equilibrium end-to-end distance of free chains. We imposed periodic boundary conditions in all directions. The bead number density was $\rho$ = 0.12, ensuring that the solution is semi-dilute ($\rho \approx 1.6\rho^*$, where $\rho^*$ is the overlap concentration).

We used Langevin dynamics to evolve the system:

$$m\ddot{r} = f_p + f_b - \zeta\dot{r}$$

where $r$ and $f_p$ are, respectively, the particle position and interparticle force, and the particle mass $m$ is set at unity. The damping coefficient was set to $\zeta = 1$ to ensure overdamped dynamics. The Brownian force $f_b$ was taken to be white noise with a mean of 0 and a variance of $2kT\zeta$. We integrated using a timestep of $\delta t = 0.003$. To reach the equilibrium state for $\epsilon_e = 4.5$, the sample was annealed at a temperature of $kT = 4.5$ for a duration of $2\tau_R$ (where $\tau_R$ is the Rouse time of the system), followed by quenching to $kT = 1$ over a period of $5\tau_R$. We then further equilibrated each sample for $5\tau_R$. The data (e.g. state fractions, $P(R)$, and $g(R)$) were then collected over a period of $20\tau_R$.

To characterize the state of a chain (e.g. free, bound, etc.) we must first define the junctions of the gel. We define junctions as groups of two or more associating stickers. Stickers within a cutoff distance of 1.5 (capturing the attractive portion of the LJ potential-well) are deemed associating and grouped into the same junction.

### 1.7.3 Derivation of the analytical solution to the 3-state model

The 3-state reaction-diffusion model of strand exchange considers three sequential states in equilibrium that describe the process of network association for PEP chains:

$$f \underset{}{\overset{K_1}{\rightleftharpoons}} d \underset{}{\overset{K_2}{\rightleftharpoons}} b \qquad \textbf{(Eq. S1)}$$

In this model, the free chain *f* must undergo two separate association events in order to become fully bound *b* or network associated. An intermediate dangle state *d* appears in which only one of the two P domains participates in a network junction. This situation is depicted graphically in **Figure 1.3** and **Supplementary Figure 1.3.** Sprague et al.

developed a FRAP model for analyzing probe diffusion when the probe itself undergoes a single binding reaction (2-state), or two independent binding reactions with structurally unrelated binding sites (alternative 3-state) (*18*). We sought to extend their analysis of a 2-state system to a 3-state system with sequential binding reactions. The analysis below closely follows their development of an analytical solution for the 2-state system (see especially their Appendix). In our case, a material balance on (**Eq. S1**) results in the following system of coupled reaction-diffusion equations, where [*A*] denotes the molar concentration of a given species *A*:

$$\frac{\partial[f]}{\partial t} = D_f \nabla^2[f] - k_{on}^*[f] + k_{off}[d]$$

$$\frac{\partial[b]}{\partial t} = k_{on}^*[d] - k_{off}[b] \qquad \textbf{(Eq. S2)}$$

$$\frac{\partial[d]}{\partial t} = k_{on}^*[f] - (k_{off} + k_{on}^*)[d] + k_{off}[b]$$

Here we use are using the pseudo-first-order rate constant $k_{on}^*$, which is equal to the true second-order rate constant $k_{on}$, multiplied by the equilibrium molar concentration of binding sites $[S]_{eq}$ (see **Eq. S26** and **S27** below). Immediately following a photobleach, visible fluorophore is depleted in all three states within a cylinder of radius *a* that extends through the entire sample. Outside the radius of this cylinder, visible fluorophore remains at its equilibrium concentration. Because the photobleach is symmetric along the *z*-axis of the cylinder, only lateral diffusion in a single 2D plane needs to be considered. The initial conditions are:

$$f(r,t_0)=\begin{cases}0 & r\le a\\ [f]_{eq} & r>a\end{cases}$$

$$b(r,t_0)=\begin{cases}0 & r\le a\\ [b]_{eq} & r>a\end{cases} \qquad \textbf{(Eq. S3)}$$

$$d(r,t_0)=\begin{cases}0 & r\le a\\ [d]_{eq} & r>a\end{cases}$$

It is convenient to normalize the equilibrium concentrations of each species with the requirement

$$[f]_{eq}+[d]_{eq}+[b]_{eq}=1 \qquad \textbf{(Eq. S4)}$$

At equilibrium, the concentration of each species may be found using the steady-state condition

$$\frac{\partial[f]}{\partial t}=\frac{\partial[d]}{\partial t}=\frac{\partial[b]}{\partial t}=0$$

Applying this condition to (**Eq. S2**) together with (**Eq. S4**) results in the following relations for the equilibrium concentration of each species:

$$\frac{1}{[f]_{eq}}=1+\left(\frac{k_{on}^{*}}{k_{off}}\right)+\left(\frac{k_{on}^{*}}{k_{off}}\right)^2$$

$$\frac{1}{[d]_{eq}}=1+\left(\frac{k_{off}}{k_{on}^{*}}\right)+\left(\frac{k_{on}^{*}}{k_{off}}\right) \qquad \textbf{(Eq. S5)}$$

$$\frac{1}{[b]_{eq}} = 1 + \left(\frac{k_{off}}{k_{on}^{*}}\right) + \left(\frac{k_{off}}{k_{on}^{*}}\right)^2$$

We can also define a pseudo equilibrium constant $K_{eq}$ as the ratio of gel-bound/free chains, which from the steady-state assumption can be shown to be:

$$K_{eq} = \frac{[b]_{eq}}{[f]_{eq}} = \left(\frac{k_{on}^{*}}{k_{off}}\right)^2 \qquad \textbf{(Eq. S6)}$$

It is convenient to make the following variable transformations:

$$\begin{aligned} u &= [f]_{eq} - f \\ v &= [b]_{eq} - b \\ w &= [d]_{eq} - d \end{aligned} \qquad \textbf{(Eq. S7)}$$

Using (**Eq. S7**), we can transform the system of equations in (**Eq. S2**) as follows.

$$\begin{aligned} \frac{\partial u}{\partial t} &= D_f \nabla^2 u - k_{on}^{*} u + k_{off} w \\ \frac{\partial v}{\partial t} &= k_{on}^{*} w - k_{off} v \\ \frac{\partial w}{\partial t} &= k_{on}^{*} u - (k_{on}^{*} + k_{off}) w + k_{off} v \end{aligned} \qquad \textbf{(Eq. S8)}$$

Furthermore, the initial conditions in (**Eq. S3**) now become

$$u(r,t_0)=\begin{cases}[f]_{eq} & r\le a\\ 0 & r>a\end{cases}$$

$$v(r,t_0)=\begin{cases}[b]_{eq} & r\le a\\ 0 & r>a\end{cases} \qquad \textbf{(Eq. S9)}$$

$$w(r,t_0)=\begin{cases}[d]_{eq} & r\le a\\ 0 & r>a\end{cases}$$

With this change of variables, we are now in a position to apply the Laplace transformation to the system in (**Eq. S8)**. This transformation is given by

$$F(s)=L\{f(t)\}(s)=\int_0^\infty e^{-st}f(t)dt$$

After transformation into Laplace space, the new system of equations becomes:

$$s\bar{u}=D_f\nabla^2\bar{u}-k_{on}{}^*\bar{u}+k_{off}\bar{w}+\bar{u}(0) \qquad \textbf{(Eq. S10)}$$

$$s\bar{v}=k_{on}{}^*\bar{w}-k_{off}\bar{v}+\bar{v}(0) \qquad \textbf{(Eq. S11)}$$

$$s\bar{w}=k_{on}{}^*\bar{u}-(k_{on}{}^*+k_{off})\bar{w}+k_{off}\bar{v}+\bar{w}(0) \qquad \textbf{(Eq. S12)}$$

Here $\bar{u}$ has been used to distinguish the Laplace-domain variable from the time-domain variable *u*. In order to solve this system, at least one of the above expressions needs to be written in terms of a single variable. This can be achieved with (**Eq. S10**) by expressing *w* in terms of *u* using (**Eq. S11**) and (**Eq. S12**). Towards this goal, (**Eq. S11**) is first used to solve for *v*(*s*) in terms of *w*, which gives

$$\bar{v} = q_v(s)[k_{on}^{*}\bar{w} + \bar{v}(0)] \quad \textbf{(Eq. S13)}$$

where

$$q_v(s) \equiv \frac{1}{s + k_{off}} \quad \textbf{(Eq. S14)}$$

Next (**Eq. S13**) can be substituted into (**Eq. S12**) to get *w* in terms of *u*

$$\bar{w} = q_w(s)[k_{on}^{*}\bar{u} + k_{off}q_v\bar{v}(0) + \bar{w}(0)] \quad \textbf{(Eq. S15)}$$

where

$$q_w(s) \equiv \frac{1}{s + k_{on}^{*} + k_{off} - k_{on}^{*}k_{off}q_v} \quad \textbf{(Eq. S16)}$$

Finally, (**Eq. S16**) can be substituted into (**Eq. S10**) which yields a differential equation in terms of *u* only. This equation has the simplified form

$$\nabla^2\bar{u} - q_u(s)^2\bar{u} = \begin{cases} -V & r \le a \\ 0 & r > a \end{cases} \quad \textbf{(Eq. S17)}$$

where $q_u$ and $V$ are defined as

$$q_u(s)^2 \equiv \left(\frac{1}{D_f}\right)[s + k_{on}^{*} - k_{off}k_{on}^{*}q_w] \quad \textbf{(Eq. S18)}$$

$$V \equiv \left(\frac{1}{D_f}\right)[(k_{off})^2 q_w q_v\bar{v}(0) + k_{off}q_w\bar{w}(0) + \bar{u}(0)] \quad \textbf{(Eq. S19)}$$

Here a "nested function" approach has been used to simplify the forms of (**Eq. S17** – **S19**). This conceals the underlying algebraic complexity of (**Eq. S17**). Despite this complexity, the equation has a known solution of the form

$$\bar{u}_1 = \frac{V}{q_u^{\,2}} - \alpha_1 I_0(q_u r), \quad r \le a$$

$$\bar{u}_2 = \alpha_2 K_0(q_u r), \quad r > a$$

where $I_0$ and $K_0$ are modified Bessel functions of the first and second kind, respectively. To determine the constants $\alpha_1$ and $\alpha_2$, we require that $u$ and its first derivative be continuous at the bleach spot boundary $r = a$. Using this continuity requirement and the Bessel function relationships $I_0' = I_1$ and $K_0' = -K_1$, we arrive at the following expression for $\alpha_1$

$$\alpha_1 = \left( \frac{V}{q_u^{\,2}} \right) q_u a K_1(q_u a) \qquad \textbf{(Eq. S20)}$$

In the time domain, what is actually measured is the average fluorescence intensity of all three states within the circular spot, i.e.

$$\langle f(t,r) \rangle = \langle f + d + b \rangle = \langle [f]_{eq} - u + [d]_{eq} - w + [b]_{eq} - v \rangle = 1 - \langle u + v + w \rangle$$

The Laplace transformation of this profile is

$$F(s,r) = \frac{1}{s} - \langle \bar{u} \rangle - \langle \bar{v} \rangle - \langle \bar{w} \rangle \qquad \textbf{(Eq. S21)}$$

The only term that depends on *r* in (**Eq. S21**) is *u*, so it suffices to compute the average for *u*. This can be done with the integral:

$$\langle \bar{u}(s) \rangle = \frac{1}{\pi a^2} \int_0^{2\pi} d\theta \int_0^a \left[ \frac{V}{q_u{}^2} - \alpha_1 I_0(q_u r) \right] r dr$$

$$\boxed{\langle \bar{u}(s) \rangle = \left( \frac{V}{q_u{}^2} \right) \left[ 1 - 2K_1(q_u a) I_1(q_u a) \right]} \qquad \textbf{(Eq. S22)}$$

Finally, we can combine all the preceding expressions into the final form

$$F(s,r) = \frac{1}{s} - \langle \bar{u} \rangle - \bar{v} - \bar{w}$$

$$\boxed{F(s,r) = \frac{1}{s} - \left[ 1 + k_{on}{}^* q_w + (k_{on}{}^*)^2 q_w q_v \right] \langle \bar{u}(s) \rangle - Q_{wv}(s)} \qquad \textbf{(Eq. S23)}$$

where

$$\boxed{Q_{wv}(s) = [k_{off} q_w q_v + k_{off} k_{on}{}^* q_w q_v{}^2 + q_v] \bar{v}(0) + [k_{on}{}^* q_w q_v + q_w] \bar{w}(0)} \quad \textbf{(Eq. S24)}$$

We now consider the case in which binding is negligible, i.e. when $k_{on}{}^* \rightarrow 0$ and $k_{off} \rightarrow \infty$. In this case, it is immediately apparent from (**Eq. S14**) and (**Eq. S16**) that $q_v$ and $q_w$ approach zero. A similar analysis of (**Eq. S24**) under the same constraint also leads to the conclusion that $Q_{wv}$ approaches zero. Furthermore, $q_u{}^2$ and $V$ approach $s/D_f$ and $1/D_f$ respectively. These reductions greatly simplify (**Eq. S23**), which can now be written as

$$F(s,r) = \frac{1}{s} - \langle \bar{u}(s) \rangle = \frac{1}{s} - \frac{1}{s} \left[ 1 - 2K_1(q_u a) I_1(q_u a) \right] = \frac{2K_1(q_u a) I_1(q_u a)}{s} \qquad \textbf{(Eq. S25)}$$

Sprague et al. show that this relation is identical to the relation obtained by Soumpasis for a chain diffusing freely in a circular bleach spot (*18*, *30*). To further validate our solution, we compared curves obtained by inversion of (**Eq. S23**) with those obtained by numerical simulation of (**Eq. S8**) and (**Eq. S9**) using a finite-difference method. FRAP curves simulated analytically and numerically showed good agreement across multiple values of $k_{on}$, with only minor differences at long times which could be attributed to the finite mesh size used in the difference algorithm (**Supplementary Figure 1.4**).

As discussed in the main text, the parameter $k_{on}^{*}$ is a pseudo-first-order association rate, calculated from the true (second-order) association rate $k_{on}$ by assuming a constant concentration of binding sites $S_{eq}$. The true second-order association rate is:

$$k_{on} = \frac{k_{on}^{*}}{S_{eq}} \qquad \textbf{(Eq. S26)}$$

The maximum molar concentration of equilibrium binding sites can be calculated from the network mass density $\rho$ by assuming that all P domains are active in pentameric bundle formation. In this ideal case, $S_{eq}$ is given by the following relation, where $M$ is the molar mass of a single PEP chain (~32 kDa, **Supplementary Table 1.1**).

$$S_{eq} = \frac{2}{5}\left(\frac{\rho}{M}\right) \qquad \textbf{(Eq. S27)}$$

Use of (**Eq. S26**) and (**Eq. S27**) also permits determination of the dissociation constant $K_d$, which is simply the ratio of $k_{off}$ to $k_{on}$. With $K_d$ it is possible to estimate the free energy of network association $\Delta G_a$ from the relation:

$$\Delta G_a = -RT \ln\left(\frac{1}{K_d}\right) \qquad \textbf{(Eq. S28)}$$

Sprague et al. use the following parameter to describe rate constant parameter space, which is helpful for determining whether fluorescence recovery is primarily governed by either diffusion or binding, or a combination of both.

$$\varphi^2 = \frac{k_{on}^{*} a^2}{D_f} \qquad \textbf{(Eq. S29)}$$

### 1.7.4 *invlap.m*: a MATLAB script for inverse Laplace transformation

The following algorithm may be used to numerically invert the Laplace domain solution in (**Eq. S23**) in order to obtain simulated fluorescence recovery curves in the time domain. The algorithm was originally written by Karl Hollenbeck and should be cited as shown below. The original web link to the algorithm is no longer active.

Hollenbeck, K. J. (1998) INVLAP.M: A MATLAB function for numerical inversion of Laplace transforms by the de Hoog algorithm.
http://www.mathworks.com/matlabcentral/answers/uploaded_files/1034/invlap.m

```
% INVLAP  numerical inverse Laplace transform
%
% f = invlap(F, t, alpha, tol, P1,P2,P3,P4,P5,P6,P7,P8,P9);
%
% F       laplace-space function (string refering to an m-file),
%           must have form F(s, P1,..,P9), where s is the Laplace
parameter,
%           and return column vector as result
% t       column vector of times for which real-space function values
are
%           sought
% alpha   largest pole of F (default zero)
% tol     numerical tolerance of approaching pole (default 1e-9)
% P1-P9   optional parameters to be passed on to F
% f       vector of real-space values f(t)
```

```
%
% example: identity function in Laplace space:
%   function F = identity(s);                    % save these two lines
%            F = 1./(s.^2);                      % ...  as "identity.m"
%   invlap('identity', [1;2;3])                  % gives [1;2;3]
%
% algorithm: de Hoog et al's quotient difference method with
accelerated
%   convergence for the continued fraction expansion
%   [de Hoog, F. R., Knight, J. H., and Stokes, A. N. (1982). An
improved
%    method for numerical inversion of Laplace transforms. S.I.A.M. J.
Sci.
%    and Stat. Comput., 3, 357-366.]
% Modification: The time vector is split in segments of equal magnitude
%   which are inverted individually. This gives a better overall
accuracy.

%  details: de Hoog et al's algorithm f4 with modifications (T->2*T and
%    introduction of tol). Corrected error in formulation of z.
%
%  Copyright: Karl Hollenbeck
%             Department of Hydrodynamics and Water Resources
%             Technical University of Denmark, DK-2800 Lyngby
%             email: karl@isv16.isva.dtu.dk
%  22 Nov 1996, MATLAB 5 version 27 Jun 1997 updated 1 Oct 1998
%  IF YOU PUBLISH WORK BENEFITING FROM THIS M-FILE, PLEASE CITE IT AS:
%    Hollenbeck, K. J. (1998) INVLAP.M: A matlab function for numerical
%    inversion of Laplace transforms by the de Hoog algorithm,
%    http://www.isva.dtu.dk/staff/karl/invlap.htm

function f = invlap(F, t, alpha, tol, P1,P2,P3,P4,P5,P6,P7,P8,P9);

if nargin <= 2,
  alpha = 0;
elseif isempty(alpha),
  alpha = 0;
end
if nargin <= 3,
  tol = 1e-9;
elseif isempty(tol),
  tol = 1e-9;
end
f = [];

% split up t vector in pieces of same order of magnitude, invert one
piece
%   at a time. simultaneous inversion for times covering several orders
of
%   magnitudes gives inaccurate results for the small times.

allt = t;               % save full times vector
logallt = log10(allt);
```

```
iminlogallt = floor(min(logallt));
imaxlogallt = ceil(max(logallt));
for ilogt = iminlogallt:imaxlogallt,    % loop through all pieces

  t = allt(find((logallt>=ilogt) & (logallt<(ilogt+1))));
  if ~isempty(t),           % maybe no elements in that magnitude

    T = max(t)*2;
    gamma = alpha-log(tol)/(2*T);
    % NOTE: The correction alpha -> alpha-log(tol)/(2*T) is not in de
Hoog's
    %   paper, but in Mathematica's Mathsource (NLapInv.m)
implementation of
    %   inverse transforms
    nt = length(t);
    M = 20;
    run = [0:1:2*M]';    % so there are 2M+1 terms in Fourier series
expansion

    % find F argument, call F with it, get 'a' coefficients in power
series
    s = gamma + i*pi*run/T;
    command = ['a = ' F '(s'];
    if nargin > 4,              % pass on parameters
      for iarg = 1:nargin-4,
        command = [command ',P' int2str(iarg)];
      end
    end
    command = [command ');'];
    eval(command);
    a(1) = a(1)/2;              % zero term is halved

    % build up e and q tables. superscript is now row index, subscript
column
    %   CAREFUL: paper uses null index, so all indeces are shifted by 1
here
    e = zeros(2*M+1, M+1);
    q = zeros(2*M  , M+1);          % column 0 (here: 1) does not exist
    e(:,1) = zeros(2*M+1,1);
    q(:,2) = a(2:2*M+1,1)./a(1:2*M,1);
    for r = 2:M+1,                  % step through columns (called
r...)
      e(1:2*(M-r+1)+1,r) = ...
      q(2:2*(M-r+1)+2,r) - q(1:2*(M-r+1)+1,r) + e(2:2*(M-r+1)+2,r-1);
      if r<M+1,                     % one column fewer for q
    rq = r+1;
    q(1:2*(M-rq+1)+2,rq) = ...
     q(2:2*(M-rq+1)+3,rq-1).*e(2:2*(M-rq+1)+3,rq-1)./e(1:2*(M-
rq+1)+2,rq-1);
      end
    end

    % build up d vector (index shift: 1)
```

```
    d = zeros(2*M+1,1);
    d(1,1) = a(1,1);
    d(2:2:2*M,1) = -q(1,2:M+1).'; % these 2 lines changed after niclas
    d(3:2:2*M+1,1) = -e(1,2:M+1).'; % ...

    % build up A and B vectors (index shift: 2)
    %   - now make into matrices, one row for each time
    A = zeros(2*M+2,nt);
    B = zeros(2*M+2,nt);
    A(2,:) = d(1,1)*ones(1,nt);
    B(1:2,:) = ones(2,nt);
    z = exp(i*pi*t'/T);     % row vector
    % after niclas back to the paper (not: z = exp(-i*pi*t/T)) !!!
    for n = 3:2*M+2,
      A(n,:) = A(n-1,:) + d(n-1,1)*ones(1,nt).*z.*A(n-2,:);  %
different index
      B(n,:) = B(n-1,:) + d(n-1,1)*ones(1,nt).*z.*B(n-2,:);  %  shift
for d!
    end

    % double acceleration
    h2M = .5 * ( ones(1,nt) + ( d(2*M,1)-d(2*M+1,1) )*ones(1,nt).*z );
    R2Mz = -h2M.*(ones(1,nt) - ...
    (ones(1,nt)+d(2*M+1,1)*ones(1,nt).*z/(h2M).^2).^.5);
    A(2*M+2,:) = A(2*M+1,:) + R2Mz .* A(2*M,:);
    B(2*M+2,:) = B(2*M+1,:) + R2Mz .* B(2*M,:);

    % inversion, vectorized for times, make result a column vector
    fpiece = ( 1/T * exp(gamma*t') .* real(A(2*M+2,:)./B(2*M+2,:)) )';
    f = [f; fpiece];            % put pieces together

  end % if not empty time piece

end % loop through time vector pieces
```

### 1.7.5 Fitting procedures for experimental FRAP curves

In order to fit simulated curves to experimental curves, the following curve fitting procedures were employed. For the effective diffusion model (**Figure 1.2**), the full model (**Eq. S23**) was used but with the values of $k_{on}^{*}$ and $k_{off}$ fixed at $10^{-5}$ $s^{-1}$ and $10^{5}$ $s^{-1}$ respectively. This was found to be numerically equivalent to fitting the curves with the form derived by Soumpasis (*30*):

$$f(t) = \exp\left(\frac{-\tau_D}{2t}\right)\left[I_0\left(\frac{\tau_D}{2t}\right) + I_1\left(\frac{\tau_D}{2t}\right)\right] \qquad \textbf{(Eq. S30)}$$

where

$$\tau_D = \frac{a^2}{D_f}$$

As discussed by Sprague et al., both (**Eq. S25**) and (**Eq. S30**) are solutions to the simple diffusion equation without any binding. When used to fit curves influenced by binding (i.e., in the effective diffusion regime), the diffusivity resulting from the fit is $D_{eff}$. Curves were fit using the method described in the main text, as well as by the following custom algorithm which gave similar results: (*i*) a guess for the parameter of interest ($D_{eff}$, $D_f$, $k_{on}^*$, $k_{off}$) was drawn from a normal distribution (generated by the MATLAB command `randn`) having a mean and standard deviation equal to an initial seed guess, (*ii*) based on the guess, a new FRAP curve was simulated from (**Eq. S23**) and compared to the experimental curve, (*iii*) the guess was accepted if it lowered the root-mean-square residual of the fit relative to the previous guess, and (*iv*) the next guess was drawn from a new normal distribution having a mean and standard deviation equal to the value of the new best guess for the fitting parameter. This procedure was typically iterated 1000 times, after which point a very good fit had usually been obtained. For fits using the full model, $D_f$ was fixed in an independent experiment (by modeling recovery curves of the $E_C$ probe with the pure diffusion equation), and then guesses for $k_{on}^*$ and $k_{off}$ were simultaneously drawn from independent normal distributions with means and standard deviations equal to the value of the current guess for each rate constant. As with the fits for $D_f$ alone, new guesses were accepted whenever they

lowered the root mean square residual of the fit, and this procedure was iterated 1000 times. Examples of fits resulting from this approach are shown in **Supplementary Figure 1.5**.

### 1.7.6 Derivation of Equation 3

Consider a generalized version of (**Eq. 1**), in which there are $N$ associative "sticky" domains and therefore $N + 1$ total states (including the free state $f$). Assume that the $f$ state has a free diffusivity given by $D_f$, and that the mobility of chains in each of the remaining $N$ states is given by a single non-zero value designated $D_b$ for "bound mobility".

$$f \underset{}{\overset{k_{on}^*/k_{off}}{\rightleftharpoons}} d_i \underset{}{\overset{k_{on}^*/k_{off}}{\rightleftharpoons}} d_{i+1} \cdots \underset{}{\overset{k_{on}^*/k_{off}}{\rightleftharpoons}} \cdots d_{N-1} \underset{}{\overset{k_{on}^*/k_{off}}{\rightleftharpoons}} b_N \quad \textbf{(Eq. S31)}$$

If binding is fast relative to the time it takes to diffuse across the bleach spot, then we can assume local, instantaneous chemical equilibrium at each time throughout the course of fluorescence recovery (*51*). Under this assumption, it is trivial to show that

$$[d_i] \approx \left(\frac{k_{on}^*}{k_{off}}\right)[f]$$

$$[d_{i+1}] \approx \left(\frac{k_{on}^*}{k_{off}}\right)[d_i] = \left(\frac{k_{on}^*}{k_{off}}\right)^2 [f]$$

$$\vdots$$

$$[b_N] \approx \left(\frac{k_{on}^*}{k_{off}}\right)[d_{N-1}] = \left(\frac{k_{on}^*}{k_{off}}\right)^N [f]$$

or more generally that

$$[d_i] \approx \left(\frac{k_{on}^{*}}{k_{off}}\right)^{i} [f] \qquad \text{for } i = 1...N \qquad \textbf{(Eq. S32)}$$

Proceeding to write out the reaction-diffusion equations for each state and then summing them together (all reaction terms disappear during this operation) gives:

$$\frac{\partial[f]}{\partial t} + \frac{\partial[d_i]}{\partial t} + \frac{\partial[d_{i+1}]}{\partial t} + \cdots + \frac{\partial[b_N]}{\partial t} = D_f \nabla^2[f] + D_b\left(\nabla^2[d_i] + \nabla^2[d_{i+1}] + \cdots + \nabla^2[b_N]\right)$$

Supplying (**Eq. S32**) into the above relation gives

$$\left[1 + \left(\frac{k_{on}^{*}}{k_{off}}\right) + \left(\frac{k_{on}^{*}}{k_{off}}\right)^2 + \cdots + \left(\frac{k_{on}^{*}}{k_{off}}\right)^N\right]\frac{\partial[f]}{\partial t} = \left\{D_f + D_b\left[\left(\frac{k_{on}^{*}}{k_{off}}\right) + \left(\frac{k_{on}^{*}}{k_{off}}\right)^2 + \cdots + \left(\frac{k_{on}^{*}}{k_{off}}\right)^N\right]\right\}\nabla^2[f]$$

Letting $\frac{k_{on}^{*}}{k_{off}} = \alpha$ simplifies this to

$$\frac{\partial[f]}{\partial t} = \frac{D_f + D_b\left(\alpha + \alpha^2 + \cdots + \alpha^N\right)}{1 + \alpha + \alpha^2 + \cdots + \alpha^N}\nabla^2[f] = D_{eff}\nabla^2[f]$$

where we have defined $D_{eff}$ as

$$D_{eff} = \frac{D_f + D_b\left(\alpha + \alpha^2 + \cdots + \alpha^N\right)}{1 + \alpha + \alpha^2 + \cdots + \alpha^N} \qquad \textbf{(Eq. S33)}$$

Setting $D_b = 0$ (assume no mobility in the bound state) finally gives

$$\boxed{\frac{D_f}{D_{eff}} = 1 + \alpha + \alpha^2 + \cdots + \alpha^N = 1 + \sum_{i=1}^{N}\left(\frac{k_{on}^{*}}{k_{off}}\right)^i} \qquad \textbf{(Eq. S34)}$$

which is equation (**5**) reported in the main text. Note that (**33**) can be used to estimate the bound state mobility $D_b$ if one relaxes the assumption that $D_b = 0$. In the above analysis, we have assumed symmetric sequential binding such that $K_1 = K_2 = \ldots = K_N = k_{on}^*/k_{off}$. This assumption is easily relaxed by redefining $\alpha$ as $\alpha_i$ where

$$\alpha_i = \left(\frac{k_{on}^*}{k_{off}}\right)_1 \left(\frac{k_{on}^*}{k_{off}}\right)_2 \cdots \left(\frac{k_{on}^*}{k_{off}}\right)_N = K_1 K_2 \cdots K_N = \prod_{j=1}^{i} K_j \qquad \textbf{(Eq. S35)}$$

for $i = 1 \ldots N$

The state fractions become $[d_i] \approx \alpha_i [f]$, which when supplied into the mass balance gives

$$\left[1 + \alpha_1 + \alpha_2 + \cdots + \alpha_N\right] \frac{\partial [f]}{\partial t} = \left\{D_f + D_b \left[\alpha_1 + \alpha_2 + \cdots + \alpha_N\right]\right\} \nabla^2 [f]$$

We can now define a new $D_{eff}$ as

$$D_{eff} = \frac{D_f + D_b \left(\alpha_1 + \alpha_2 + \cdots + \alpha_N\right)}{1 + \alpha_1 + \alpha_2 + \cdots + \alpha_N} \qquad \textbf{(Eq. S36)}$$

which returns us to simple Fickian diffusion governed by the new $D_{eff}$, and the ratio $D_f/D_{eff}$ is (neglecting bound mobility by setting $D_b = 0$)

$$\boxed{\frac{D_f}{D_{eff}} = 1 + \alpha_1 + \alpha_2 + \cdots + \alpha_N = 1 + \sum_{i=1}^{N} \left[\prod_{j=1}^{i} K_j\right] = 1 + K_1 + K_1 K_2 + \cdots + K_1 K_2 \cdots K_N}$$

**(Eq. S37)**

**Eq. S37** allows each equilibrium constant to be treated as an adjustable fitting parameter, and is used above to detect binding asymmetry ($K_1 > K_2$) by setting $D_{eff} = D_{obs}$ for $PE_CP$, after fixing $K_1$ with the measurement from the $PE_C$ probe.

### 1.7.7 Fraction of elastically effective chains estimated from Phantom Network Theory

At 10% (*w*/*v*) the number density of chains is

$$\bar{n} = \rho\left(\frac{N_A}{M}\right) = 1.88 \times 10^{24} \text{ chains} / \text{m}^3$$

and the number density of bundles, assuming every endblock ends up in a pentamer, is

$$\bar{n}_b = \frac{2}{5}\bar{n} = 7.52 \times 10^{23} \text{ bundles } / \text{m}^3$$

From Phantom Network Theory, the fraction of elastically effective chains at 10% is given by ($f = 5$ for pentameric chain junctions):

$$G'_{\infty} \Big/ G_{phantom} = \bar{n}kT\left(1 - \frac{2}{f}\right) = 0.69$$

This set of equations can be used to estimate *G'* for gels prepared at different protein concentrations, as is shown in **Supplementary Figure 1.7**.

### 1.7.8 Supplementary Tables

**Supplementary Table 1.1. Plasmids and sequence information for FRAP probes.** Each "P" domain is highlighted in blue, and key mutations (Leu→Ala) or insertions (Cys) are highlighted in red and underlined. All protein coding sequences were confirmed by DNA sequencing.

| Plasmid | Protein | Molecular Weight (Da) |
|---|---|---|
| *pET15b-PEP* | PEP | 32047 |
| MKGSHHHHHHHVDGSGSGSGSGSGSGAPQMLRELQETNAALQDVRELLRQQVKEITFLKNTVMESD ASGSGSGSGSGSGSGLDGHGVGVPGVGVPGVGVPGEGVPGVGVPGVGVPGVGVPGVGVPGEGVPG VGVPGVGVPGVGVPGVGVPGEGVPGVGVPGVGELYAVTGRGDSPASSAPIATSVPGVGVPGVGVPGE GVPGVGVPGVGVPGVGVPGVGVPGEGVPGVGVPGVGVPGVGVPGVGVPGEGVPGVGVPGVGVPGGL LDGSGSGSGSGSGSGAPQMLRELQETNAALQDVRELLRQQVKEITFLKNTVMESDASGSGSGSGSG SGSGSGLEMHHHHHHK* | | |
| *pET15b-PE$_C$P* | PE$_C$P | 32151 |
| *pQE80L-PE$_C$P-LeuRS* | | |
| MKGSHHHHHHHVDGSGSGSGSGSGSGAPQMLRELQETNAALQDVRELLRQQVKEITFLKNTVMESD ASGSGSGSGSGSGSGLDGHGVGVPGVGVPGVGVPGEGVPGVGVPGVGVPGVGVPGVGVPGEGVPG VGVPGVGVPGVGVPGVGVPGEGVPGVGVPGVGELCYAVTGRGDSPASSAPIATSVPGVGVPGVGVPG EGVPGVGVPGVGVPGVGVPGVGVPGEGVPGVGVPGVGVPGVGVPGVGVPGEGVPGVGVPGVGVPG GLLDGSGSGSGSGSGSGAPQMLRELQETNAALQDVRELLRQQVKEITFLKNTVMESDASGSGSGSG SGSGSGLEMHHHHHHK* | | |
| *pET15b-PE$_C$P-L37A* | PE$_C$P-L37A | 32066 |
| MKGSHHHHHHHVDGSGSGSGSGSGSGAPQMLREAQETNAALQDVRELLRQQVKEITFLKNTVMESD ASGSGSGSGSGSGSGLDGHGVGVPGVGVPGVGVPGEGVPGVGVPGVGVPGVGVPGVGVPGEGVPG VGVPGVGVPGVGVPGVGVPGEGVPGVGVPGVGELCYAVTGRGDSPASSAPIATSVPGVGVPGVGVPG EGVPGVGVPGVGVPGVGVPGVGVPGEGVPGVGVPGVGVPGVGVPGVGVPGEGVPGVGVPGVGVPG GLLDGSGSGSGSGSGSGAPQMLREAQETNAALQDVRELLRQQVKEITFLKNTVMESDASGSGSGSG SGSGSGLEMHHHHHHK* | | |
| *pQE80L-AE$_C$A* | AE$_C$A | 20941 |
| MKGSSHHHHHHVDAHIVMVDAYKPTKLDGHGVGVPGVGVPGVGVPGEGVPGVGVPGVGVPGVGVPGV GVPGEGVPGVGVPGVGVPGVGVPGVGVPGEGVPGVGVPGVGELYAVTGRGDSPACSAPIATSVPGVG VPGVGVPGEGVPGVGVPGVGVPGVGVPGVGVPGEGVPGVGVPGVGVPGVGVPGVGVPGEGVPGVGV PGVGVPGGLLDAHIVMVDAYKPTKLEWKK* | | |
| *pQE80L-E$_C$* | E$_C$ | 17706 |
| MKGSSHHHHHHVDGHGVGVPGVGVPGVGVPGEGVPGVGVPGVGVPGVGVPGVGVPGEGVPGVGVP GVGVPGVGVPGVGVPGEGVPGVGVPGVGELYAVTGRGDSPACSAPIATSVPGVGVPGVGVPGEGVPG VGVPGVGVPGVGVPGVGVPGVGVPGEGVPGVGVPGVGVPGVGVPGVGVPGEGVPGVGVPGVGVPGGLLEW KKM* | | |
| *pQE80L-PE$_C$* | PE$_C$ | 25352 |
| MKGSHHHHHHHVDGSGSGSGSGSGSGAPQMLRELQETNAALQDVRELLRQQVKEITFLKNTVMESD ASGSGSGSGSGSGSGLDGHGVGVPGVGVPGVGVPGEGVPGVGVPGVGVPGVGVPGVGVPGEGVPG VGVPGVGVPGVGVPGVGVPGEGVPGVGVPGVGELYAVTGRGDSPASSAPIATSVPGVGVPGVGVPGE GVPGVGVPGVGVPGVGVPGVGVPGEGVPGVGVPGVGVPGVGVPGVGVPGEGVPGVGVPGVGVPGGL LDGPQGIWGQLECM* | | |

**Supplementary Table 1.2. Quantification of Hil substitution level from MALDI-MS**. Based on the above MALDI spectra, the degree of Hil substitution was calculated for different expression conditions (lanes **5-7** in **Supplementary Figure 1.8B**). In cultures containing Hil and depleted of Leu, a substitution level of 91.8 ± 4.5% was obtained. In cultures containing 500 $\mu$m Hil and 100 $\mu$m Leu, the substitution level was 53.2 ± 10.6%. Cultures grown without Hil contained only Leu. The incorporation levels were determined by integration of MALDI peaks for three peptide fragments.

| | | | | *% of Hil-substituted residues* | | |
|---|---|---|---|---|---|---|
| | | | ***μM*** | **Leu** | **Leu + Hil** | **Leu → Hil** |
| | *Expected MW (Da)* | | **[Leu]** | 300 | 100 | 0 |
| **Peptide** | **+ Leu** | **+ Hil** | **[Hil]** | 0 | 500 | 500 |
| E**LL**R | 529.6 | 557.7 | | - | 65.5% | 94.3% |
| EITF**L**K | 749.9 | 763.9 | | - | 46.9% | 94.5% |
| E**L**QETNAA**L**QDVR | 1486.6 | 1514.6 | | - | 47.1% | 86.6% |
| | | | | ***avg*** | **53.2%** | **91.8%** |
| | | | | *std* | 10.6% | 4.5% |

### 1.7.9 Supplementary Figures

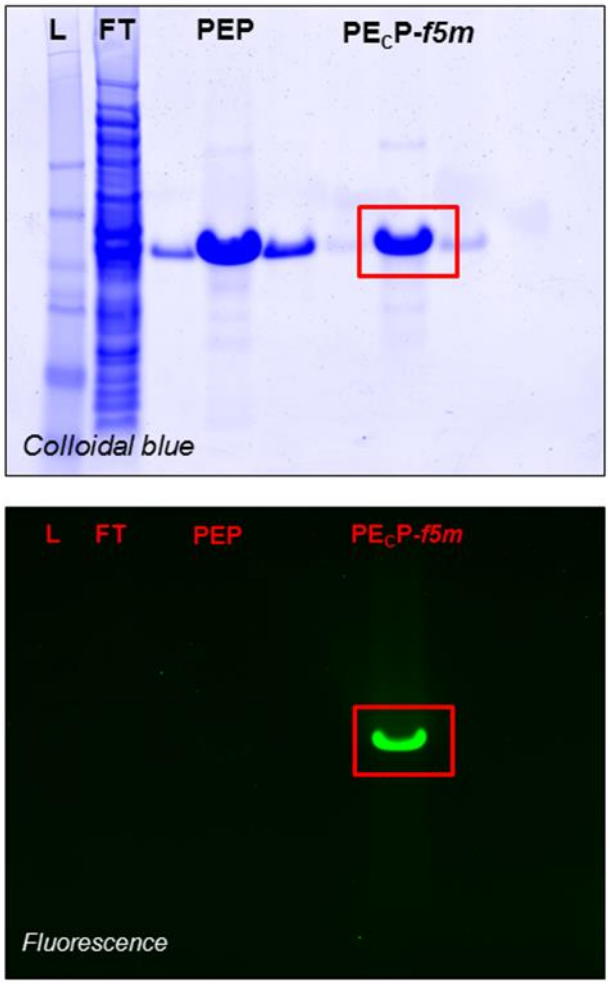


**Supplementary Figure 1.1. Site-specific labeling of PE$_C$P.** SDS-PAGE analysis of unpurified and purified PEP and PE$_C$P constructs. (*Top*) Colloidal blue staining reveals the following bands: **L**, ladder; **FT**, flow-through from His-purification; **PEP**, elution of purified protein from Ni-NTA column; **PE$_C$P**, analogous elution of purified PE$_C$P-*f5m* (labeled with fluorescein-5-maleimide). (*Bottom*) Fluorescence analysis of the same gel shows that fluorophore is conjugated to PE$_C$P-*f5m*.

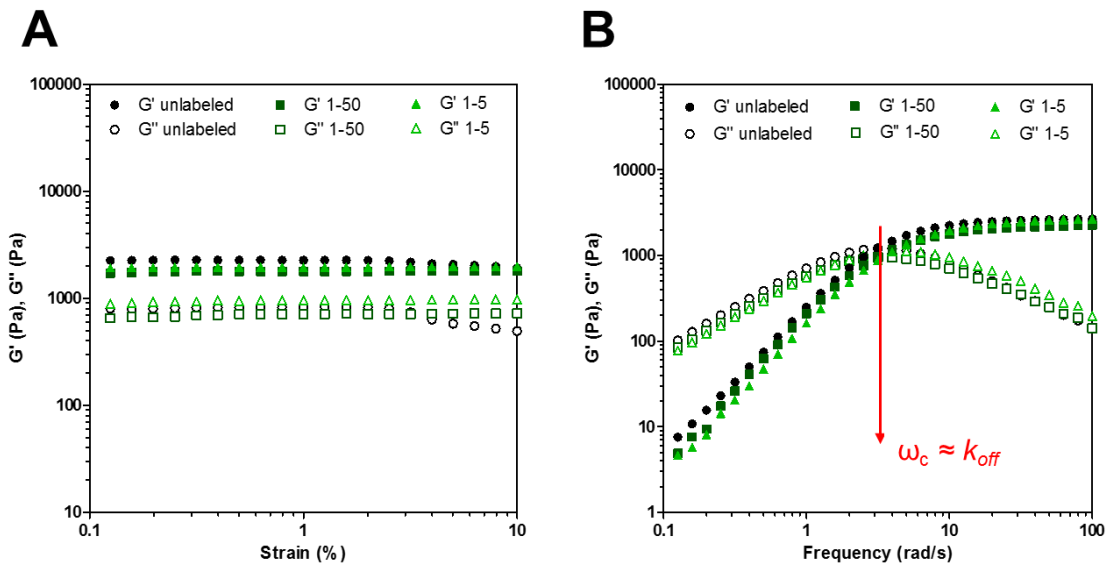


**Supplementary Figure 1.2. Low probe concentrations do not affect network rheology.** Labeling with $PE_CP$-*f5m* (1:5 or 1:50) minimally affects the rheological behavior of 10% PEP networks. (**A**) Strain sweeps at 10 rad $s^{-1}$ show minimal variation in the elastic (*G*') and loss (*G*'') moduli in a linear regime between 0.1 and 10% strain. (**B**) Frequency sweeps at 1% strain show similar frequency-dependent behavior for labeled and unlabeled gels. Data were collected on a parallel plate rheometer (15 mm plate diameter) and a gap width of 250 $\mu$m. The crossover frequency $\omega_c$, which also remains unchanged upon labeling, can be taken as an approximation of the off rate $k_{off}$ (see discussion above).

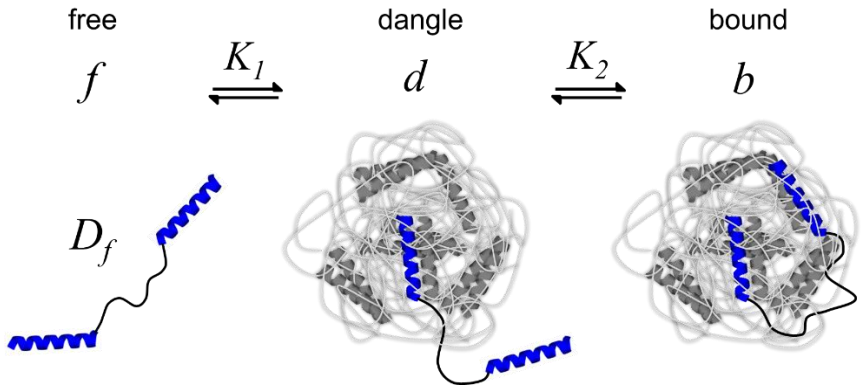


**Supplementary Figure 1.3. Graphical representation of the 3-state reaction-diffusion model.** Free polymer chains *f* diffuse with diffusion coefficient $D_f$ within the network. A chain with one arm bound enters the dangle state *d*. Upon binding of both arms, the chain is in the bound state *b* and, like the dangling chains, assumed to have no spatial mobility because interchain crosslinks constrain its motion. Interconversion between these three states is governed by the equilibrium constants $K_1$ and $K_2$. In developing the analytical solution below, we assume that $K_1 \approx K_2 = k_{on}^*/k_{off}$. This assumption is considered in detail in **Section 1.4**, and can be relaxed (see **Eq. S33 – S37**).

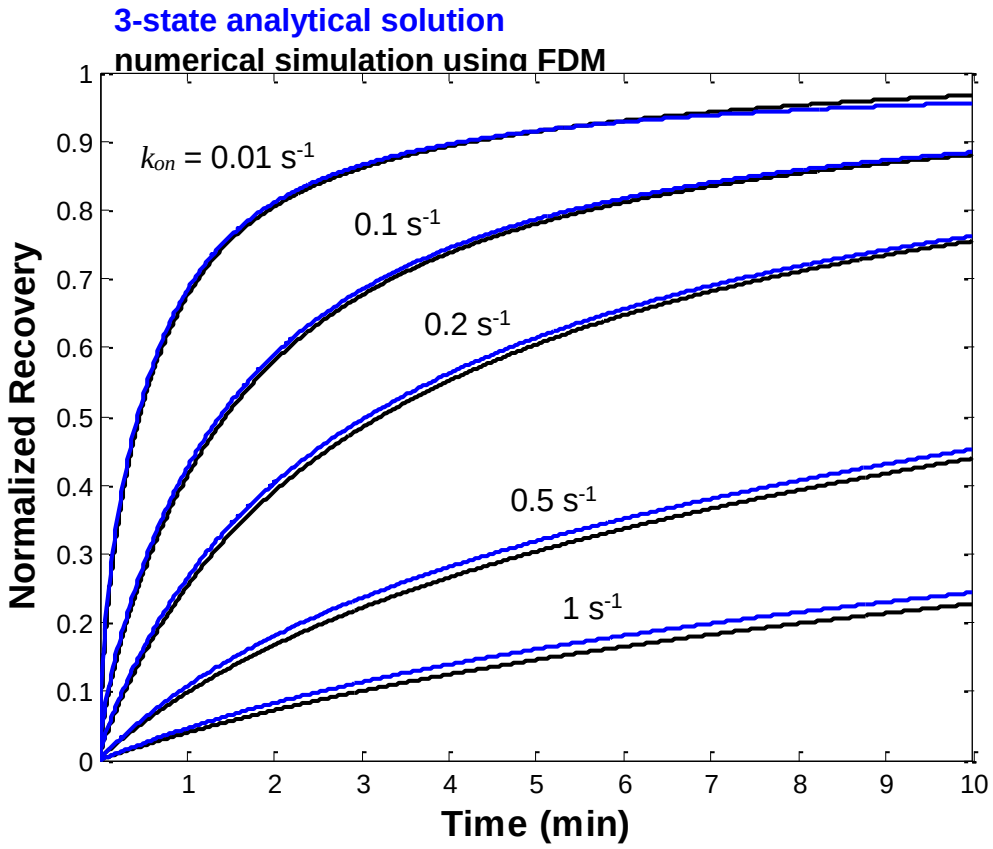


**Supplementary Figure 1.4. Validation of the analytical solution to the 3-state model.** Simulated fluorescence recovery curves obtained by using a finite difference method (FDM, black) and by numerical inversion of (**Eq. S23**), (blue). The parameters used to obtain the simulated curves were $a$ = 10 $\mu$m, $D_f$ = 1 $\mu$m$^2$ s$^{-1}$ and $k_{off}$ = 0.1 s$^{-1}$. The values used for $k_{on}$ are displayed above their corresponding curves. All simulations were performed in MATLAB. The code used to numerically invert the Laplace-domain solution was *invlap.m*, which is included below. The small divergence between curves at higher values of $k_{on}$ (close to ~1 s$^{-1}$) is a result of the finite space discretization in the numerical FDM implementation. The divergence disappears when finer mesh sizes are chosen. Furthermore, simulations out to 60 min indicate that the divergence does not continue to grow at long times.

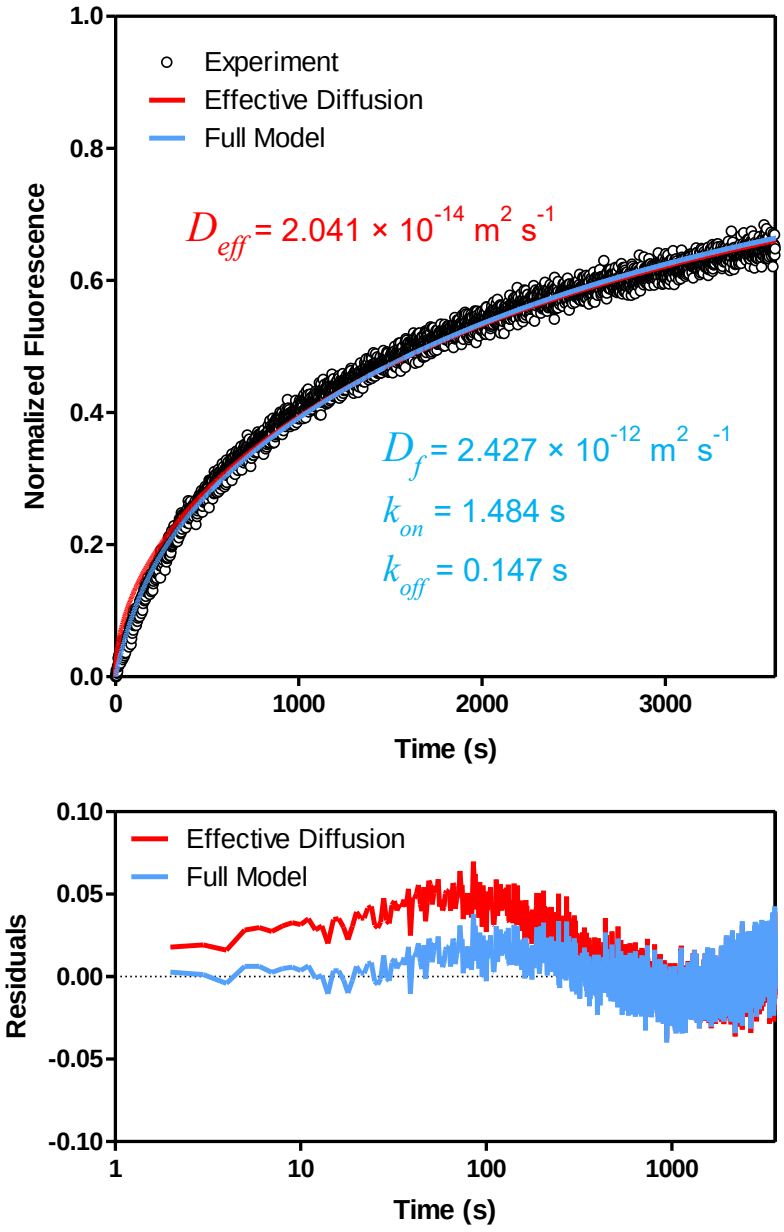


**Supplementary Figure 1.5. Simulated FRAP curves fit to experimental data** (shown for a 10% PEP gel labeled with $PE_CP$). The experimental recovery curve shows excellent agreement with both the full model simulation (blue) and the simplified, effective diffusion model (red). The key parameters extracted from these fits are also listed (*Top*). A residuals analysis of the two curves shows that the full model results in a slightly better fit in this case. In both cases, RMS of all the residuals is < 1 (*Bottom*).

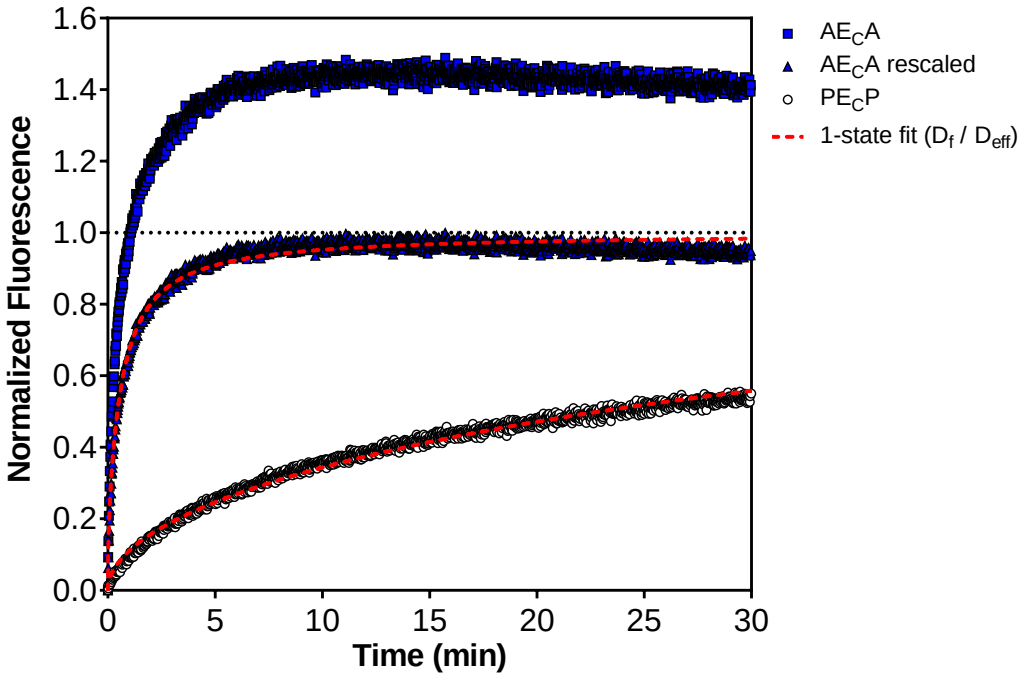


**Supplementary Figure 1.6. Fluorescence recovery curves for AE$_C$A and PE$_C$P in 10% PEP networks.**The final fluorescence intensity for AE$_C$A bleach spots often exceeded the original intensity before the bleach. As a result, AE$_C$A (and E$_C$) recovery curves were typically rescaled before curve fitting such that the maximum fluorescence intensity was equal to 1. Curves for AE$_C$A and PE$_C$P were fit to the 1-state effective diffusion model (**Equation S23** with $k_{on}^*/ k_{off} \approx 0$, or **Equations S25** and **S30**) in order to get $D_f$ for and $D_{eff}$ for PE$_C$P. This unusual recovery behavior is attributed to the LCST behavior of elastin-like polypeptides, and is characterized further in Chapter 3.

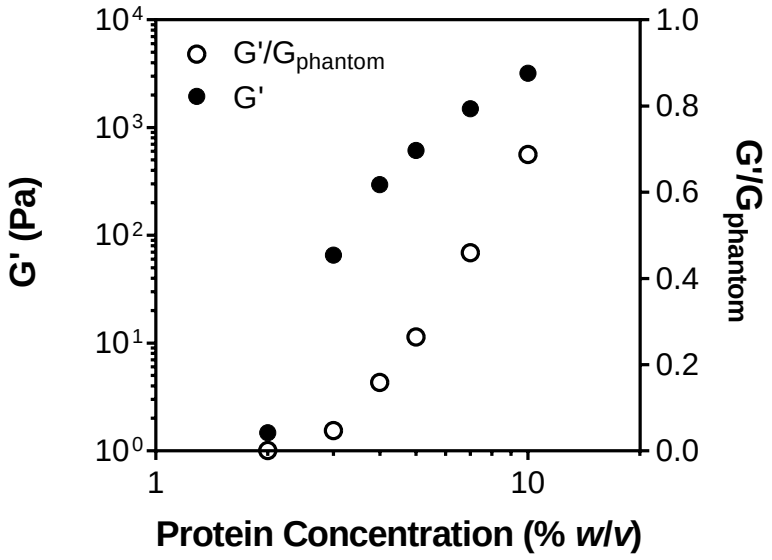


**Supplementary Figure 1.7. Fraction of elastically effective chains estimated from phantom network theory** ($G'/G_{phantom}$ = 0.69 at 10%). Chains in the bound state include both bridges ($B$) and loops ($L$), such that $[b]_{eq} = [B] + [L]$. The simulation described above gives $[B] = 0.70$, similar to the experimental $G'/G_{phantom}$.

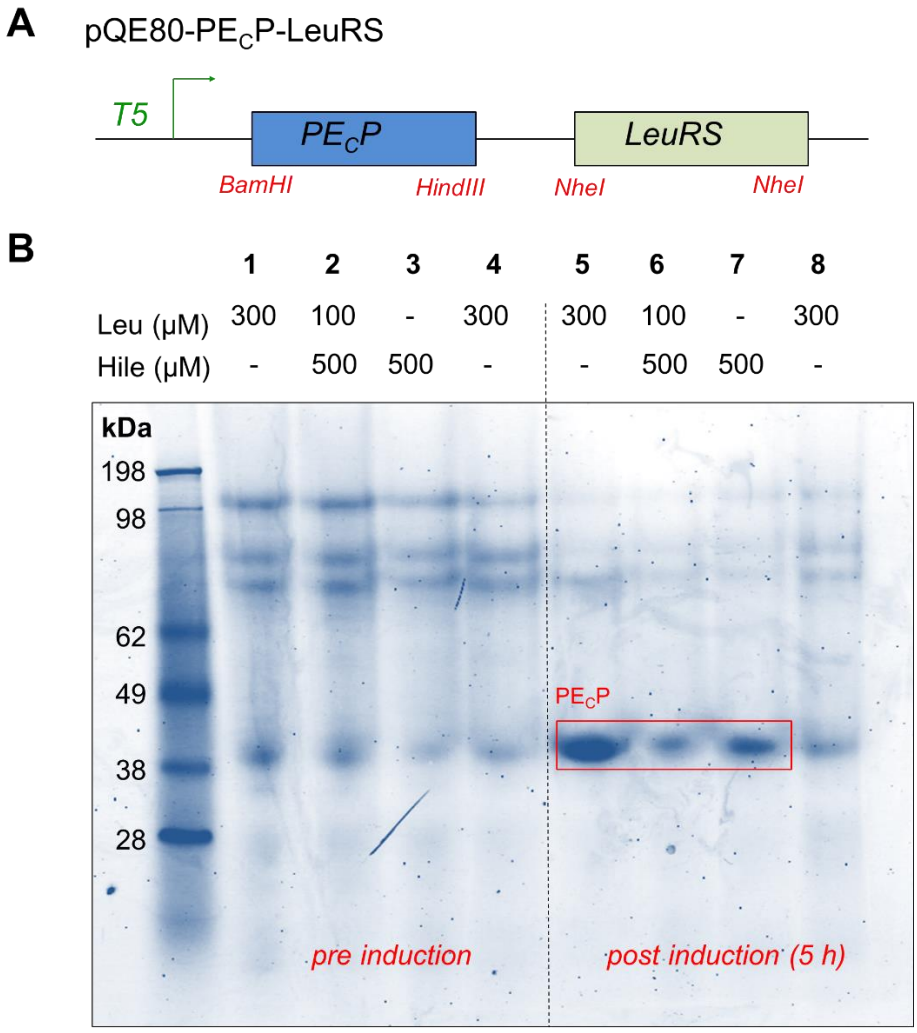


**Supplementary Figure 1.8. Validation of expression cassette for incorporation of Hil into $PE_CP$.** (**A**) To prepare the plasmid pQE80-LeuRS-$PE_CP$, the $PE_CP$ gene was PCR amplified and ligated into pQE-80L-LeuRS between *BamHI* and *HindIII* restriction sites. The gene coding for LeuRS is downstream of $PE_CP$ flanked by *NheI* restriction sites. Its expression is constitutively controlled by its endogenous *E. coli* promoter, whereas $PE_CP$ is under T5 control and is inducible with IPTG. (**B**) 1 L expression cultures of strains carrying pQE80-$PE_CP$-LeuRS in M9 minimal media supplemented with Hil: **1-4**, pre-induction cultures grown in 19AA + Leu; **5-7**, cultures were shifted into M9 media containing 19AA and the indicated amounts of Leu and Hil. Protein expression was induced with 1 mM IPTG and the cultures collected after 5 h; **8**, non-induced control. Strong $PE_CP$ expression can be seen after 5 h.

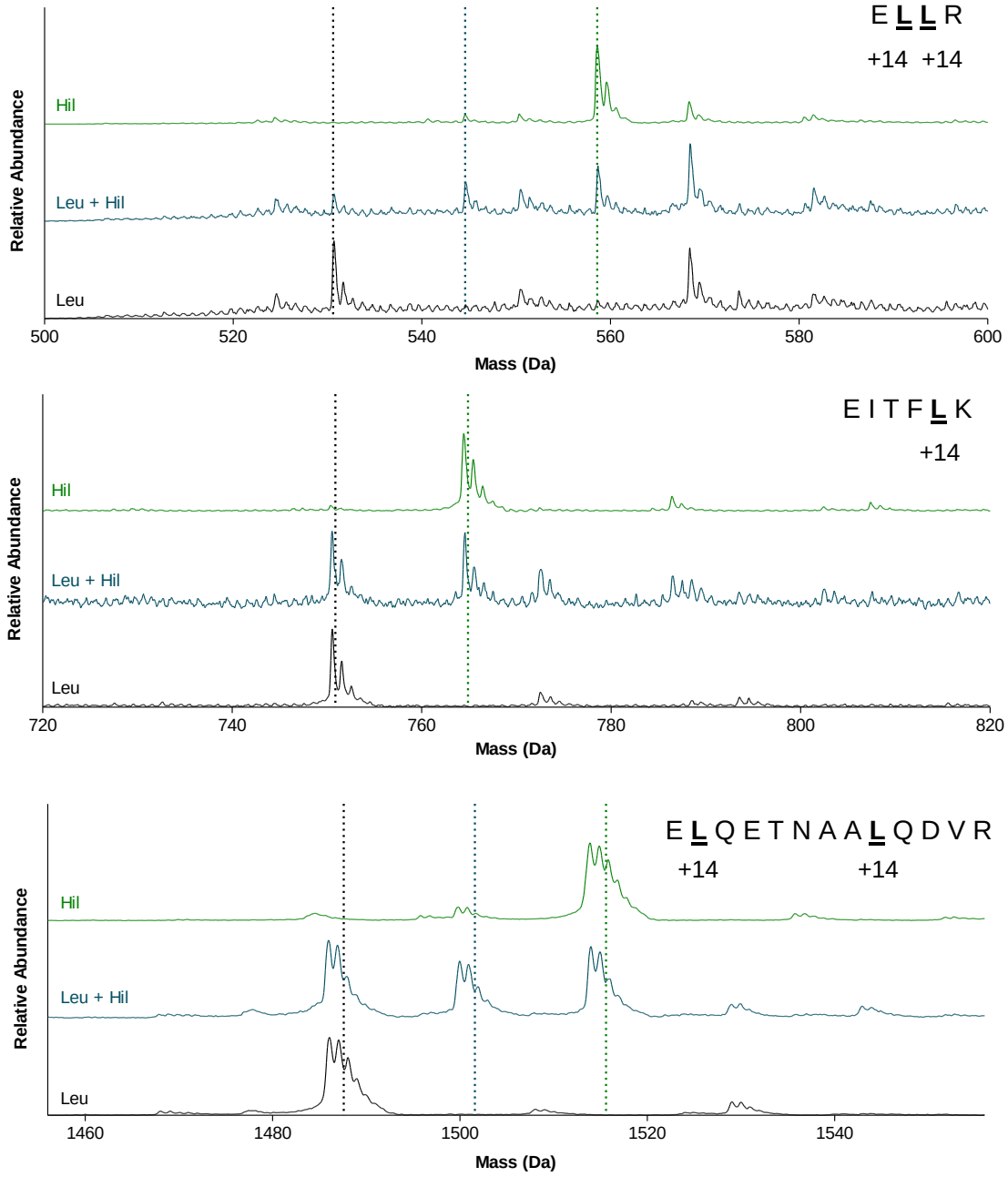


**Supplementary Figure 1.9. MALDI-MS of tryptic peptides containing Hil.** $PE_CP$ was purified from Hil expression lysates and subject to trypsin digestion followed by MALDI-MS. The spectra corresponding to three quantified peptides are presented above. A Hil substitution may be identified by a *m/z* shift of 14 Da arising from the presence of an additional methylene group. The peptides and their expected masses with and without Hil are listed in **Supplementary Table 1.2**. Spectral analysis indicates a maximum Leu → Hil replacement level of **91.8 ± 4.5%**.

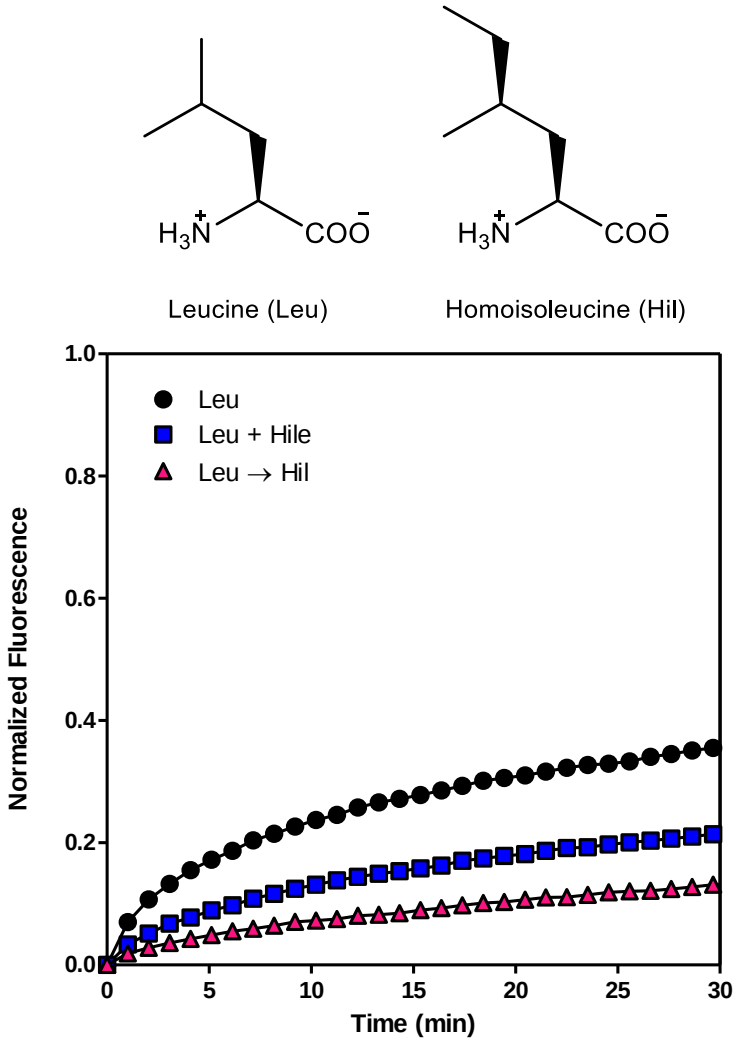


**Supplementary Figure 1.10. Tuning the fluorescence recovery rate with Hil by controlling the level of incorporation of Hil**. Fluorescence recovery curves of a 10% PEP gel labeled with fluorescent $PE_CP$-Hil probes at a mass ratio of 1:5 $PE_CP$ to PEP (i.e. 20% of the network consists of fluorescent probe). The blue curve (Leu + Hil) shows the recovery curve for 53% Hil substitution, and the magenta curve (Leu → Hil) shows the recovery curve for 92% substitution (see **Supplementary Table 1.2** for exact incorporation levels). The degree of substitution provides a means of tuning the fluorescence recovery rate.

## 1.8 References


1. S. Banta, I. R. Wheeldon, M. Blenner, Protein Engineering in the Development of Functional Hydrogels. *Annu Rev Biomed Eng* **12**, 167-186 (2010).

2. W. A. Petka, J. L. Harden, K. P. McGrath, D. Wirtz, D. A. Tirrell, Reversible hydrogels from self-assembling artificial proteins. *Science* **281**, 389-392 (1998).

3. S. Creutz, J. van Stam, F. C. De Schryver, R. Jerome, Dynamics of poly((dimethylamino)alkyl methacrylate-block-sodium methacrylate) micelles. Influence of hydrophobicity and molecular architecture on the exchange rate of copolymer molecules. *Macromolecules* **31**, 681-689 (1998).

4. Z. L. Li, E. E. Dormidontova, Equilibrium chain exchange kinetics in block copolymer micelle solutions by dissipative particle dynamics simulations. *Soft Matter* **7**, 4179-4188 (2011).

5. T. Annable, R. Buscall, R. Ettelaie, D. Whittlestone, The Rheology of Solutions of Associating Polymers - Comparison of Experimental Behavior with Transient Network Theory. *J Rheol* **37**, 695-726 (1993).

6. T. van der Heijden *et al.*, Homologous recombination in real time: DNA strand exchange by RecA. *Mol Cell* **30**, 530-538 (2008).

7. J. T. Holthausen, C. Wyman, R. Kanaar, Regulation of DNA strand exchange in homologous recombination. *DNA Repair* **9**, 1264-1272 (2010).

8. W. Shen, K. C. Zhang, J. A. Kornfield, D. A. Tirrell, Tuning the erosion rate of artificial protein hydrogels through control of network topology. *Nat. Mater.* **5**, 153-158 (2006).

9. W. Shen, J. A. Kornfield, D. A. Tirrell, Dynamic properties of artificial protein hydrogels assembled through aggregation of leucine zipper peptide domains. *Macromolecules* **40**, 689-692 (2007).

10. E. K. O'Shea, R. Rutkowski, W. F. Stafford, P. S. Kim, Preferential Heterodimer Formation by Isolated Leucine Zippers from Fos and Jun. *Science* **245**, 646-648 (1989).

11. E. K. O'Shea, R. Rutkowski, P. S. Kim, Evidence That the Leucine Zipper Is a Coiled Coil. *Science* **243**, 538-542 (1989).

12. W. H. Landschulz, P. F. Johnson, S. L. Mcknight, The Leucine Zipper - a Hypothetical Structure Common to a New Class of DNA-Binding Proteins. *Science* **240**, 1759-1764 (1988).

13. B. D. Olsen, J. A. Kornfield, D. A. Tirrell, Yielding Behavior in Injectable Hydrogels from Telechelic Proteins. *Macromolecules* **43**, 9094-9099 (2010).

14. S. J. Ryan, A. J. Kennan, Variable stability heterodimeric coiled-coils from manipulation of electrostatic interface residue chain length. *J. Am. Chem. Soc.* **129**, 10255-10260 (2007).

15. J. D. Steinkruger, D. N. Woolfson, S. H. Gellman, Side-Chain Pairing Preferences in the Parallel Coiled-Coil Dimer Motif: Insight on Ion Pairing between Core and Flanking Sites. *J. Am. Chem. Soc.* **132**, 7586-7588 (2010).

16. H. Wendt, C. Berger, A. Baici, R. M. Thomas, H. R. Bosshard, Kinetics of Folding of Leucine-Zipper Domains. *Biochemistry* **34**, 4097-4107 (1995).

17. D. L. Daugherty, S. H. Gellman, A fluorescence assay for leucine zipper dimerization: Avoiding unintended consequences of fluorophore attachment. *J. Am. Chem. Soc.* **121**, 4325-4333 (1999).

18. B. L. Sprague, R. L. Pego, D. A. Stavreva, J. G. McNally, Analysis of binding reactions by fluorescence recovery after photobleaching. *Biophys J* **86**, 3473-3495 (2004).

19. B. M. Mayr, E. Guzman, M. Montminy, Glutamine rich and basic region/leucine zipper (bZIP) domains stabilize cAMP-response element-binding protein (CREB) binding to chromatin. *J Biol Chem* **280**, 15103-15110 (2005).

20. J. G. McNally, Quantitative FRAP in analysis of molecular binding dynamics in vivo. *Method Cell Biol* **85**, 329-351 (2008).

21. Y. A. Li *et al.*, Mobility of lysozyme inside oxidized starch polymer microgels. *Soft Matter* **7**, 1926-1935 (2011).

22. S. C. DeSmedt *et al.*, Diffusion of macromolecules in dextran methacrylate solutions and gels as studied by confocal scanning laser microscopy. *Macromolecules* **30**, 4863-4870 (1997).

23. M. C. Branco, D. J. Pochan, N. J. Wagner, J. P. Schneider, Macromolecular diffusion and release from self-assembled beta-hairpin peptide hydrogels. *Biomaterials* **30**, 1339-1347 (2009).

24. F. Herbst, S. Seiffert, W. H. Binder, Dynamic supramolecular poly(isobutylene)s for self-healing materials. *Polym Chem* **3**, 3084-3092 (2012).

25. P. Gribbon, T. E. Hardingham, Macromolecular diffusion of biological polymers measured by confocal fluorescence recovery after photobleaching. *Biophys J* **75**, 1032-1039 (1998).

26. P. Gribbon, B. C. Heng, T. E. Hardingham, The molecular basis of the solution properties of hyaluronan investigated by confocal fluorescence recovery after photobleaching. *Biophys J* **77**, 2210-2216 (1999).

27. V. N. Malashkevich, R. A. Kammerer, V. P. Efimov, T. Schulthess, J. Engel, The crystal structure of a five-stranded coiled coil in COMP: A prototype ion channel? *Science* **274**, 761-765 (1996).

28. P. A. Perry, M. A. Fitzgerald, R. G. Gilbert, Fluorescence recovery after photobleaching as a probe of diffusion in starch systems. *Biomacromolecules* **7**, 521-530 (2006).

29. S. Tang, M. J. Glassman, S. Li, S. Socrate, B. D. Olsen, Oxidatively Responsive Chain Extension to Entangle Engineered Protein Hydrogels. *Macromolecules* **47**, 791-799 (2014).

30. D. M. Soumpasis, Theoretical-Analysis of Fluorescence Photobleaching Recovery Experiments. *Biophys J* **41**, 95-97 (1983).

31. K. J. Hollenbeck, 1998. INVLAP.M: A MATLAB function for numerical inversion of Laplace transforms by the de Hoog algorithm. http://www.mathworks.com/matlabcentral/answers/uploaded_files/1034/invlap.m.

32. W. B. Zhang, F. Sun, D. A. Tirrell, F. H. Arnold, Controlling Macromolecular Topology with Genetically Encoded SpyTag-SpyCatcher Chemistry. *J. Am. Chem. Soc.* **135**, 13988-13997 (2013).

33. B. Zakeri *et al.*, Peptide tag forming a rapid covalent bond to a protein, through engineering a bacterial adhesin. *Proc Natl Acad Sci USA* **109**, E690-E697 (2012).

34. G. M. Cruise, D. S. Scharp, J. A. Hubbell, Characterization of permeability and network structure of interfacially photopolymerized poly(ethylene glycol) diacrylate hydrogels. *Biomaterials* **19**, 1287-1294 (1998).

35. L. M. Weber, C. G. Lopez, K. S. Anseth, Effects of PEG hydrogel crosslinking density on protein diffusion and encapsulated islet survival and function. *J Biomed Mater Res A* **90**, 720-729 (2009).

36. K. Engberg, C. W. Frank, Protein diffusion in photopolymerized poly(ethylene glycol) hydrogel networks. *Biomed Mater* **6**, 055006 (2011).

37. J. A. Zitzewitz, O. Bilsel, J. B. Luo, B. E. Jones, C. R. Matthews, Probing the Folding Mechanism of a Leucine-Zipper Peptide by Stopped-Flow Circular-Dichroism Spectroscopy. *Biochemistry* **34**, 12812-12819 (1995).

38. L. R. Patel, T. Curran, T. K. Kerppola, Energy-Transfer Analysis of Fos-Jun Dimerization and DNA-Binding. *Proc Natl Acad Sci USA* **91**, 7360-7364 (1994).

39. S. Ozeki, T. Kato, M. E. Holtzer, A. Holtzer, The Kinetics of Chain Exchange in 2-Chain Coiled Coils - Alpha-Alpha-Tropomyosin and Beta-Beta-Tropomyosin. *Biopolymers* **31**, 957-966 (1991).

40. S. Dalal, D. Canet, S. E. Kaiser, C. M. Dobson, L. Regan, Conservation of mechanism, variation of rate: folding kinetics of three homologous four-helix bundle proteins. *Protein Eng Des Sel* **21**, 197-206 (2008).

41. S. Y. Park, C. M. Quezada, A. M. Bilwes, B. R. Crane, Subunit exchange by CheA histidine kinases from the mesophile Escherichia coli and the thermophile Thermotoga maritima. *Biochemistry* **43**, 2228-2240 (2004).

42. H. Wendt, A. Baici, H. R. Bosshard, Mechanism of Assembly of a Leucine-Zipper Domain. *J. Am. Chem. Soc.* **116**, 6973-6974 (1994).

43. S. K. Gunasekar *et al.*, N-Terminal Aliphatic Residues Dictate the Structure, Stability, Assembly, and Small Molecule Binding of the Coiled-Coil Region of Cartilage Oligomeric Matrix Protein. *Biochemistry* **48**, 8559-8567 (2009).

44. K. Beck, J. E. Gambee, C. A. Bohan, H. P. Bachinger, The C-terminal domain of cartilage matrix protein assembles into a triple-stranded alpha-helical coiled-coil structure. *J Mol Biol* **256**, 909-923 (1996).

45. K. Kremer, G. S. Grest, Dynamics of entangled linear polymer melts: A molecular-dynamics simulation. *J Chem Phys* **92**, 5057-5086 (1990).

46. W. Shen, J. A. Kornfield, D. A. Tirrell, Structure and mechanical properties of artificial protein hydrogels assembled through aggregation of leucine zipper peptide domains. *Soft Matter* **3**, 99-107 (2007).

47. S. C. Tang, M. Z. Wang, B. D. Olsen, Anomalous Self-Diffusion and Sticky Rouse Dynamics in Associative Protein Hydrogels. *J. Am. Chem. Soc.* **137**, 3946-3957 (2015).

48. P. B. Harbury, T. Zhang, P. S. Kim, T. Alber, A Switch between 2-Stranded, 3-Stranded and 4-Stranded Coiled Coils in Gcn4 Leucine-Zipper Mutants. *Science* **262**, 1401-1407 (1993).

49. J. A. Van Deventer, J. D. Fisk, D. A. Tirrell, Homoisoleucine: A Translationally Active Leucine Surrogate of Expanded Hydrophobic Surface Area. *ChemBioChem* **12**, 700-702 (2011).

50. L. J. Dooling, M. E. Buck, W. B. Zhang, D. A. Tirrell, Programming Molecular Association and Viscoelastic Behavior in Protein Networks. *Adv Mater* **28**, 4651-4657 (2016).

51. J. Braga, J. G. McNally, M. Carmo-Fonseca, A reaction-diffusion model to study RNA motion by quantitative fluorescence recovery after photobleaching. *Biophys J* **92**, 2694-2703 (2007).

*Chapter 2*

# BINDING ASYMMETRY IN TELECHELIC POLYMER NETWORKS

## 2.1 Abstract

Networks assembled by the reversible self-association of telechelic polymers are a common class of soft materials. Here we show that, within any such network, the sequential binding of identical chain ends to the network is inherently asymmetric: the first association is always stronger than the second. This binding asymmetry primarily arises from a strong entropic penalty for chain entry into the fully bound state due to local network structure. We derive a simple equation predicting the degree of binding asymmetry as a function of network geometry from equilibrium statistical mechanics. A large set of self-diffusivity measurements on a series of model telechelic polymers finds good agreement with this new theory. Generalized binding asymmetry for chains with many associative domains also holds.

## 2.2 Introduction

Entropic constraints underlie the structure and dynamics of macromolecular systems. For example, decreased entropy associated with chain stretching is the basis for the elasticity of polymer networks (*1*). Negative entropies of mixing can promote phase separation of polymer solutions at elevated temperatures (*2, 3*). Entropy also regulates many aspects of protein function, including allostery, ligand recognition, and catalytic activity (*4-9*). Here we describe a new binding phenomenon in reversible polymer networks that is under entropic control.

Reversible polymer networks are a well-studied class of materials, and consist of polymers crosslinked through non-covalent or physical means (e.g., by hydrogen bonding or chain entanglement) (*10-13*). Telechelic polymers can spontaneously assemble such networks via reversible self-association of their reactive end-groups (*14-21*). The end-groups cluster into discrete junctions that act as transient interchain crosslinks. Stress relaxation within the resulting network structure is mediated by chain disengagement from the junctions. Importantly, the same event can also permit diffusion of disengaged chains throughout the network (*21*). Relating the bulk material properties of reversible networks to the single chain picture has been the goal of several important theoretical treatments (*22-24*).

Towards the same goal, we model telechelic networks as an ensemble of chains partitioned into three sequential states, depicted schematically in **Figure 2.1A**. In the free state *f,* neither chain end is bound to the network. By reversible association with the network, the chain may transition into either the dangle state *d* (one end bound) or the bound state *b* (both ends bound). Two different topologies are possible in the bound state: bridges (*B*) and loops (*L*). Conversion among the three states is controlled by the equilibrium constants $K_1 = [d]/[f]$ and $K_2 = [b]/[d]$. Since $[b] = [B] + [L]$ we may also write $K_2$ as the sum of bridges and loops, i.e. $K_2 = [B]/[d] + [L]/[d] = K_B + K_L$. Given that the two ends of a telechelic polymer are structurally identical, one might naively expect symmetry between these two constants, i.e. $K_1 = K_2$. We will now demonstrate both theoretically and experimentally that this is essentially never true. Binding asymmetry, with $K_1 > K_2$, will

always arise in this simple system due to purely entropic considerations, regardless of the binding energy or the detailed crosslinking mechanism.

## 2.3 Theory

### 2.3.1 Statistical mechanics of telechelic chain binding

Consider a single telechelic chain undergoing reversible network association (**Figure 2.1A**). The ideal chemical potential for the chain in the free state (neglecting interchain interactions) may be taken as $\beta\mu_f = \ln(n_c[f]\upsilon_{ref}) - \ln(G_f)$, where $\beta = 1/k_BT$, $n_c$ denotes the number density of chains, and $\upsilon_{ref}$ is a reference volume. The conformational entropy of the free chain is contained within $G_f = G_f(\mathbf{R}; N, b)$. We treat the unbound chain ends as distinguishable such that $G_f = \int p(\mathbf{R}; N, b) d\mathbf{R}$, where $p(\mathbf{R}; N, b)$ is the vector end-to-end distance probability density function.

Upon binding once (transition from free to dangle), the chain energy changes by an amount $\Delta E_B$, and the chain also becomes restricted to a small fraction of the total system volume $\phi_j \equiv \upsilon_j n_j$, where $\upsilon_j$ is the local volume accessible to a dangling chain and $n_j$ is the junction number density. Although translational entropy is lost upon tethering one chain end, we assume no additional loss of conformational freedom, since the untethered end is still free to explore space around the junction itself, the size of which is relatively small. These considerations provide $G_d \approx 2G_f$, where the factor of 2 arises because a dangling chain has two ends available for binding the network. The chemical potential of a dangling

chain is then $\beta\mu_d = \ln(n_c[d]\upsilon_{ref} / \phi_j) - \ln(2G_f) + \beta\Delta E_B$, and from the equilibrium condition ($\mu_f = \mu_d$) we obtain $K_1 = 2\phi_j \exp[-\beta\Delta E_B]$.

The chain faces a new challenge during the second binding event (transition from dangle to bound). In order to adopt the bridge topology *B*, the second chain end must locate a new junction within a restricted volume fraction $\phi_j(\mathbf{R}; R_{mesh})$ some distance $\mathbf{R}$ away from the first chain end. This volume necessarily depends on the local network structure, with $\phi_j(\mathbf{R}) = \phi_j g(\mathbf{R})$, where $g(\mathbf{R})$ is the pairwise junction density distribution function. If the preferred size of the free or dangling chain is small relative to $R_{mesh}$, the characteristic mesh size (junction spacing) of the network, significant conformational entropy may be lost during bridge formation. The chain may prefer to adopt the loop topology *L* if the junction spacing is sufficiently wide.

To account for these possibilities, we treat the chemical potential of a bound chain as a sum of bridges and loops, with the bridge configurational integral weighted by the local junction density. We define $\phi_j G_b \equiv \phi_j G_B + G_L$, where $\phi_j G_B = \phi_j \int p(\mathbf{R}) g(\mathbf{R}) d\mathbf{R}$ is the conformational entropy of bridged chains. $G_L$ for loops takes the same functional form as $G_f$ and $G_d$, but we restrict the bounds of the conformational integral to a small distance *l* on the order of the junction size (end-to-end distance of looped chains), rather than the junction spacing. The bound chain chemical potential is then $\beta\mu_b = \ln(n_c[b]\upsilon_{ref} / \phi_j^2) - \ln(G_b) + 2\beta\Delta E_B$, and we obtain $K_2$ from the equilibrium condition ($\mu_d = \mu_b$) as $K_2 = \exp[-\beta\Delta E_B](\phi_j G_B + G_L) / 2G_f$.

This analysis results in the following expression for the ratio of $K_1$ to $K_2$ for a telechelic polymer:

$$\frac{K_1}{K_2} = \frac{4G_f}{G_B + G_L/\phi_j} \qquad \textbf{(Eq. 1)}$$

The ratio is independent of the binding energy. If we neglect loops entirely and consider only bridges ($G_L = 0$), the ratio is simply:

$$\frac{K_1}{K_2} = \frac{4G_f}{G_B} = \frac{4\int p(\mathbf{R})d\mathbf{R}}{\int p(\mathbf{R})g(\mathbf{R})d\mathbf{R}} = \frac{K_1}{K_B} \qquad \textbf{(Eq. 2)}$$

**Eq. 2** distills our key prediction for the reversible binding of telechelic polymers: $K_1$ and $K_2$ will be inequivalent in any network containing a significant fraction of bridges. More specifically, apart from a complete absence of network structure (i.e., junctions are randomly distributed in space such that $g(\mathbf{R}) = 1$), we will always have $K_1 \geq 4K_2$. This asymmetry arises as a natural consequence of network formation, which can reduce the set of conformations available to bridged chains due to the local depletion of junctions on length scales relevant to the free and dangling chains. Moreover, in addition to this structural asymmetry, the first association is inherently four times stronger than the second, since the dangling state always has twice as many ways to bind the network as either the free or the bound states.

We can estimate the strength of these entropic effects directly from **Eq. 2**. Assume "probe" chains with $N = 100$ monomers each of unit length $b = 1$ are partitioned in a "normal

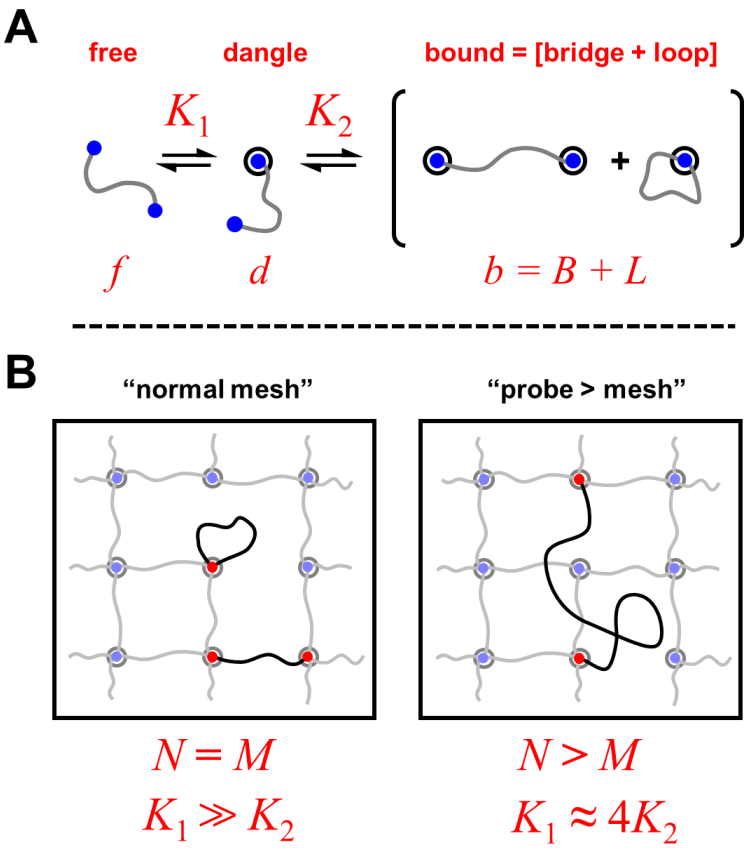


**Figure 2.1. Schematic representation of single chain partitioning in a reversible telechelic network**. (**A**) The chains are partitioned among three sequential states: free (*f*), dangle (*d*), and bound (*b*). The bound state consists of bridges (*B*) and loops (*L*). (**B**) Predicted dependence of binding asymmetry ( $K_1 / K_2$ ) on the mesh size (*M*) and probe size (*N*). Strong asymmetry is expected for the size-matched "normal mesh". Reduced asymmetry is expected for the case where the probe is much larger than the mesh.

mesh" made from chains having the same size $M = 100$ (**Figure 2.1B**). For simplicity, we take $p(\mathbf{R}; N, b) = (3/2\pi Nb^2)^{3/2} \exp(-3\mathbf{R}^2 / 2Nb^2)$ for a Gaussian chain (*25*) and model $g(\mathbf{R}; R_{mesh})$ as a step function activated at a characteristic mesh size $R_{mesh} = 10$. The

characteristic dimensions of the probe are $R_{probe} = bN^{1/2}$, such that $r \equiv R_{probe} / R_{mesh} = 1$. Integrating over the probe chain from $R = 0$ to $R_{max} = Nb$ gives $K_1 / K_2 = 10.21$. Increasing the size of the probe while keeping the network dimensions fixed (**Figure 2.1B**, "probe > mesh") should reduce the degree of asymmetry, since the test chain is less conformationally constrained upon entering the bridge state. Indeed, using $N = 500$ in the above calculation provides $K_1 / K_2 = 4.46$. For an infinitely long probe in a finite mesh, **Eq. 2** predicts that the binding asymmetry arising from network structure will disappear completely ($K_1 / K_2 = 4$). In this case the untethered chain end behaves like a free chain end: it has a global "view" of the network (it can access all available sites) such that bridge formation is not constrained by the other end. In any real network, the above effects will depend on concentration through loops, which we propose to capture with **Eq. 1**.

### 2.3.2 Generalization to chains with multiple stickers

The above, intuitive derivation of binding constants for telechelic chains may be generalized for chains with multiple associative domains ("stickers") along the backbone using a more formal approach. In general, for a multisticker probe with *S* such stickers, one can define an equilibrium constant $K_i$ as the ratio of the number of chains with $i$ to $i-1$ bound chains. One then readily finds

$$K_i = \frac{Z_i}{Z_{i-1}} \exp(-\beta \Delta E_B) \qquad \textbf{(Eq. 3)}$$

where $Z_i$ is the sum of all possible chain configurations with *i* bound stickers, subject to the constraint of chain connectivity. For a chain with *S* total stickers, the number of ways

$N_b$ in which $i \leq S$ such stickers may become bound is simply the binomial coefficient $N_b = C(S,i)$. We can then express $Z_i = \sum_{k=1}^{N_b} Q_k$, where $Q_k$ is the sum of all configurations available to a chain in the $k^{th}$ bound state (**Supplementary Figure 2.1**). The chain can be thought to consist of $S - 1$ flexible "blocks" between each sticker. The total number of configurations available to the whole chain in the $k^{th}$ bound state can be decomposed into the product of the configurations available to each $S - 1$ block, such that $Q_k = \prod_{j=1}^{S-1} G_{k,j}$. The central task is then to compute the number of configurations available to each block for a given bound state of the chain. We derive the exact results for the cases of $S = 3$ and $S = 5$ in the **Supporting Information** (**Supplementary Table 2.1**). Our key prediction for multisticker chains is that $K_i \ll K_{i-1}$ for all sequential associations.

## 2.4 Results and Discussion

### 2.4.1 Network design and characterization

We designed a series of model, reversible telechelic networks to test these predictions. Artificial proteins are well suited to exploring the physical properties of reversible networks: they are structurally well-defined, completely monodisperse, and are easily modified (e.g. chain extended) by manipulating their DNA coding sequences. We cloned and recombinantly expressed a large family of P($E_n$P)$_m$-type protein polymers (**Supplementary Figure 2.2**), where P is an associative domain that forms pentameric coiled-coils (network junctions), and $E_n$ is a flexible elastin-like linker (**Supplementary Tables 2.2** and **2.3**). When swollen in aqueous buffer, P$E_n$P proteins formed completely transparent hydrogels with classical Maxwell-type rheological signatures (**Supplementary**

**Figures 2.3** and **2.4**). We could easily vary the mesh size and terminal modulus of each gel by changing the number of repeats of the elastin midblock ($n$ = 3 – 24), without perturbing the network relaxation rate (**Supplementary Figure 2.5** and **Supplementary Table 2.4**). The terminal network moduli of each "$n$-mesh" approximated the molecular weight dependence expected from rubber elasticity theory ($G'_\infty \sim M^\nu$), with $\nu = -1$ expected for simple affine networks (*25*), and $\nu = -0.9 \pm 0.2$ observed experimentally (**Supplementary Figure 2.5**).

### 2.4.2 Measurement of equilibrium constants

The equilibrium constants $K_1$ and $K_2$ for telechelic polymers were estimated in each $n$-mesh by inferring them from effective diffusivities of size-matched ($N = M$) and mismatched ($N \neq M$) fluorescently-labeled test chains ("$n$-probes", $n$ = 3 – 48) with either zero ($E_n^*$), one ($E_nP^*$), or two ($PE_nP^*$) terminal coils (**Figure 2.2A**). The effective diffusivity $D_S$ of a test chain with $S$ associative domains can be related to each $S^{th}$-order equilibrium constant using:

$$\frac{D_0}{D_S} = 1 + K_1 + K_1K_2 + \cdots + \prod_{i=1}^{S} K_i = 1 + \sum_{j=1}^{S}\left(\prod_{i=1}^{j} K_i\right) \qquad \textbf{(Eq. 4)}$$

where $D_0 = D_f$ is the diffusivity of chains in the free state (*21*). We first measure $D_0$ by monitoring the fluorescence recovery rate of an $E_n^*$ test chain that cannot bind to the network and is therefore locked in the free state. The diffusivity is obtained by fitting the FRAP trace to a renormalized Fickian diffusion model (see **Materials and Methods**) (*21, 26, 27*). Next, $K_1$ is obtained from **Eq. 4** by comparing the mobility $D_1$ of an $E_nP^*$ probe

with $D_0$. This comparison provides a direct estimate for the key exponential factor $K_{1/2} = \phi_j \exp[-\beta \Delta E_B]$, the equilibrium constant for non-telechelic chains with only one sticker. $K_1 = 2K_{1/2}$ for telechelic chains is then easily obtained. Subsequently, $K_2$ for telechelic chains is obtained by comparing the mobility $D_2$ of a PE$_n$P$^*$ probe with $D_0$, and supplying the measured value of $K_1$ into **Eq. 4**. At each step we adjust $D_0$ slightly by the Rouse scaling $D_0 \sim 1/N$, to take into account the added mass of each P domain. An important assumption implicit in the derivation of **Eq. 4** is that network chains have a negligible mobility once bound to the network, such that all chain migration occurs through a "hopping" mechanism. In this mechanism, single chains must completely disengage from the network (enter the free state) in order to travel distances greater than $\sim O(R_{mesh})$ (*21*). We examine this assumption further below.

We acquired a total of 298 FRAP traces on 15 different probes in four different meshes in order to explore a wide range of different $R_{probe} / R_{mesh}$ ratios. Since the bleach spot profile was found to be moderately sensitive to the nature and size of the probe (**Supplementary Figure 2.6**, we acquired an additional 173 control FRAP traces on size-matched E$_n^*$ probes in each of the four meshes (**Supplementary Figure 2.7**). Using a generalized Gaussian bleach spot fit-and-track algorithm, our inferred diffusivities were insensitive to the variance in the bleach spot profile over a wide range of bleach efficiencies. Representative FRAP traces for each of the probes in the 6-mesh network, along with their corresponding Fickian diffusion fits, are presented in **Supplementary Figure 2.8**. Each $D_S$ obtained from

all $15\times4$ combinations of probes and meshes ($n \geq 4$ replicates per combination) is plotted separately in **Supplementary Figure 2.9**.

### 2.4.3 Power-law fits to diffusivity data

Power-law fits to the diffusivity dataset, with $D_S \sim N^{\alpha_s}$, provide molecular weight exponents $\alpha_s$ that permit estimation of $\beta_i$ for each $K_i \sim N^{\beta_i}$ (**Supplementary Figure 2.9** and **Supplementary Table 2.4**). These estimates are qualitatively consistent with **Eq. 1** and **Eq. 2**. In the 6-mesh, for example, $\alpha_0 = -1.5 \pm 0.0$, $\alpha_1 = -0.9 \pm 0.1$, and $\alpha_2 = -1.5 \pm 0.1$ for $D_0$, $D_1$ and $D_2$ respectively (**Figure 2.2B**). A scaling analysis of **Eq. 4** provides $\beta_1 = \alpha_0 - \alpha_1 = -0.6 \pm 0.1$ for $K_1$, and $\beta_2 = \alpha_1 - \alpha_2 = 0.6 \pm 0.1$ for $K_2$. The molecular weight exponent for $K_2$ is positive, implying increasing association strength of the second chain end as the chain becomes longer. $K_1 / K_2 = \beta_1 - \beta_2 = -1.2 \pm 0.1$ is strongly negative, consistent with weakening of the structural asymmetry as the entropic constraint for bridge entry is relaxed. We attribute the negative value of $\beta_1$ to excluded volume effects (e.g., end group association starts to become sterically hindered by the large pervaded volume of the chain itself), which are not captured by our theory. We presume that such effects would hinder both associations equally, in which case they should be approximately absent from the experimental $K_1 / K_2$ ratio.

### 2.4.4 Coarse-graining of *n*-probes as equivalent freely jointed chains

A quantitative comparison of the dataset to **Eq. 1** and **Eq. 2** requires an estimate of $R_{mesh}$ for each mesh, and coarse-grained estimates of $R_{probe}$ for each probe in terms of *b* and *N*,

the Kuhn length and number of monomers for an equivalent freely jointed chain. For this purpose, we select the Flory characteristic ratio $C_\infty = 2.51$, calculated for elastin pentapeptides using conformational energy maps (*28*). Although recent DLS measurements on model elastins in water provide slightly larger ratios (*29, 30*), $C_\infty = 2-3$ is typical for denatured glycine-rich proteins in a $\theta$-solvent (*31, 32*). Moreover, measurements of the second virial coefficient for model elastins suggest a $\theta$-temperature between 40 and 45 °C (*30*), justifying our treatment of the chains as essentially ideal.

For an ideal chain, $R_{probe} = (C_\infty n_p l_p{}^2)^{1/2} = bN^{1/2}$ and $R_{max} = n_p l_p$, where we take $n_p$ to be the number of peptides between each associative domain, and $l_p = 0.38\,\text{nm}$ is the approximate linear $C_\alpha$–$C_\alpha$ distance (*32*). We assign the length of a Kuhn monomer as $b = C_\infty n_p l_p{}^2 / R_{max} = 0.95$ nm (*25*). The equivalent freely jointed chain is then composed of $N = R_{max}{}^2 / C_\infty n_p l_p{}^2$ such monomers, each with an effective molar mass of $M_0 = 198$ Da. Between our smallest (3-probe) and largest (48-probe) chains, $R_{probe}$ = 6.14 – 21.36 nm, and $N$ varies from 41 to 502 respectively. These data are summarized in **Supplementary Table 2.5**. We select $R_{mesh}$ based on the junction number density $n_j$, which provides $R_{mesh} = 12.15 - 17.32$ nm between the 3-mesh and 24-mesh at a fixed mass concentration of $\rho = 100$ g/L. Under these conditions, $r \sim bN^{1/2}M^{-1/3}$ such that binding asymmetry is expected to decrease with increasing molecular weight in size-matched networks (i.e., if $N = M$ and the chain is ideal, $r \sim bM^{1/6}$).

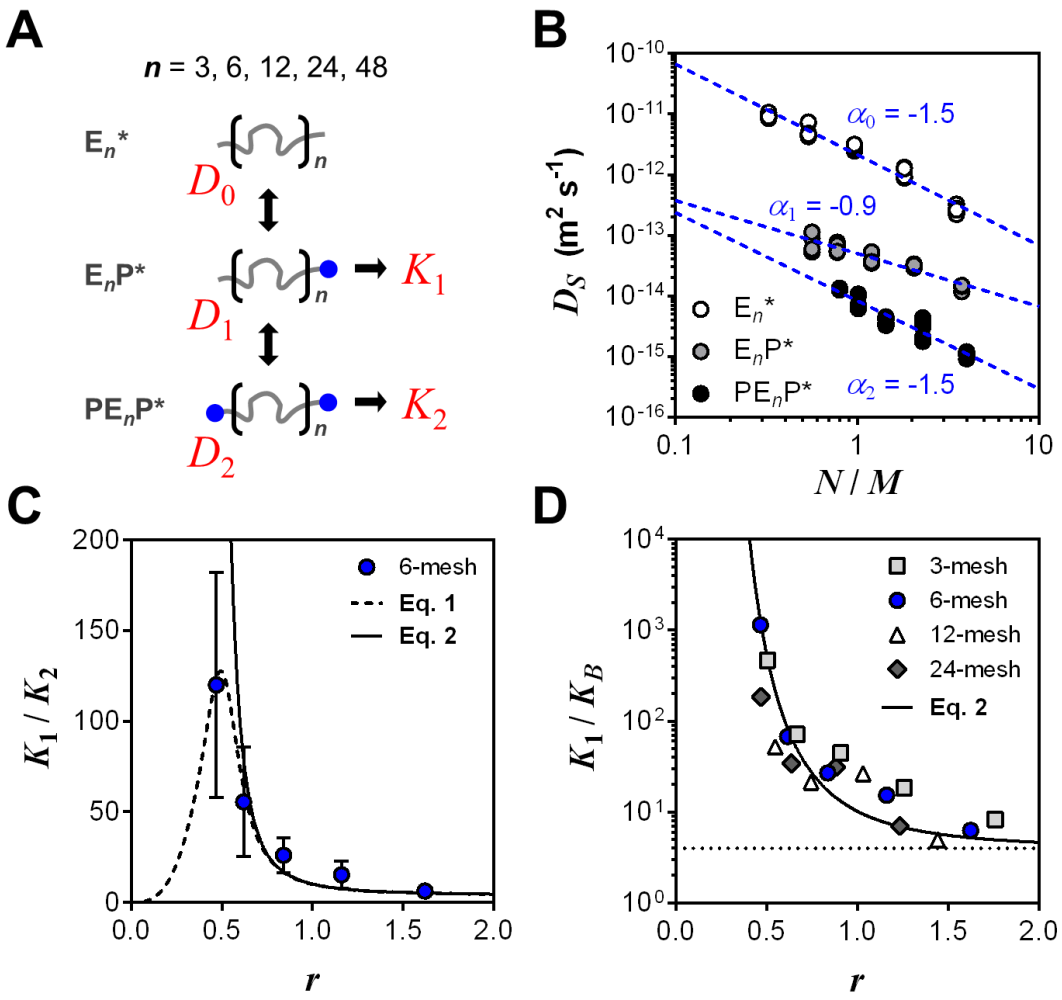


**Figure 2.2. Binding asymmetry in telechelic polymer networks.** (**A**) Elastin-like probes with different lengths and numbers of stickers were placed in size-matched ($N = M$) and mismatched ($N \neq M$) PE$_n$P "$n$-mesh" networks. Equilibrium constants were inferred from diffusivities extracted by FRAP (**Eq. 4**). (**B**) Representative diffusivities in a 6-mesh ($n$ = 80 measurements, ≥ 4 per probe). Molecular weight exponents $\alpha_i$ for each $D_S$ were extracted from power-law fits. (**C**) Experimental $K_1 / K_2$ data (mean ± std. dev.) in the 6-mesh plotted against $r = R_{probe} / R_{mesh} \sim bN^{1/2}M^{-1/3}$. Predictions from **Eq. 1** and **Eq. 2** are shown, with $x_{min}$ = 0.26. (**D**) Loop subtraction permits a simultaneous comparison of the $K_1 / K_B$ data from each mesh ($n$ = 271 total measurements) to **Eq. 2** using $x_{min}$ = 0.24 – 0.43. Error bars are omitted for clarity. The dotted line represents $K_1 / K_B = 4$.

### 2.4.5 Quantitative comparison to theory

A functional analysis of **Eq. 2** reveals that $K_1 / K_2$ is completely specified by the dimensionless probe size *r*, whereas **Eq. 1** contains an effective *N* dependence through $\phi_j = n_j \upsilon_j$ and the looping integral $G_L$. We account for this by modeling the accessible volume of junction-bound chains as $\upsilon_j = 4\pi c^3 / 3$, where *c* is the characteristic dimension of a cluster. Estimates based on the molecular weight of the P domain provide *c* = 1.89 nm (**Supplementary Equations and Derivations**). The *N* dependence may then be captured through *l*, the limits of the looping integral. At fixed $x \equiv l / c$ ratios, the behavior of **Eq. 1** is nearly independent of *c* for $c < R_{mesh}$ due to the approximate cubic form of the volume integral $G_L \sim l^3$, and the fact that $\phi_j \sim c^3$ (**Supplementary Figure 2.10**). We expect $l \sim O(b)$, and indeed, selecting *l* based on rheological data provides *l* = 0.29 – 1.52 nm. In practice we choose $l = l_{min}$ to minimize the residuals between **Eq. 1** and the experimental values in each mesh (**Supplementary Figure 2.11**).

Experimental values of $K_1 / K_2$ in the 6-mesh are plotted against *r* in **Figure 2.2C**, along with the theoretical predictions of **Eq. 1** and **Eq. 2**. The data are in good agreement with the theory: $K_1 / K_2$ rises sharply for *r* < 1, and decays for *r* > 1. The experimental rise in $K_1 / K_2$ appears softened by loop formation at low *r*, an effect that is more significant in the larger meshes (**Supplementary Figure 2.12**). To compare the data in all meshes simultaneously, we subtract out the estimated looping contributions from the experimental data using $K_1 / K_B = [(K_2 / K_1)_{exp} - G_L / 4\phi_j]^{-1}$. Selecting $x_{min}$ = 0.24 – 0.43 to minimize the looping residuals in each mesh leads to a satisfying collapse of the dataset onto **Eq. 2**

(**Figure 2.2D**). $G_L / 4\phi_j > (K_2 / K_1)_{exp}$ for two of the 20 $R_{probe} / R_{mesh}$ ratios (loops are slightly overestimated), which we exclude from the master plot. This can be avoided by choosing a smaller $x_{min}$ = 0.26 for all meshes (fit to the 6-mesh), and a fit of comparable quality is still achieved (**Supplementary Figure 2.13)**. Experimentally, $K_1 / K_B$ varies over a remarkable 200-fold range and exceeds $10^3$ for $r$ = 0.47, the smallest probe in a 6-mesh. This demonstrates the strong entropic penalty paid by chain entry into the bridge state. Moreover, the data appear to asymptote at $K_1 / K_2 = 4$: $K_1 / K_B = 4.94 - 8.27$ is obtained over $r$ = 1.23 – 1.76, the ratios for the largest probes in each mesh.

To directly test the concentration dependence of **Eq. 1**, we acquired an additional 54 FRAP traces in size-matched 6-mesh networks at four additional mass concentrations ($\rho = 50 - 250\,\mathrm{g/L}$), with $\phi_j \sim (c / R_{mesh})^3$ = 0.012 – 0.057. These data are plotted in **Figure 2.3** against **Eq. 1** with $x_{min}$ = 0.37 ± 0.05. Strong formation of loops is evident experimentally at the lowest concentrations, with $K_1 / K_2 \sim \phi_j$ for small $\phi_j$. $K_1 / K_2$ then falls sharply above $\phi_j = 0.035$, consistent with increased bridge formation as the junction spacing becomes smaller. Both of these effects are captured by **Eq. 1**, although the experimental drop in $K_1 / K_2$ is sharper than the theory predicts due to a predicted rise in $K_2$ that is too slow (**Supplementary Figure 2.14**). Excluded volume effects in the real network may be important at these higher concentrations, and cooperative self-assembly of the P domain cannot be excluded. It is interesting to note that **Eq. 1** specifies a region at very low $\phi_j < \phi_j^* = G_L / (4 - G_B)$, for which $K_1 < K_2$ and the binding asymmetry inverts. This region appears physically implausible, since it lies below the mean-field percolation

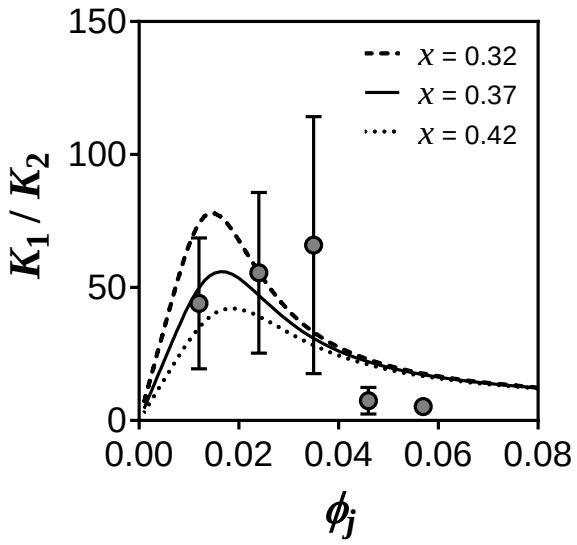


**Figure 2.3. Dependence of $K_1/K_2$ on junction density.** Binding asymmetry is proportional to $\phi_j$ for small $\phi_j \sim R_{mesh}^{-1/3}$, then falls sharply above $\phi_j \sim 0.035$ due to a decrease in interjunction spacing. **Eq. 1** qualitatively captures this behavior, with $x_{min} = 0.37 \pm 0.05$. The data were collected in a 6-mesh network, and predictions from **Eq. 1** were generated using coarse-grained data on 6-mesh probes, with $b$ = 0.95 and $N$ = 72 (**Supplementary Table 2.3**). Error bars depict mean ± std. deviation from $n$ = 76 total measurements, with ≥ 2 measurements per probe per concentration. The mass concentration of each network ranged from 5 – 25% (*w*/*v*), i.e. $\rho$ = 50 – 250 g/L.

threshold for an *f*-functional Bethe-lattice, $p_c = 1/(f-1) = 1/4$ for $f$ = 5. Substituting $\phi_j^*$ into **Eq. S15**, provides the theoretical maximum bridge fraction $[B]^* = G_B/4 \leq p_c$ for all $N$. Hence we always expect $K_1 > K_2$, at least for networks assembled from pentameric crosslinking domains.

Generalization of our theory to chains having $S > 2$ stickers using **Eq. 3** suggests that the entropic penalty for entry into the bridge state becomes compounded with each sequential

association, such that $K_i < K_{i-1}$ for all $i \leq S$ (**Supplementary Table 2.1**). Intuitively, we expect each sequential association to become more costly as the conformational restriction on the whole chain grows. This is expected to greatly increase the fraction of free chains, and thus the likelihood that a chain will migrate by "hopping" (complete site disengagement before rebinding). To test this hypothesis, we synthesized two additional "multisticker" probes, with $S$ = 3 and $S$ = 5, and compared their effective diffusivities, measured in a 6-mesh network, to the exact theoretical predictions for blocks of this size, obtained from **Eq. 3**.

To permit a direct comparison, we define the effective equilibrium constant $K_{eff} = \left[ \sum_{j=1}^{S} \left( \prod_{i=1}^{j} K_i \right) \right]^{1/S}$, such that $D_0 / D_S = 1 + K_{eff}{}^S$ from **Eq. 4**. Moreover, we calculate $D_{hop} = p_f D_0$, where $p_f$ is the fraction of free chains computed from **Eq. 3**. To ensure a correct estimation of the looping fraction, we select $x_{min}$ = 0.37 based on minimization of residuals in the 6-mesh concentration series. We observe striking agreement between the generalized asymmetric binding theory and our measured values of $K_{eff}$ for both $S$ = 3 and $S$ = 5 (**Figure 2.4**). The $D_{hop}$ prediction is essentially exact for $S$ = 3, and $D_{hop} / D_S$ = 0.33 for $S$ = 5, i.e. ca. 33% of these multisticker chains still migrate by hopping, despite the large number of stickers. These predictions hold over several different reasonable estimates of $\phi_j$ and $x$. We note that the measured $D_S$ for $S$ = 5 approaches a theoretical bound mobility $D_b = R_{mesh}{}^2 / 6\tau_b = 1.61 \times 10^{-17}$ m$^2$ s$^{-1}$, where we have assumed that a bound chain can move a distance of order the mesh size within a bound time $\tau_b \sim \omega_c^{-1} \approx 1$ s set by the

relaxation rate of the network (**Supplementary Figure 2.5**). Thus we suspect that, for $S$ = 5, the motion of the remaining chains is slaved to the collective reorganization of the telechelic network itself, in agreement with recent work by Tang et al. (*33*). Notably, ignoring the asymmetry in the binding constants drastically understimates the fraction of free chains. Moreover, a prediction from Baxandall that multisticker self-diffusion should be Rouse-like, with $D_S \sim 1/S$, appears too weak (*23*).

## 2.5 Conclusion

Our results support a new theory of asymmetric binding in reversible networks of telechelic polymers. For telechelic chains, the first association is always greater than the second due to a strong entropic constraint on entry into the bridge state. This constraint arises from a local depletion of network junctions on length scales preferred by the dangling chain. The chain must therefore discard a rich set of conformations in order to effectively bridge network junctions, whereas this constraint is essentially absent during the first association. This leads to $K_1 \gg K_2$ for most networks, and for size-matched networks, the asymmetry is especially strong at low $N$. The effect is compounded for chains with multiple associative domains, leading to $K_{i-1} \gg K_i$ in general, promoting diffusive chain transport that remains strongly influenced by hopping, even for chains with up to five associative domains.

## 2.6 Acknowledgements

The technical assistance of Andres Collazo at the Caltech Beckman Imaging Center during the acquisition of the FRAP data is gratefully acknowledged.

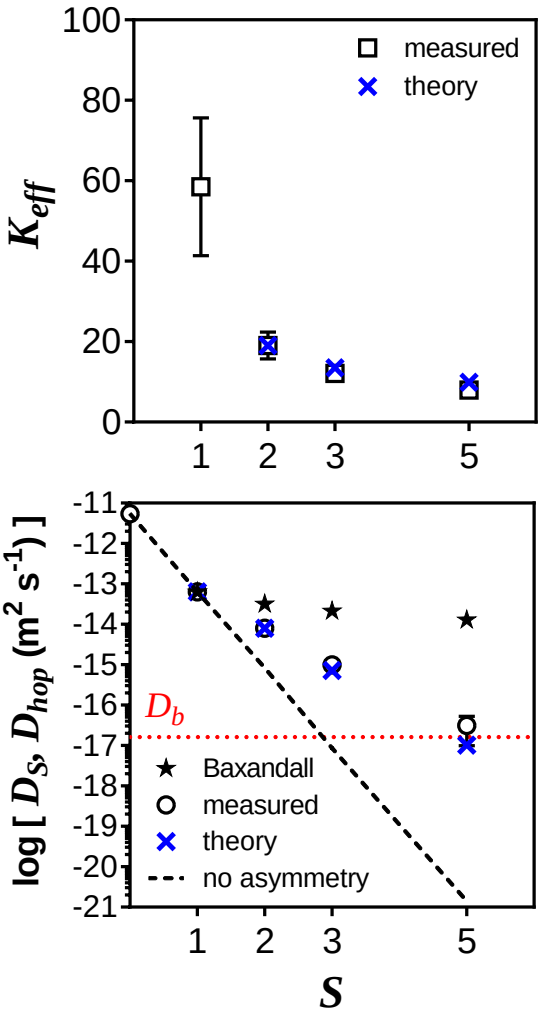


**Figure 2.4. Generalized binding asymmetry for chains with multiple stickers.** Measurements of $K_{eff}$ and $D_S$ are in good agreement with theoretical expectations of $K_{eff}$ and $D_{hop} = p_f D_0$ from **Eq. 3** for $S$ = 2, 3 and 5, generated by supplying the experimental value of $\phi_j \exp(-\beta \Delta E_B)$ measured from the single-sticker $E_nP^*$ probe, and using $x_{min}$ = 0.37 as determined for the 6-mesh concentration series. $D_b = R_{mesh}^2 / 6\tau_b = 1.61 \times 10^{-17}$ $m^2$ $s^{-1}$ is the prediction for the effective mobility of network-bound chains. Results depict mean ± std. deviation from $n \geq 4$ measurements per probe.

## 2.7 Supporting Information

### 2.7.1 Materials and Methods

**Plasmids construction.** Cloning of all $P(E_nP)_m$ constructs was performed on a modified pQE-80L-*ΔXhoI* (≡ pX) vector (Qiagen, USA) with the native *XhoI* site upstream of the MCS inactivated by site-directed mutagenesis. Further mutagenesis was performed on pX to convert the native Asn codon immediately adjacent to the terminal stop codon (just upstream of the *HindIII* site) into a Cys codon (≡ $pX^*$). This enabled facile generation of C-terminal cysteine versions of all proteins by shuttling them from pX to $pX^*$ with a single *BamHI* + *HindIII* double digest. The full amino acid sequences of all artificial proteins is presented in **Supplementary Table 2.2.**

Meshes and test chains of various sizes were prepared from smaller gene fragments by directed recursive ligation (**Supplementary Figure 2.2**). Genes blocks encoding proteins $E_3$ and P were designed and synthesized (Genscript, NJ). Each gene contained two pairs of two sequential restriction sites flanking the 5' (*BamHI-SalI*) and 3' (*XhoI-HindIII*) ends of the gene. These genes were first installed on the vector by *BamHI* + *HindIII* double digestion. Directed recursive ligation was then performed by digesting the vector (containing the gene to be extended) with *XhoI* + *HindIII*, and separately digesting the insert (extension) with *SalI* + *HindIII*. Ligation of the two digestion products between complementary *SalI-XhoI* overhangs (sites then destroyed) and *HindIII* yielded the new, chain extended gene. This cycle could be repeated as many times as desired to produce telechelic proteins of any desired size. Elastin genes were extended by iterative ligation of

the $E_3$ gene in the order: $E_3 > E_6 > E_{12} > E_{24} > E_{48}$. Two different sequences of the $E_3$ gene were used during this process to minimize the repetitiveness of the coding sequence. Each elastin gene was then capped with a P block at one end ($E_nP$) or both ends ($PE_nP$). Plasmids encoding proteins smaller than $PE_6P$ were validated by double-stranded DNA sequencing. Plasmids encoding proteins larger than $PE_6P$ (e.g. $E_{12}^C$) could not be validated this way due to the large size and highly repetitive nature of the insert. Therefore, these larger plasmids were validated by end-sequencing (partial read-through at the 5' and 3' ends to check for proper gene insertion), and the molecular weights of the gene products were then validated by ESI-MS (**Supplementary Table 2.3**).

**Protein expression and purification.** Plasmids coding for each proteins were transformed into BL21 chemically competent *E. coli* (NEB, Δ*fhuA2* resistant to phage T1). Overnight cultures of transformed cells were used to inoculate 1 L flasks containing Terrific Broth (TB) (inoculation ratios were typically 1:20-50) supplemented with 100 mg $ml^{-1}$ ampicillin. Cells were grown to an $OD_{600}$ of 0.7 – 1.0 and then induced with 1 mM isopropyl β-D-1 thiogalactopyranoside (IPTG). After 4-6 h, bacterial cultures were harvested by centrifugation for 6 min at 10,000*g*. Cells were immediately resuspended in 8 M urea, pH 8 supplemented with 100 mM phosphate, 10 mM Tris and 10 mM imidazole). Lysates were taken through two freeze-thaw cycles before being subject to high-power tip sonication (tip diameter ~ 1 cm). For sonication, 50 mL of lysate from a 1 L culture was treated at 50% maximum amplitude for 10 min in 1 sec pulse intervals (5 min total sonication time). Homogenized lysate was clarified by high-speed centrifugation (50,000*g* for 1 h) and then

subjected to standard His-tag purification over Ni-NTA agarose beads (Qiagen, USA) under denaturing conditions.

Prior to elution of the purified protein, the column was buffer-exchanged into 8 M urea supplemented with 100 mM Tris, pH 8, and eluted in this buffer with 250 mM imidazole. This allowed for removal of phosphate, and was crucial for containing soluble, well-folded batches of the smallest mesh protein ($PE_3P$). 50 – 100 mL of eluted protein was dialyzed against 4 L of pre-chilled distilled water at 4 °C. The water was changed repeatedly (5 – 6x) over the course of several days. For all except the largest proteins (see below), yields after lyophilization typically ranged from 80 to 200 mg/L.

The four largest proteins expressed ($E_{48}^C$ , $E_{48}P^C$, $PE_{48}P^C$ and $P(E_6P)_4^C$) were found to be highly susceptible to proteolytic cleavage and fragmentation during the typical denaturing work-up described above. As a result, these four proteins were lysed, extracted, and purified using B-PER Complete (ThermoFisher) supplemented with "cOmplete ULTRA" protease inhibitor tablets (Roche). After extensive column washing with a native high salt buffer (100 mM Tris, 500 mM NaCl, 20 mM imidazole, pH 8), the column was exchanged into 8 M urea and washed with a step-wise pH gradient (8 > 6.3 > 5.9) before being eluted. All wash and elution fractions were analyzed, and those containing pure protein were pooled.

**Fluorescent Labeling of Probes.** The C-terminal cysteine of all test chains was site-specifically labeled with fluorescein-5-maleimide (Life Technologies) to permit diffusion measurements by fluorescence recovery after photobleaching (FRAP). Briefly, all probes ($E_n^C$, $E_nP^C$, $PE_nP^C$ and multiblocks $P(E_6P)_2^C$ and $P(E_6P)_4^C$) were dissolved at 240 $\mu$M in 1

mL of 8 M urea, pH 7.5 – 8, supplemented with 100 mM $NaH_2PO_4$. Tris-(2-Carboxyethyl)phosphine Hydrochloride (TCEP, ThermoFisher Scientific) was added at a 20:1 ratio (TCEP:protein). After 30 min, fluorescein-5-maleimide was added at a 10:1 ratio (dye:protein), and labeling was allowed to proceed at room temperature for 2 h. Remaining thiols were then alkylated for 30 min with iodoacetamide (IAM, 20:1 ratio), and the reaction was quenched with addition of a small amount of 2-mercaptoethanol (Sigma). Tubes were gently rotated throughout the reaction. Using this procedure, the extent of polymer labeling was 0.3 moles dye per mole of protein (estimate based on comparison to dilute solutions of free dye). All fluorescently-labeled –Cys terminated proteins are denoted with a * (**Supplementary Table 2.2** and **Supplementary Figure 2.2**).

After the labeling reaction was quenched, probes were bound to a small volume of NiNTA, washed to remove unreacted dye, and then subject to a rapid on-column refolding protocol. The column was first equilibrated in a buffer containing 20 mM Tris, 100 mM NaCl, pH 7.4, and supplemented with 8 M urea, then rapidly washed in the same buffer but without urea, and eluted under native conditions (20 mM Tris, 100 mM NaCl, 500 mM imidazole). Following overnight dialysis in 100 mM phosphate buffer pH 7.4, aliquots of labeled, refolded probes were flash-frozen in liquid nitrogen and stored at -80 °C until use. Thawed probes were immediately used to prepare gels, and were photobleached within two weeks of the initial thaw.

**Hydrogel Preparation.** Gels were typically prepared at a concentration of 10% (*w*/*v*) (protein volume fraction $\varphi \sim 0.067$) by adding 100 mM phosphate buffer, pH 7.4, directly

to lyophilized protein. The protein was allowed to swell for several hours, and was periodically mixed and centrifuged. Fluorescent gels for FRAP experiments were prepared by swelling protein in phosphate buffer containing the desired fluorescent test chain at a concentration of ~10 μM.

**Rheology.** Oscillatory shear rheometry was performed on 10% (*w*/*v*) PE$_n$P meshes using an ARES-RFS strain-controlled rheometer (TA Instruments) equipped with a cone-and-plate geometry (25 mm diameter, gap width 50 μm). The outer edge of the plate was coated with mineral oil to minimize evaporation, and sample temperature was maintained at 25 °C using a circulating water batch. Strain sweeps at 10 rad $s^{-1}$ identified a linear regime between 0.1 and 10% strain. Frequency sweeps were performed at a fixed strain amplitude of 1% between 0.01 and 100 rad $s^{-1}$. Large-amplitude oscillatory shear (LAOS) experiments were performed at 10 rad $s^{-1}$ between strains of 0.1 and 1000%.

**Fluorescence Recovery After Photobleaching.** A small volume of fluorescent gel (5 – 10 μL) was placed between two glass coverslips separated by a 120 μm spacer (Secure-Seal Spacer, ThermoFisher). Photobleaching was performed on a Zeiss LSM 880 equipped with a 488 nm Ar-Ion laser (25 mW nominal output power) and a standard 25X/0.8NA objective. A bleach spot radius of 10 μm was defined using the Zen Black photobleaching applet, and ~1500 bleach iterations were then applied at maximum laser power and scan rate. Recovery was monitored with a wide pinhole at low laser power.

We observed variance in the effective bleach spot size and bleach depth (extent of photobleaching within a spot) among the various probes (**Supplementary Figure 2.6**).

This variance arose for several reasons: probes without stickers (e.g., the $E_n$-series) diffused very fast during the bleaching period, and had wider and shallower bleach spots as a result. Probes with one or many stickers (e.g., $PE_nP$-series) had tighter and deeper bleaches. Increasing the chain length within a given series could also change the shape of the bleach spot. Furthermore, the output power of the Ar-Ion laser steadily decreased over the experimental period by as much as 20% due to heavy use (hundreds of FRAP experiments conducted over a ~6-mo period), and decreased output power from the laser gave shallower bleaches. To control for these effects, we performed rigorous post-acquisition image analysis for each experiment:

i. The raw image stack (time series data) for each recovery was first imported into MATLAB, and the fluorescence intensity profile across the diameter of the bleach spot from the first post-bleach image was fit to a generalized Gaussian of the form:

$$g(x) \sim e^{-(|x-\mu|/\alpha)^{\beta}} \qquad \textbf{(Eq. S1)}$$

with mean $\mu$ and variance $\alpha^2\Gamma(3/\beta)/\Gamma(1/\beta)$. The variance of the bleach spot profile extracted from this fit was used as the bleach spot radius. Bleach depth (efficiency) was determined by averaging the fluorescence intensity within the area defined by this radius (**Supplementary Figure 2.6**).

ii. After measuring the bleach spot radius (variance), a spot-tracking algorithm was used to follow the center of the recovering bleach spot. The normalized

fluorescence recovery curve (range of [0,1]) was obtained by comparing the average intensity $F(t)$ in this tracked spot to the intensity in a control region of the same image $F_\infty(t)$.

$$f(t) = \frac{F(t)/F_\infty(t)}{F(t_0)/F_\infty(t_0)} \qquad \textbf{(Eq. S2)}$$

Following this normalization, the data were scaled such that $f(t_0) = 0$ using

$$\bar{f}(t) = \frac{f(t) - \min[f(t)]}{1 - \min[f(t)]} \qquad \textbf{(Eq. S3)}$$

iii. Using the MATLAB routine *nlinfit.m*, the normalized, scaled recovery traces were then fit to an effective diffusion equation derived by Soumpasis (*26, 27*):

$$\bar{f}(t) = \exp\left(\frac{-\tau_D}{2t}\right)\left[\mathrm{I}_0\left(\frac{-\tau_D}{2t}\right) + \mathrm{I}_1\left(\frac{-\tau_D}{2t}\right)\right] \qquad \textbf{(Eq. S4)}$$

where $\tau_D = a^2 / D_{eff}$. Here $a$ is the radius of the bleach spot (the variance measured from the generalized Gaussian fit of the bleach spot profile) and $D_{eff} = D_S$ has the definition described in the main text (**Eq. 4**).

To confirm that the above procedure gave estimates for $D_{eff}$ that were not affected by the output laser power, or intrinsically biased by the fast or slow recovery rate of the probe (which could change the bleach efficiency and the shape of the bleach spot), we acquired 173 control FRAP traces across the four different meshes (3-, 6-, 12-, and 24-mesh), using matched ($N$ = $M$) E$_n$-series probes at two labeling concentrations (ca. 1 and 10 μM)

(**Supplementary Figure 2.7**). The bleach efficiency and effective bleach spot size were systematically varied by increasing the duration of the bleach period (# of bleach iterations). The effective mobilities $D_{eff} = D_S$ obtained from this dataset using the analysis described above were independent of the bleach efficiency, bleach spot size, and probe concentration (**Supplementary Figure 2.7**). Specifically, the standard deviation of $D_{eff}$ across the different bleach efficiencies did not exceed 25% of the mean $D_{eff}$ for any of the probe concentrations and mesh sizes examined ( $0.14 < \mu / \sigma < 0.25$ ).

### 2.7.2 Supplementary Equations and Derivations

**Estimation of key *n*-mesh parameters.** The characteristic dimensions of differently sized meshes were estimated from protein concentration, simple geometric arguments, and molecular weight data. First, the number density of junctions $n_j$ (crosslinking sites) was calculated as

$$n_j = \frac{2}{5}\left(\frac{\rho}{M}\right)N_A \qquad \textbf{(Eq. S5)}$$

where $\rho$ is the protein mass concentration in g/L, $M$ is the molecular weight of the mesh, and $N_A$ is Avogadro's number. From **Eq. S5**, the characteristic mesh size $R_{mesh}$ was estimated by approximating the average distance between junctions as two times the radius of a sphere with the volume equal to the mean volume per junction.

$$R_{mesh} = 2 \times \left(\frac{3}{4\pi n_j}\right)^{1/3} \qquad \textbf{(Eq. S6)}$$

Values of $R_{mesh}$ obtained from **Eq. S6** are reported in **Supplementary Table 2.4**. To estimate $\phi_j$, the fractional volume accessible to dangling chains, we use

$$\phi_j = \frac{\bar{\upsilon}_p}{\frac{1000}{\rho_j} + \bar{\upsilon}_p} \approx \bar{\upsilon}_p \left( \frac{\rho_j}{1000} \right) \qquad \textbf{(Eq. S7)}$$

where $\bar{\upsilon}_p = 0.7230$ mL/g is the partial specific volume of the protein estimated from elastin sequence data and the mean volume of each amino acid residue (*34*). Here $\rho_j$ is the junction mass concentration, which is related to the total protein concentration by $M_P / M_{PEP}$, the molecular weight ratio of the P domain to the whole protein.

$$\rho_j = \rho \left( \frac{2M_P}{M_{PEP}} \right) \qquad \textbf{(Eq. S8)}$$

Since $\phi_j = n_j \upsilon_j$ and $\upsilon_j = 4\pi c^3 / 3$, **Eq. S5** and **S7** provide an estimate for $c = 1.89$ nm, the average dimension of a cluster. This is in good agreement with structural data on the P domain, since $c = 2.31$ nm is provided by the X-ray crystal structure of the pentameric assembly (*35*). In order to make quantitative comparisons of experimental data to predictions from **Eq. 1** and **Eq. 2**, we numerically specified $\phi_j = n_j \upsilon_j$ in terms of *c* and the mesh size $R_{mesh}$:

$$\phi_j = \left( \frac{2c}{R_{mesh}} \right)^3 \qquad \textbf{(Eq. S9)}$$

**Generalized binding asymmetry for multisticker probes.** Consider the case of a chain with $S$ = 3 evenly spaced stickers along its backbone, with $j = 2$ blocks of molecular weight $N$ and Kuhn length $b$ (**Supplementary Figure 2.1**). For $i = 0$, there is only $N_b = 1$ state (the free state with all stickers unbound), and $Z_0 = Q_0 = {G_f}^2$, where $G_f$ takes the same form as for telechelics. For $i = 1$ there are $N_b = 3$ possible bound states, and binding restricts the chain to a fraction of the total system volume $\phi_j$. Assuming no loss of conformational entropy during this single sticking event provides $\sum_{k=1}^{3} Q_k = \sum_{k=1}^{3} \phi_j G_{k,1} G_{k,2} = 3\phi_j {G_f}^2$. Thus from **Eq. 3**, $K_1 = 3\phi_j \exp(-\beta \Delta E_B)$ for a 3-sticker chain. Note that this is $3/2$ the value of a 2-sticker (telechelic) chain, which arises as a direct consequence of the extra sticker.

Similar to telechelics, states with $i = 2$ bound blocks must pay the entropic cost associated with simultaneously locating two well-spaced junctions, or else form loops. The entropy for a chain with two adjacent bound stickers and one dangling end (see $k$ = 2,3 in **Supplementary Figure 2.1**) is $Q_2 = Q_3 = {\phi_j}^2 G_f G_b$, where again $\phi_j G_b = \phi_j G_B + G_L$ as for telechelics. For the state with one unbound sticker in the middle ($k$ = 1), the conformations of each block are coupled. We use the self-similarity property of Gaussian chains to write $Q_1 = {\phi_j}^2 G_b(\mathbf{R}; 2N, b) = {\phi_j}^2 G_b(2N)$, i.e., the chain is effectively telechelic with a block length of 2$N$. Summing over all $k$ we obtain $Z_2 = {\phi_j}^2 (2Q_{2,3} + Q_1)$, and together with $Z_1$, that $K_2 = \dfrac{2G_f G_b + G_b(2N)}{3{G_f}^2} \phi_j \exp(-\beta \Delta E_B)$. When all three stickers are bound ($i$ = 3), there is again only one possible state. In this case $Z_3 = {\phi_j}^3 {G_b}^2$, and the equilibrium constant is

$K_3 = \frac{{G_b}^2}{2G_f G_b + G_b(2N)} \phi_j \exp(-\beta \Delta E_B)$. Analogous combinatorial considerations provide each $K_i$ for chains with even more stickers. The results for the case of $S = 5$ are presented in **Supplementary Table 2.1**.

**Evaluation of configurational integrals. Eq. 1** and **Eq. 2** in the main text specify $K_1 / K_2$ in terms of the following configurational integrals:

$$G_f = \int_0^\infty p(\mathbf{R}) d\mathbf{R} = 4\pi \int_0^\infty p(R) R^2 dR = 1 \qquad \textbf{(Eq. S10)}$$

$$G_L = \int_0^l p(\mathbf{R}) d\mathbf{R} = 4\pi \int_0^l p(R) R^2 dR \qquad \textbf{(Eq. S11)}$$

$$G_B = \int_0^\infty p(\mathbf{R}) g(\mathbf{R}) d\mathbf{R} = 4\pi \int_0^\infty p(R) g(R) R^2 dR \qquad \textbf{(Eq. S12)}$$

where $l \sim O(b)$ represents the end-to-end distance of a looped chain, and we approximate $g(R)$ as a Heaviside step function activated at $R = R_{mesh}$. Since $R_{mesh} \sim \phi_j^{-1/3}$, $g(R; R_{mesh})$ has an implicit dependence on $\phi_j$. Evaluation of the above integrals requires a choice of $p(R)$, which we choose to be the Gaussian chain integral:

$$p(R) = (3/2\pi N b^2)^{3/2} \exp(-3R^2 / 2Nb^2) \qquad \textbf{(Eq. S13)}$$

**Selection of limits on the looping integral.** Because **Eq. 1** in our theory predicts the fraction of bridged and looped chains [$B$] and [$L$], it is possible to compare the theoretical fraction of bridged chains to the fraction of elastically effective chains $G'_\infty / G_{phantom}$ estimated from rheology and phantom network theory (**Supplementary Figure 2.11**). For

a given cluster dimension *c*, this constraint fixes the limits of the looping integral *l*. Recall the definitions of each equilibrium constant, and the assumption that $G_d \approx 2G_f$ :

$$K_1 = \frac{[d]}{[f]} = \frac{\phi_j G_d}{G_f} \exp(-\beta \Delta E_B) = 2\phi_j \exp(-\beta \Delta E_B)$$

$$K_L = \frac{[L]}{[d]} = \frac{G_L}{2G_d} \exp(-\beta \Delta E_B) = K_1 G_L / 4\phi_j$$

$$K_B = \frac{[B]}{[d]} = \frac{\phi_j G_B}{2G_d} \exp(-\beta \Delta E_B) = K_1 G_B / 4$$

If we require the normalization $[f]+[d]+[B]+[L]=1$, then $[B] = G'_\infty / G_{phantom}$ is exact and we need only solve for $[B]$ in terms of known equilibrium constants.

$$\frac{[d]}{K_1} + [d] + K_L[d] + [B] = 1$$

$$\left(\frac{1}{K_1} + 1 + K_L\right)[d] + [B] = 1$$

$$\left(\frac{1}{K_1} + 1 + K_L\right)\frac{[B]}{K_B} + [B] = 1$$

$$[B] = \left[1 + \frac{1}{K_B}\left(K_L + 1 + \frac{1}{K_1}\right)\right]^{-1}$$

$$[B] = \left[1 + \frac{1}{G_B}\left(G_L(l)/\phi_j + \frac{4}{K_1} + \frac{4}{K_1{}^2}\right)\right]^{-1} \qquad \textbf{(Eq. S14)}$$

Assuming $K_1 \gg 1$, the above expression simplifies to:

$$[B] = \left[1 + \frac{G_L(l)}{\phi_j G_B}\right]^{-1} = f(l; R_{mesh}, N, b, c) = G'_\infty / G_{phantom} \qquad \textbf{(Eq. S15)}$$

**Eq. S14** or **Eq. S15** may be used to fix $l = l_{calc}$ provided that reasonable estimates of the mesh parameters ($R_{mesh}$, $c$) are known and the polymer is properly coarse-grained as an equivalent, freely-jointed chain ($N$, $b$). Representative plots of $G'_\infty / G_{phantom}$ versus $l$ are shown in **Supplementary Figure 2.11**, and the $x_{calc} = l_{calc} / c$ values obtained using this scheme are presented in **Supplementary Table 2.4**.

An inverse use of this framework is the calculation of the fraction of loops from a measurement of $G'_\infty / G_{phantom} = [B]$. It is easy to show that this provides $[L]$ in a straightforward manner, provided $K_1$ and $l$ are known in advance:

$$[L]\left(\frac{1}{K_L K_1} + \frac{1}{K_L} + 1\right) = 1 - G' / G_{phantom}$$

$$[L] = \frac{1 - G' / G_{phantom}}{\frac{4\phi_j}{K_1^2 G_L(l)} + \frac{4\phi_j}{K_1 G_L(l)} + 1} \qquad \textbf{(Eq. S16)}$$

We obtain $K_1$ from FRAP measurements, and $l = l_{min}$ from minimizing residuals (**Supplementary Figure 2.11**), although in the absence of such information it is also possible to simply take $l \approx b$. Values of $[L]$ in each $n$-mesh obtained using $K_1$ and $l_{min}$ are

also presented in **Supplementary Table 2.11**. Note that **Eq. S15** collapses to the well-known equation $[L] \approx 1 - G'/G_{phantom}$ for very large $K_1$.

### 2.7.3 Supplementary Tables

**Supplementary Table 2.1. Exact equilibrium constants for a multisticker probe with *S* = 5 stickers**. Each $K_i$ is normalized by the factor $\phi_j \exp(-\beta \Delta E_B)$, and the numerical data for each $K_i / K_{i-1}$ were calculated using coarse-grained data on the 6-mesh network, i.e. $b$ = 0.95 nm and $N$ = 72, but with $R_{mesh}$ adjusted to be 14.06 nm such that $K_1 / K_2$ = 55.6 for telechelics is predicted exactly ($x$ = 0.37 was used for the looping integral based on minimization of the residuals in the 6-mesh concentration series). $G_b$ and $G_f$ take the same form as for telechelics, and unless otherwise noted, $G_b = G_b(N)$ where $N$ is the length of an equivalent freely joined chain between each sticker.

| | $K_i / \phi_j \exp(-\beta \Delta E_B)$ | $K_i / K_{i-1}$ |
|---|---|---|
| $i = 1$ | 5 | - |
| $i = 2$ | $\frac{G_b(4N) + 2G_b(3N)G_f + 3G_b(2N)G_f^2 + 4G_bG_f^3}{5G_f^4}$ | 0.091 |
| $i = 3$ | $\frac{3G_b^2G_f^2 + 4G_b(2N)G_bG_f + 2G_b(3N)G_b + G_b(2N)^2}{G_b(4N) + 2G_b(3N)G_f + 3G_b(2N)G_f^2 + 4G_bG_f^3}$ | 0.181 |
| $i = 4$ | $\frac{2G_b^3G_f + 3G_b(2N)G_b^2}{3G_b^2G_f^2 + 4G_b(2N)G_bG_f + 2G_b(3N)G_b + G_b(2N)^2}$ | 0.276 |
| $i = 5$ | $\frac{G_b^5}{2G_b^3G_f + 3G_b(2N)G_b^2}$ | 0.020 |

**Supplementary Table 2.2. Sequences of all probe and mesh proteins prepared by directed recursive ligation**. All mesh proteins were encoded on a pQE-80L-*ΔXhoI* (≡ pX) plasmid backbone, and all –Cys terminated proteins (used to prepare the * fluorescent probes) were encoded on a pQE-80L-*ΔXhoI*-Cys vector (≡ pX*).

| Protein | MW (Da) | Sequence |
|---|---|---|
| **P** |  | APQMLRE LQETNAA LQDVREL LRQQVKE ITFLKNT VMESDAS |
| **$E_n$** |  | $[(VPGAG)_2VPGEG(VPGAG)_2]_n$ |
| **$E_n$* series** | | MRGSH$_6$GSVD-{**insert**}-LEH$_6$KLC |
| $E_3^C$ | 8,936 | **$E_3$** |
| $E_6^C$ | 15,060 | **$E_3$**-LD-**$E_3$** |
| $E_{12}^C$ | 27,308 | [**$E_3$**-LD]$_3$-**$E_3$** |
| $E_{24}^C$ | 51,805 | [**$E_3$**-LD]$_7$-**$E_3$** |
| $E_{48}^C$ | 100,798 | [**$E_3$**-LD]$_{15}$-**$E_3$** |
| **$E_n$P* series** | | MRGSH$_6$GSVD-{**insert**}-(GS)$_6$G-**P**-(GS)$_6$-LEH6KLC |
| $E_3P^C$ | 15,779 | **$E_3$**-LD |
| $E_6P^C$ | 21,903 | [**$E_3$**-LD]$_2$ |
| $E_{12}P^C$ | 34,151 | [**$E_3$**-LD]$_4$ |
| $E_{24}P^C$ | 58,647 | [**$E_3$**-LD]$_8$ |
| $E_{48}P^C$ | 107,640 | [**$E_3$**-LD]$_{16}$ |
| **PE$_n$P* series** | | MRGSH$_6$GSVD(GS)$_6$G-**P**-(GS)$_6$LD-{**insert**}-(GS)$_6$G-**P**-(GS)$_6$-LEH6KLC |
| $PE_3P^C$ | 22,621 | **$E_3$**-LD |
| $PE_6P^C$ | 28,745 | [**$E_3$**-LD]$_2$ |
| $PE_{12}P^C$ | 40,994 | [**$E_3$**-LD]$_4$ |
| $PE_{24}P^C$ | 65,490 | [**$E_3$**-LD]$_8$ |
| $PE_{48}P^C$ | 114,483 | [**$E_3$**-LD]$_{16}$ |
| **mesh series** | | MRGSH$_6$GSVD(GS)$_6$G-**P**-(GS)$_6$LD-{**insert**}-(GS)$_6$G-**P**-(GS)$_6$-LEH$_6$KLN |
| $PE_3P$ "3-mesh" | 22,632 | **$E_3$**-LD |
| $PE_6P$ "6-mesh" | 28,756 | [**$E_3$**-LD]$_2$ |
| $PE_{12}P$ "12-mesh" | 41,004 | [**$E_3$**-LD]$_4$ |
| $PE_{24}P$ "24-mesh" | 65,501 | [**$E_3$**-LD]$_8$ |
| **P(E$_n$P)$_m$* series (multistickers)** | | |
| $E_6^C$ | 15,060 | MRGSH$_6$GSVD-**$E_3$**-LD-**$E_3$**-LEH$_6$KLC |
| $E_6P^C$ | 21,903 | MRGSH$_6$GSVD-[**$E_3$**-LD]$_2$-(GS)$_6$G-**P**-(GS)$_6$-LEH$_6$KLC |
| $PE_6P^C$ | 28,745 | MRGSH$_6$GSVD(GS)$_6$G-**P**-(GS)$_6$LD-[**$E_3$**-LD]$_2$-(GS)$_6$G-**P**-(GS)$_6$-LEH$_6$KLC |
| $P(E_6P)_2^C$ | 47,836 | MRGSH$_6$GSVD(GS)$_6$G-**P**-(GS)$_6$-{LD-[**$E_3$**-LD]$_2$-(GS)$_6$G-**P**-(GS)$_6$}$_2$-LEH$_6$KLC |
| $P(E_6P)_4^C$ | 86,018 | MRGSH$_6$GSVD(GS)$_6$G-**P**-(GS)$_6$-{LD-[**$E_3$**-LD]$_2$-(GS)$_6$G-**P**-(GS)$_6$}$_4$-LEH$_6$KLC |

**Supplementary Table 2.3. ESI-MS data for large *n*-probes.** The remaining proteins ($PE_6P$ and smaller) were validated by double-stranded DNA sequencing of the corresponding plasmid. All –Cys terminated proteins were blocked with iodoacetamide (+IAM, Δ = +57 Da) prior to analysis.

| Protein | Predicted (Da) | +IAM (Da) | Observed (Da) | % error |
|---|---|---|---|---|
| $E_{12}{}^{C}$* | 27,308 | 27,365 | 27,319 | 0.167% |
| $E_{12}P^{C}$ | 34,151 | 34,208 | 34,211 | 0.009% |
| $PE_{12}P^{C}$ | 40,994 | 41,051 | 41,043 | 0.019% |
| $PE_{12}P$ | 41,004 | - | 41,021 | 0.042% |
| $E_{24}{}^{C}$ | 51,805 | 51,862 | 51,867 | 0.010% |
| $E_{24}P^{C}$ | 58,647 | 58,704 | 58,710 | 0.010% |
| $PE_{24}P^{C}$ | 65,490 | 65,547 | 65,552 | 0.008% |
| $PE_{24}P$ | 65,501 | - | 65,506 | 0.007% |
| $E_{48}{}^{C}$ | 100,798 | 100,855 | 100,862 | 0.007% |
| $E_{48}P^{C}$ | 107,640 | 107,697 | 107,702 | 0.005% |
| $PE_{48}P^{C}$ | 114,483 | 114,540 | 114,573 | 0.029% |
| $P(E_6P)_2{}^{C}$ | 47,847 | 47,904 | 47,906 | 0.004% |
| $P(E_6P)_4{}^{C}$ | 86,018 | 86,075 | 86,080 | 0.006% |

**observed by MALDI*

**Supplementary Table 2.4. Experimental parameters and exponent data for *n*-mesh.** *M* represents the true molecular weight of each *n*-mesh (including P domains). The mesh size was calculated as $R_{mesh} = 2\left(3/4\pi n_j\right)^{1/3}$, i.e. two times the radius of a sphere with a volume equal to the mean volume per site. A cluster dimension of $c$ = 1.89 nm was taken for calculating $l$, the bounds of the looping integral $G_L$. The fraction of elastically effective chains, $G'_\infty / G_{phantom}$, is the average value measured from rheology ($n \geq 2$ independent measurements) with $G_{phantom} = \rho RT(1-2/f)/M$, where $f$ = 5 for a pentameric network junction. Each $a_s$ and $\beta_i$ represent the molecular weight exponents calculated from power-law fits to the diffusivity data in **Supplementary Figure 2.9**. $x_{calc} = l_{calc}/c$ was determined from **Eq. S15** using the experimental $G'/G_{phantom}$ and the coarse-grained values of $N$ and $b$ for each mesh (**Supplementary Table 2.5**). Each $x_{min} = l_{min}/c$ was used to generate the master plot in **Figure 2.2D**, and was determined from minimizing the residuals between $K_1/K_2$ and **Eq. 1** in each mesh (**Supplementary Figures 2.11** and **2.12**). $[B]$ and $[L]$ were determined from **Eq. S14** and **S16** respectively using $x_{min}$.

| | 3-mesh | 6-mesh | 12-mesh | 24-mesh |
|---|---|---|---|---|
| $M$ (Da) | 22,632 | 28,756 | 41,004 | 65,501 |
| $R_{mesh}$ (nm) | 12.2 | 13.2 | 14.8 | 17.3 |
| $G'_\infty/G_{phantom}$ | 0.59 | 0.74 | 0.82 | 0.67 |
| $x_{calc}$ (nm) | 0.15 | 0.28 | 0.42 | 0.80 |
| $x_{min}$ (nm) | 0.24 | 0.26 | 0.43 | 0.35 |
| $[B]$ | 0.11 | 0.49 | 0.66 | 0.79 |
| $[L]$ | 0.13 | 0.07 | 0.08 | 0.05 |
| | $D_S \sim N^{\alpha}$, $K_i \sim N^{\beta}$ | | | |
| $\alpha_0$ | -1.4 ± 0.1 | -1.5 ± 0.0 | -1.4 ± 0.1 | -1.3 ± 0.1 |
| $\alpha_1$ | -1.0 ± 0.1 | -0.9 ± 0.1 | -1.0 ± 0.1 | -1.0 ± 0.1 |
| $\alpha_2$ | -1.6 ± 0.1 | -1.5 ± 0.1 | -1.3 ± 0.2 | -1.4 ± 0.1 |
| $\beta_1 = \alpha_0 - \alpha_1$ | -0.4 ± 0.1 | -0.6 ± 0.1 | -0.4 ± 0.1 | -0.3 ± 0.1 |
| $\beta_2 = \alpha_1 - \alpha_2$ | 0.6 ± 0.2 | 0.6 ± 0.1 | 0.3 ± 0.2 | 0.4 ± 0.1 |
| $\beta_1 - \beta_2$ | -1.0 ± 0.2 | -1.2 ± 0.1 | -0.7 ± 0.2 | -0.7 ± 0.2 |

**Supplementary Table 2.5. Coarse graining of probe size based on the Flory characteristic ratio $C_\infty$ = 2.51** (*28*). The value $n_p$ reflects the number of peptide bonds between each P domain on PE$_n$P-type probes. The molecular weight of this inter-sticker region ("MW$_{eff}$") is also shown. $R_{probe} = (C_\infty n_p l_p)^{1/2} = bN^{0.5}$ and $R_{max} = n_p l_p$ were calculated taking $l_p$ = 0.380 nm as the "virtual" length of each peptide bond (linear $C_\alpha$–$C_\alpha$ distance). The length of a Kuhn monomer is $b = C_\infty n_p l_p{}^2 / R_{max}$, and the equivalent freely jointed chain is composed of $N = R_{max}{}^2 / C_\infty n_p l_p{}^2$ such monomers, each with an effective molar mass of $M_0$ (*25*). The parameters calculated below were also used to estimate various mesh parameters in **Supplementary Table 2.4**, assuming "size-matched" networks ($N = M$).

| | **MW$_{eff}$ (Da)** | $n_p$ | $R_{probe}$ (nm) | $R_{max}$ (nm) | $b$ (nm) | $N$ | $M_0$ (Da) |
|---|---|---|---|---|---|---|---|
| **3-probe** | 8,121 | 104 | 6.1 | 39.5 | 0.95 | 41 | 196 |
| **6-probe** | 14,245 | 181 | 8.1 | 68.8 | 0.95 | 72 | 198 |
| **12-probe** | 26,493 | 335 | 11.0 | 127.3 | 0.95 | 133 | 199 |
| **24-probe** | 50,990 | 643 | 15.3 | 244.3 | 0.95 | 256 | 199 |
| **48-probe** | 99,982 | 1259 | 21.4 | 478.4 | 0.95 | 502 | 199 |

### 2.7.4 Supplementary Figures

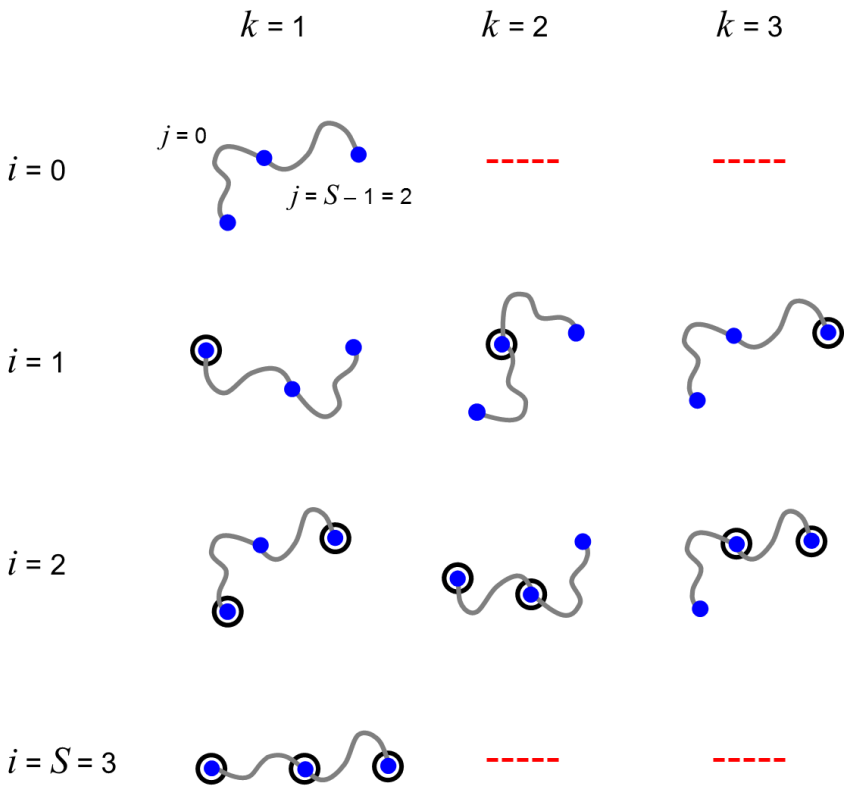


**Supplementary Figure 2.1. Schematic of all possible binding configurations of a chain with *S* = 3 stickers.** The chain has $k \leq C(S,i)$ possible bound states for each $i \leq S$ number of bound stickers, where $C(S,i)$ is the binomial coefficient. The sum $j = S-1$ runs over the total number of independent blocks.

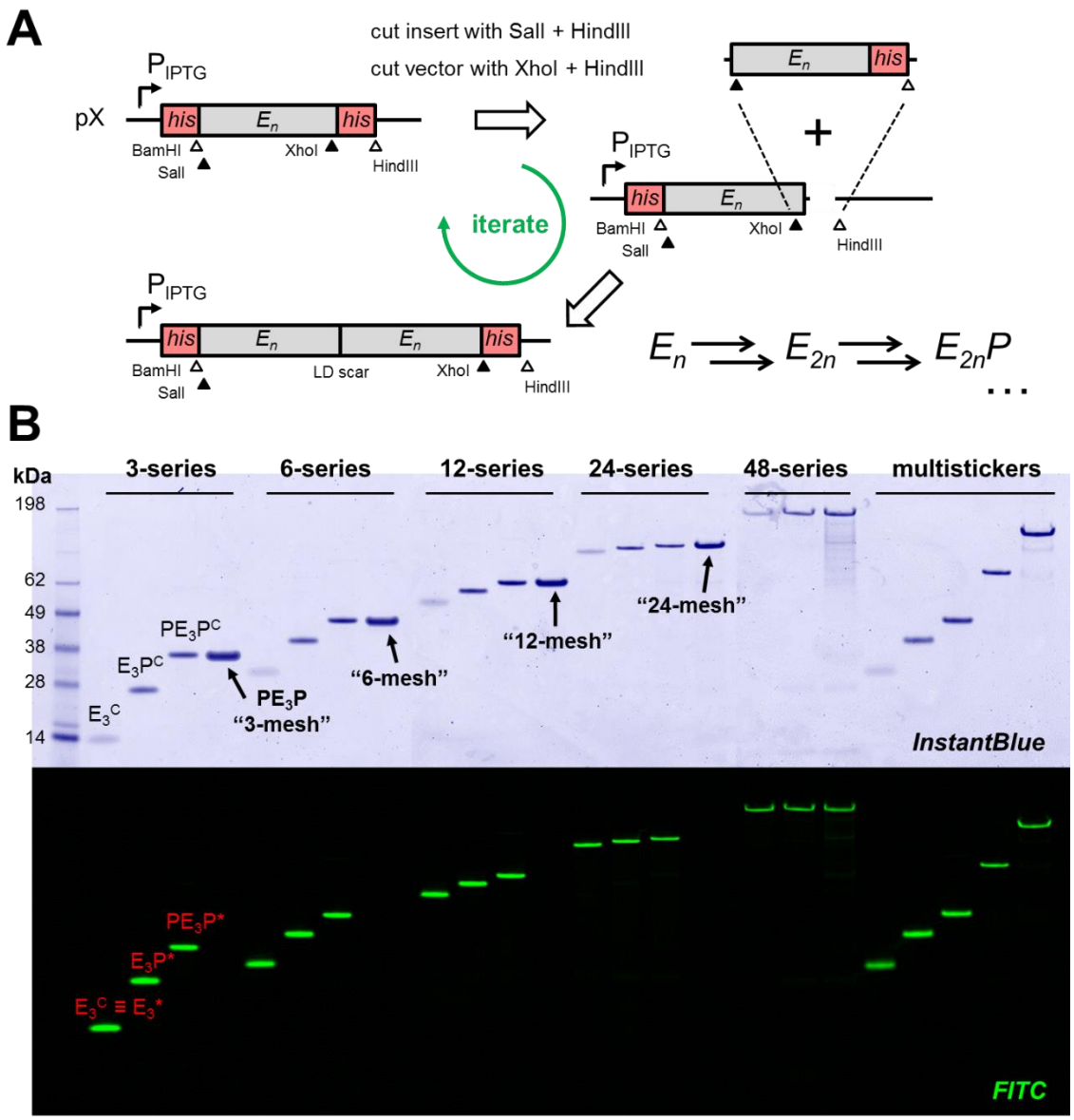


**Supplementary Figure 2.2. Outline of cloning scheme (recursive directed ligation)**. (**A**) To perform chain extension, a "pX ≡ pQE-80L-*ΔXhoI*" is cut with *Sal*I and *Hind*III, and an insert is cut with *Xho*I and *Hind*III. Ligation of the insert and vector produces the chain extended product with the same four sites on the new vector. The internal *Sal*I-*Xho*I site is destroyed during the ligation, generating an "LD" scar. (**B**) SDS-PAGE gels of the 21 unique artificial proteins prepared by this method (full sequences are presented in **Supplementary Table 2.2**). All FRAP probes were site-specifically labeled at their C-terminal Cys residue with fluorescein-5-maleimide (the labeled -Cys terminated proteins are denoted with *).

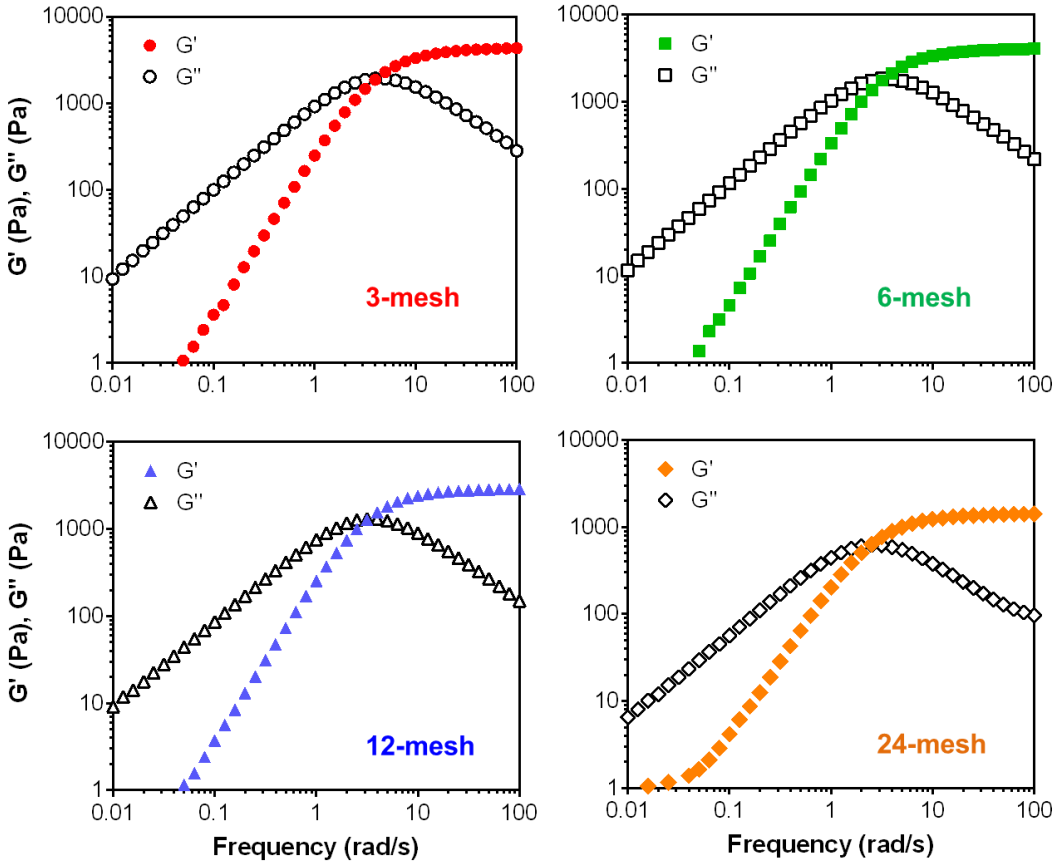


**Supplementary Figure 2.3. Linear oscillatory shear rheology of hydrogels with varying mesh sizes.** Hydrogels were prepared by swelling lyophilized mesh proteins in 100 mM phosphate buffer, pH 7.4, at a concentration of 10% (*w*/*v*). Frequency sweeps were performed at a fixed strain amplitude of 1% between 0.01 and 100 rad $s^{-1}$.

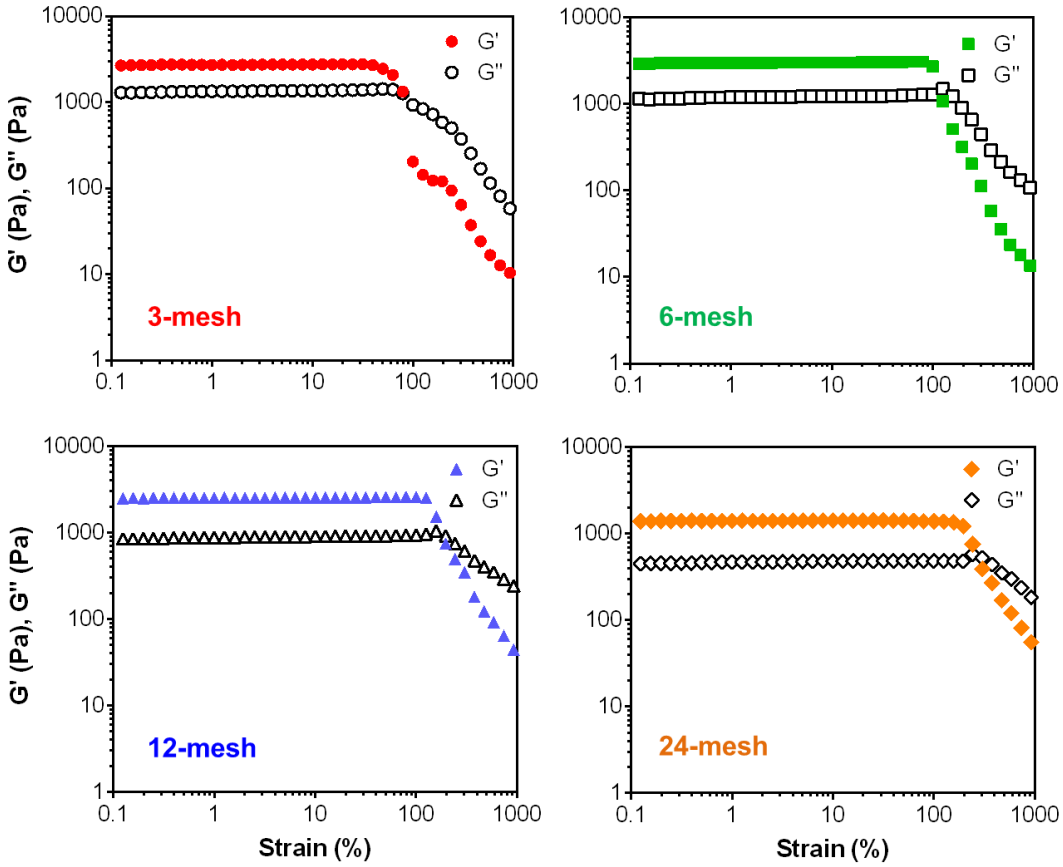


**Supplementary Figure 2.4. Non-linear rheology of hydrogels (LAOS) with varying mesh sizes.** Large-amplitude oscillatory shear was performed on 10% hydrogels at 10 rad $s^{-1}$ between 0.1 and 1000% strain. At a fixed protein concentration, larger meshes have an increased critical strain (yield strain), as well as a decreased yield stress (**Supplementary Figure 2.5**).

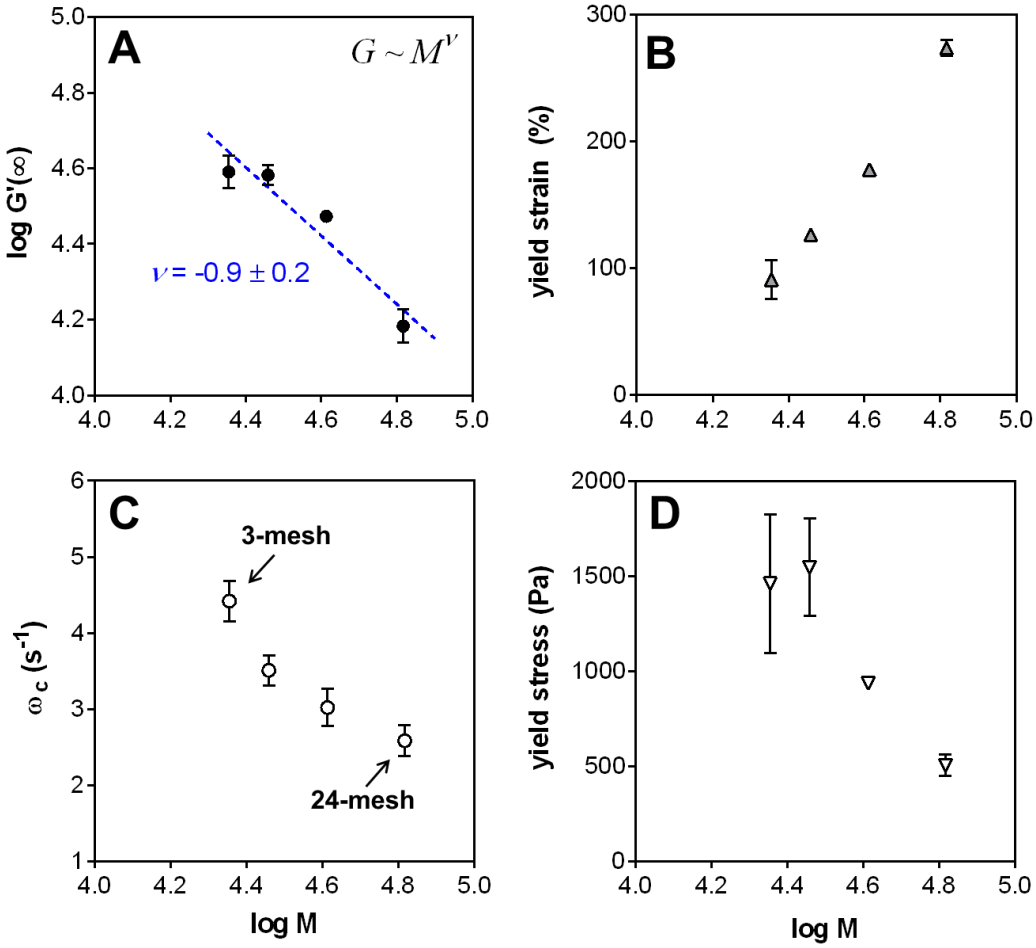


**Supplementary Figure 2.5. Summary of rheological properties of hydrogels with varying mesh sizes.** Networks were prepared at a fixed protein concentration of 10% (*w/v*) in 100 mM phosphate buffer, pH 7.4 (points in each graph represent μ ± σ for 2 – 3 independent gel preparations). (**A**) The terminal storage modulus $G'(\infty)$ (taken as $G'(100)$ from **Supplementary Figure 2.3**) follows the molecular weight dependence expected from rubber elasticity theory $(G' = \rho RT / M)$. (**B**) Gels with larger meshes have a greater terminal strain. Terminal strain is taken as the point at which $G' = G''$ in the LAOS curve (**Supplementary Figure 2.4**). (**C**) The network relaxation rate (crossover frequency, $\omega_c$) shows a weak dependence on mesh size. The crossover frequency is taken as the point at which $G' = G''$ in the frequency sweep (**Supplementary Figure 2.3**). (**D**) Larger meshes have an apparently lower yield stress.

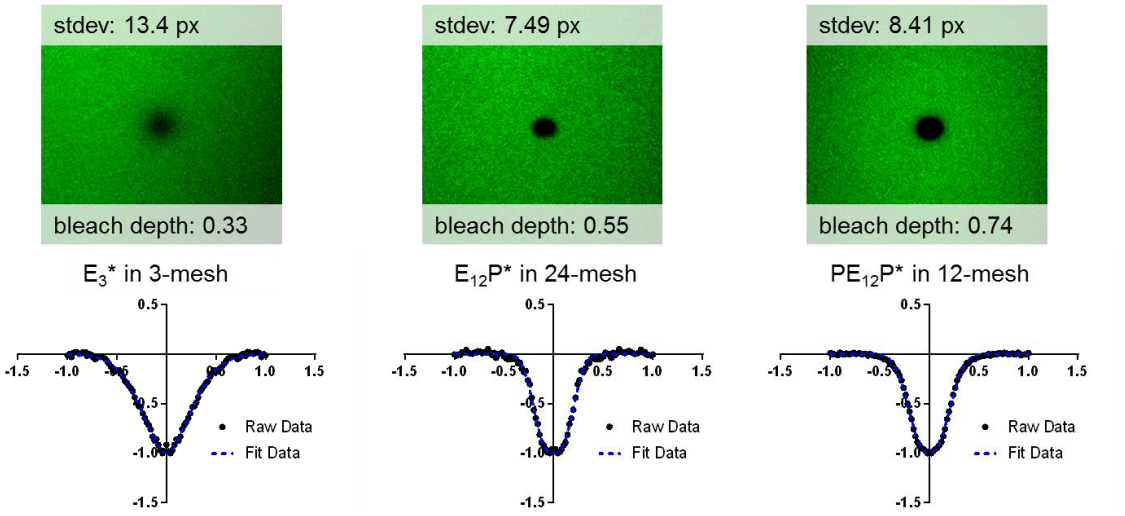


**Supplementary Figure 2.6. Variable bleach spot profiles for different probes.** (*Top*) Shown are representative post-bleach images for several probes in several different meshes. (*Bottom*) To control for this variance, the fluorescence intensity profile across the bleach spot was fit to a generalized Gaussian, and the spot size information was supplied to a tracking algorithm that extracted the normalized fluorescence recovery curves. The spot size information from the fit was also supplied during the estimation of $D_{eff} = D_S$.

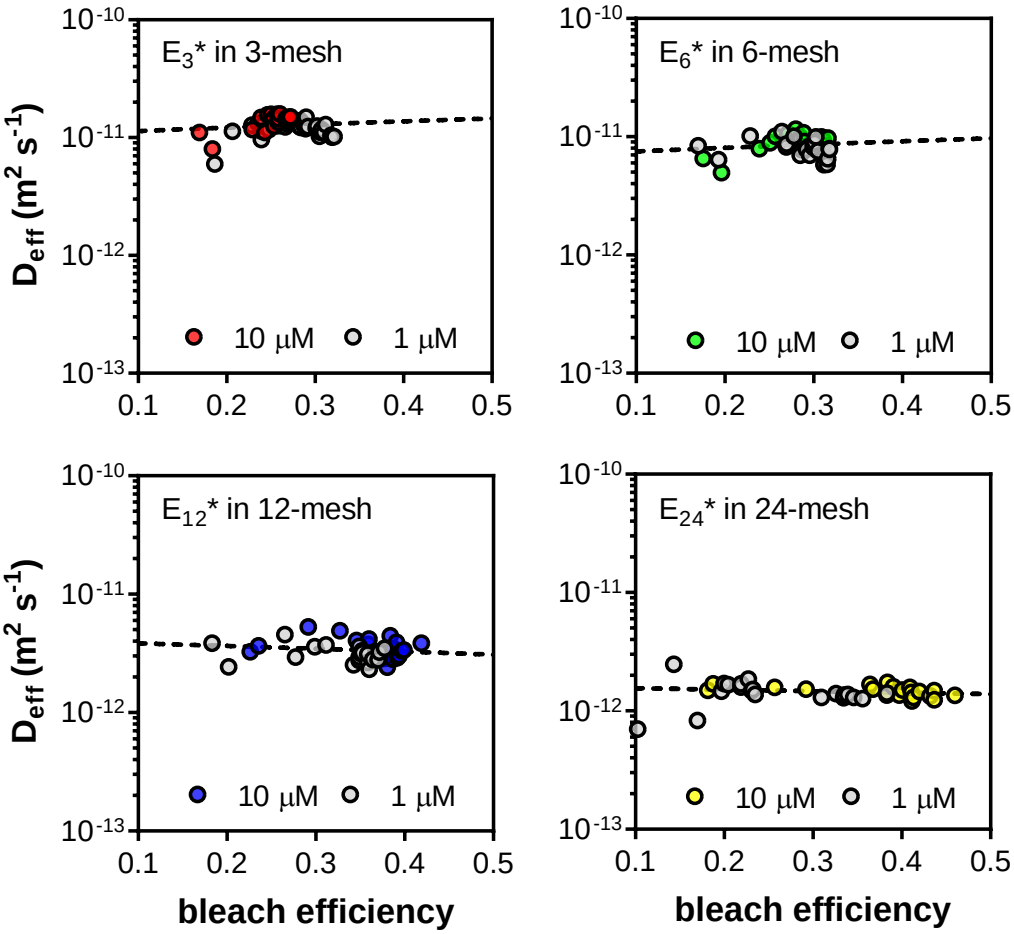


**Supplementary Figure 2.7. Validation of the FRAP analysis procedure in different meshes.** 173 control FRAP traces were acquired for four test chains in size-matched ($N = M$) meshes at varying bleach efficiencies and two different probe concentrations. The effective mobilities $D_{eff} = D_S$ obtained from this dataset are independent of the bleach efficiency, bleach spot size, and probe concentration. Dashed lines show linear regressions to $D_{eff}$ versus bleach efficiency for both probe concentrations within each mesh. No regression line has a slope significantly different from zero ($P > 0.33$). Moreover, for a given probe concentration within each mesh, the standard deviation of $D_{eff}$ across the different bleach efficiencies does not exceed 25% of the mean $D_{eff}$ (i.e., $0.14 < \mu / \sigma < 0.25$).

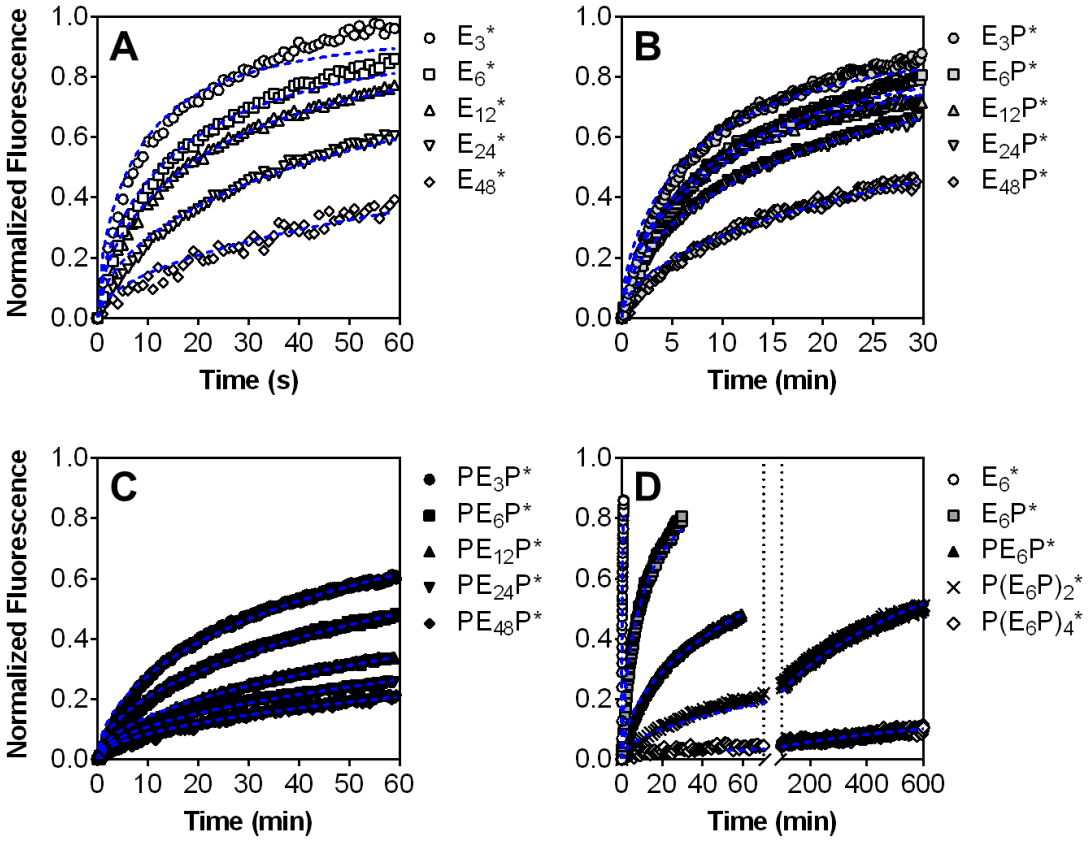


**Supplementary Figure 2.8. Representative FRAP recovery curves in "6-mesh" networks.** Fluorescent probes of various sizes, and with different numbers of associative domains ("stickers") were used to label 10% $PE_6P$ hydrogels (probe concentration ~ 10 μM), then photobleached. Fluorescence recovery was monitored for varying lengths of time, typically until at least ~50% of the original intensity was restored (within 1 – 2 h for most probes). Shown are recovery traces for (**A**) $E_n$* probes, (**B**) $E_nP$* probes, (**C**) $PE_nP$* probes, and (**D**) $P(E_nP)_m$* multisticker probes. Each recovery trace was fit to **Eq. S4**, which allowed the effective diffusivity $D_{eff} = D_S$ to be determined using **Eq. 4**.

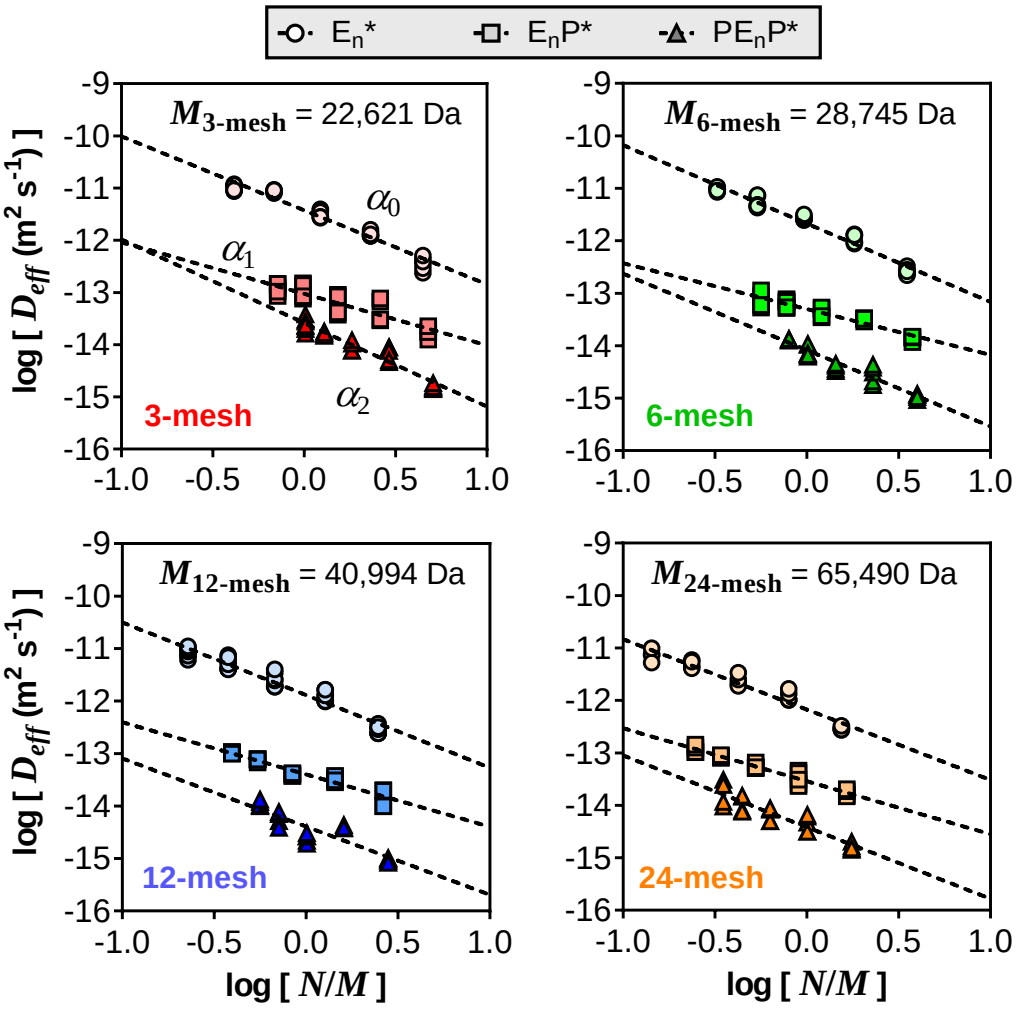


**Supplementary Figure 2.9. Molecular weight dependence of $D_S$ for probes in different meshes** Shown are 298 effective diffusivities for each probe, determined from fits to FRAP traces (**Supplementary Figure 2.8**, $n \geq 4$ measurements per probe, per mesh). Power-law fits were used to determined molecular weight scaling of each probe series, and the exponents for these fits are presented in **Supplementary Table 2.4**. As described in the main text, each probe series determines a different $D_S$: $D_0$ ($E_n$*), $D_1$ ($E_n$P*), and $D_2$ ($PE_n$P*).

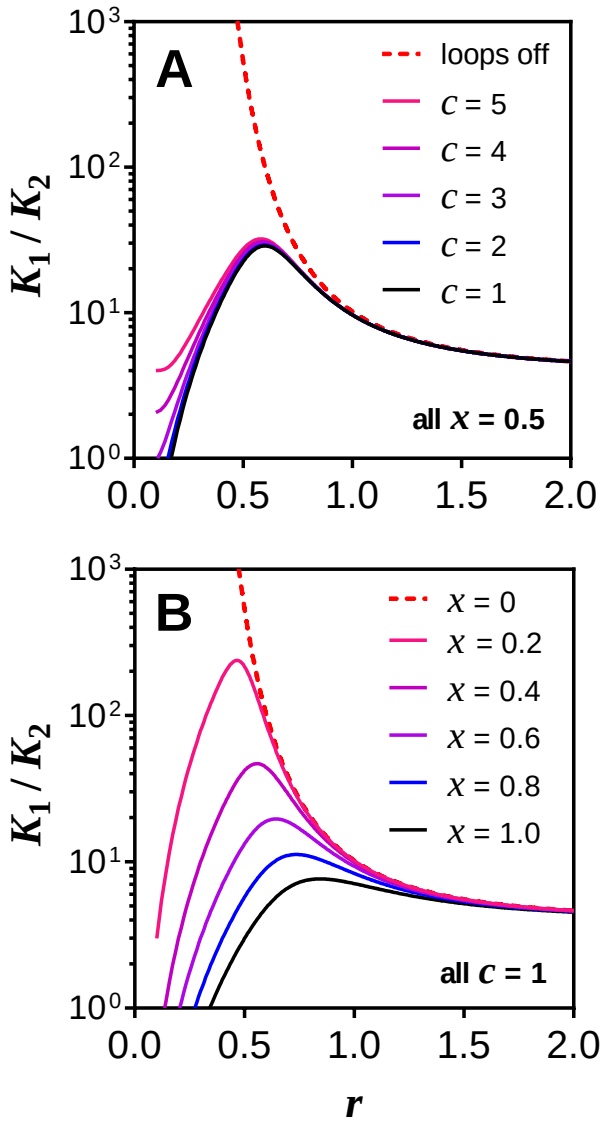


**Supplementary Figure 2.10. Independence of Eq. 1 on *c* for fixed *x* = *l* / *c*.** (**A**) The cluster dimension was taken to be $c = 1 – 5$, $R_{mesh} = 10$, $b = 1$, and $x$ was fixed at 0.5. Shown are predictions for $K_1 / K_2$ for each of these five cases from **Eq. 1**, along with **Eq. 2** for the "loops off" case. The behavior of **Eq. 1** is insensitive to the choice of $c$ for $c < R_{mesh}$. (**B**) For a fixed cluster size of $c = 1$, the limits of the looping integral (specified by $x = l / c$) determine the behavior of **Eq. 1**.

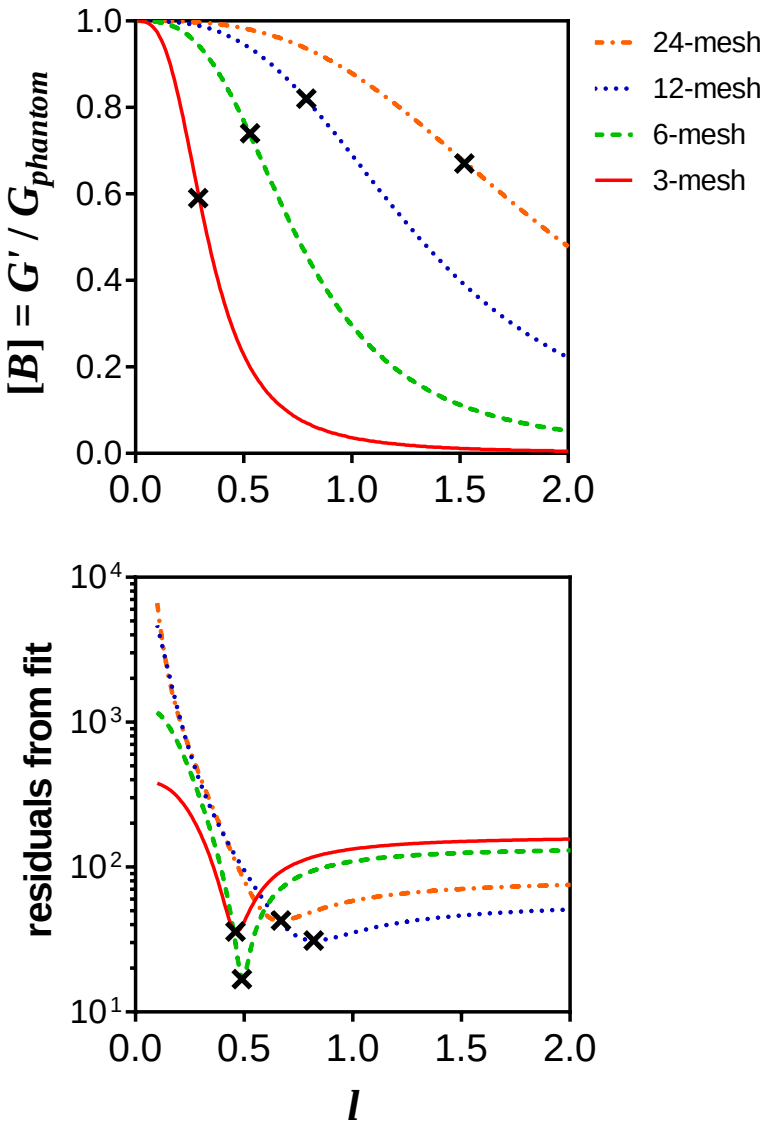


**Supplementary Figure 2.11. Selection criteria for the limits of the looping integral.** We expect $l \sim O(b)$ such that $x = l/c \approx 0.5$ from $c$ = 1.89 nm where $b$ = 0.95 nm. (*Top*) Matching the experimental fraction of elastically effective chains to predictions from **Eq. S15** fixes this limit precisely, providing $x_{calc}$ for each mesh. (*Bottom*) Alternatively, minimizing the $K_1 / K_2$ residuals from **Eq. 1** in each mesh (**Supplementary Figure 2.12**) provides $x_{min}$. The calculated and residuals-minimized $x$ values are all $\approx 0.5$ as expected.

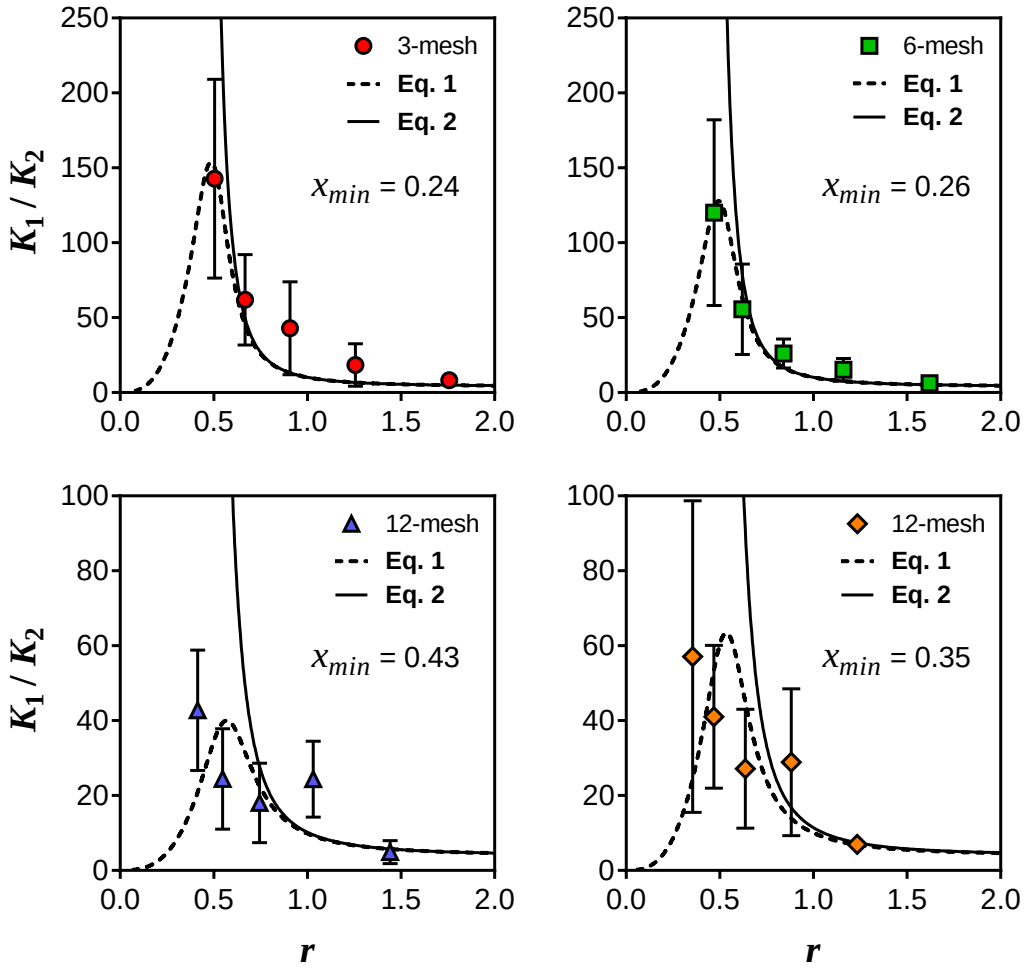


**Supplementary Figure 2.12. Minimized $K_1 / K_2$ residuals in each mesh, analogous to Figure 2.3D.** The values of $x_{min} = l_{min} / c$ determined in **Supplementary Figure 2.11** were used to plot **Eq. 1**, along with the coarse-grained data ($b$, $N$, $R_{mesh}$) on each mesh shown in **Supplementary Tables 2.4** and **2.5**.

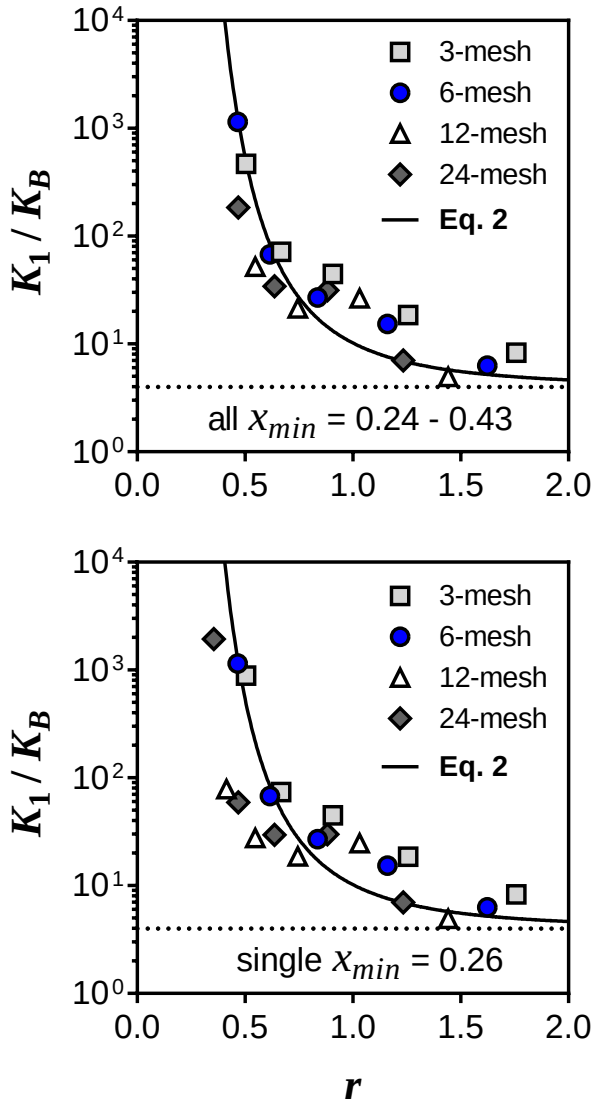


**Supplementary Figure 2.13. A single choice of $x_{min}$ = 0.26 is sufficient to collapse the binding data in each mesh onto Eq. 2** (*Bottom*), although the fit is slightly improved by selecting $x_{min}$ differently in each mesh (*Top*, same as **Figure 2.3D**). The top plot summarizes 271 measurements (out of 298 total, loops are overestimated at 2 of 20 probe-mesh ratios), whereas the bottom curve contains all 298 measurements, but underestimates looping contributions in the 12- and 24-mesh.

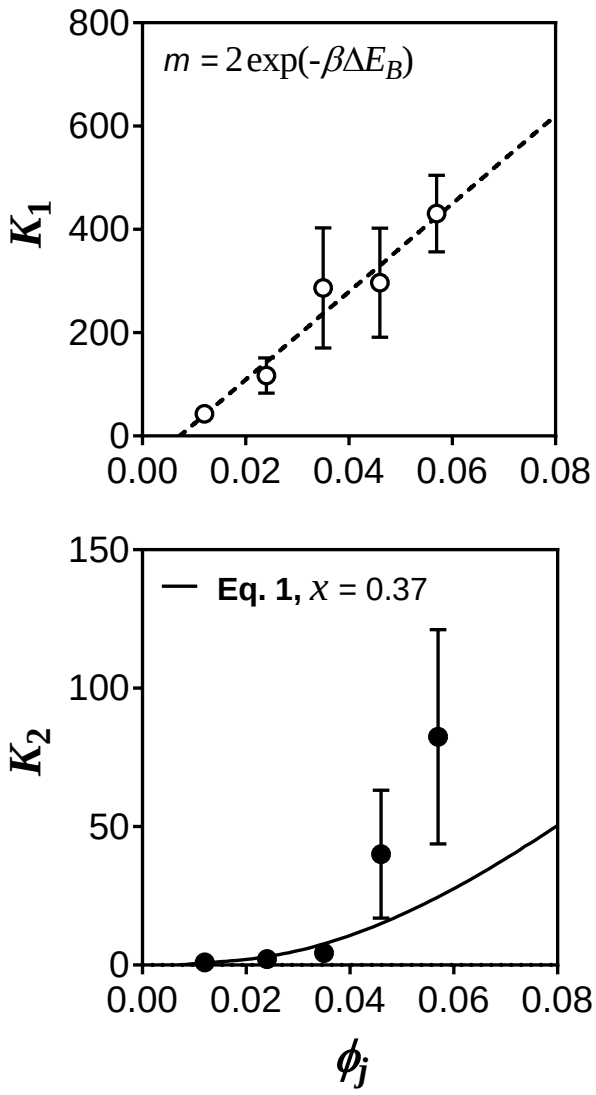


**Supplementary Figure 2.14. Dependence of $K_1$ and $K_2$ on junction density in a 6-mesh network.** The top panel shows a linear regression to the $K_1$ data, which provides an estimate for the network binding energy $\Delta E_B = -4.94$ kcal mol$^{-1}$. $K_2$ was estimated from this regression curve using **Eq. 1**, $x$ = 0.37, and the experimental 6-mesh data (**Supplementary Tables 2.4** and **2.5**). Data points represent mean ± std. deviation for a total of $n$ = 76 measurements, with ≥ 2 measurements per probe per concentration.

## 2.8 References


1. C. A. J. Hoeve, P. J. Flory, The Elastic Properties of Elastin. *J. Am. Chem. Soc.* **80**, 6523-6526 (1958).

2. H. G. Schild, D. A. Tirrell, Microcalorimetric Detection of Lower Critical Solution Temperatures in Aqueous Polymer-Solutions. *J Phys Chem-Us* **94**, 4352-4356 (1990).

3. D. E. Meyer, A. Chilkoti, Quantification of the effects of chain length and concentration on the thermal behavior of elastin-like polypeptides. *Biomacromolecules* **5**, 846-851 (2004).

4. S. M. Law, J. K. Gagnon, A. K. Mapp, C. L. Brooks, 3rd, Prepaying the entropic cost for allosteric regulation in KIX. *Proc Natl Acad Sci U S A* **111**, 12067-12072 (2014).

5. K. P. Ravindranathan, E. Gallicchio, R. A. Friesner, A. E. McDermott, R. M. Levy, Conformational Equilibrium of Cytochrome P450 BM-3 Complexed with N-Palmitoylglycine: A Replica Exchange Molecular Dynamics Study. *J. Am. Chem. Soc.* **128**, 5786-5791 (2006).

6. I. F. Thorpe, C. L. Brooks, Molecular evolution of affinity and flexibility in the immune system. *Proc Natl Acad Sci USA* **104**, 8821-8826 (2007).

7. J. Zimmermann *et al.*, Antibody evolution constrains conformational heterogeneity by tailoring protein dynamics. *Proc Natl Acad Sci U S A* **103**, 13722-13727 (2006).

8. S.-R. Tzeng, C. G. Kalodimos, Protein activity regulation by conformational entropy. *Nature* **488**, 236-240 (2012).

9. I. V. Nesmelova *et al.*, Lactose Binding to Galectin-1 Modulates Structural Dynamics, Increases Conformational Entropy, and Occurs with Apparent Negative Cooperativity. *J Mol Biol* **397**, 1209-1230 (2010).

10. W. C. Yount, H. Juwarker, S. L. Craig, Orthogonal Control of Dissociation Dynamics Relative to Thermodynamics in a Main-Chain Reversible Polymer. *J. Am. Chem. Soc.* **125**, 15302-15303 (2003).

11. W. C. Yount, D. M. Loveless, S. L. Craig, Small-Molecule Dynamics and Mechanisms Underlying the Macroscopic Mechanical Properties of Coordinatively Cross-Linked Polymer Networks. *J. Am. Chem. Soc.* **127**, 14488-14496 (2005).

12. D. Xu, S. L. Craig, Scaling Laws in Supramolecular Polymer Networks. *Macromolecules* **44**, 5465-5472 (2011).

13. Q. Chen, G. J. Tudryn, R. H. Colby, Ionomer dynamics and the sticky Rouse model. *J Rheol* **57**, 1441-1462 (2013).

14. T. Annable, R. Buscall, R. Ettelaie, D. Whittlestone, The Rheology of Solutions of Associating Polymers - Comparison of Experimental Behavior with Transient Network Theory. *J Rheol* **37**, 695-726 (1993).

15. S. C. Grindy *et al.*, Control of hierarchical polymer mechanics with bioinspired metal-coordination dynamics. *Nat Mater* **14**, 1210-1216 (2015).

16. W. A. Petka, J. L. Harden, K. P. McGrath, D. Wirtz, D. A. Tirrell, Reversible hydrogels from self-assembling artificial proteins. *Science* **281**, 389-392 (1998).

17. B. D. Olsen, J. A. Kornfield, D. A. Tirrell, Yielding Behavior in Injectable Hydrogels from Telechelic Proteins. *Macromolecules* **43**, 9094-9099 (2010).

18. D. D. McKinnon, D. W. Domaille, J. N. Cha, K. S. Anseth, Biophysically defined and cytocompatible covalently adaptable networks as viscoelastic 3D cell culture systems. *Adv Mater* **26**, 865-872 (2014).

19. F. Herbst, S. Seiffert, W. H. Binder, Dynamic supramolecular poly(isobutylene)s for self-healing materials. *Polym Chem* **3**, 3084-3092 (2012).

20. S. Tang, A. Habicht, S. Li, S. Seiffert, B. D. Olsen, Self-Diffusion of Associating Star-Shaped Polymers. *Macromolecules*, (2016).

21. P. B. Rapp *et al.*, Analysis and Control of Chain Mobility in Protein Hydrogels. *J. Am. Chem. Soc.*, (2017).

22. A. N. Semenov, M. Rubinstein, Thermoreversible Gelation in Solutions of Associative Polymers. 1. Statics. *Macromolecules* **31**, 1373-1385 (1998).

23. L. G. Baxandall, Dynamics of reversibly crosslinked chains. *Macromolecules* **22**, 1982-1988 (1989).

24. M. Rubinstein, A. N. Semenov, Thermoreversible Gelation in Solutions of Associating Polymers. 2. Linear Dynamics. *Macromolecules* **31**, 1386-1397 (1998).

25. M. Rubinstein, R. H. Colby, *Polymer Physics*. (Oxford University Press, 2003).

26. D. M. Soumpasis, Theoretical-Analysis of Fluorescence Photobleaching Recovery Experiments. *Biophys J* **41**, 95-97 (1983).

27. B. L. Sprague, R. L. Pego, D. A. Stavreva, J. G. McNally, Analysis of binding reactions by fluorescence recovery after photobleaching. *Biophys J* **86**, 3473-3495 (2004).

28. L. C. DeBolt, J. E. Mark, Theoretical study of the thermoelastic properties of elastin model chains. *Polymer* **28**, 416-422 (1987).

29. S. Fluegel, K. Fischer, J. R. McDaniel, A. Chilkoti, M. Schmidt, Chain Stiffness of Elastin-Like Polypeptides. *Biomacromolecules* **11**, 3216-3218 (2010).

30. W. Hassouneh, E. B. Zhulina, A. Chilkoti, M. Rubinstein, Elastin-like Polypeptide Diblock Copolymers Self-Assemble into Weak Micelles. *Macromolecules* **48**, 4183-4195 (2015).

31. L. Mandelkern, W. L. Mattice, Unperturbed dimensions of sequential copolypeptides containing glycine, L-alanine, L-proline, and γ-hydroxy-L-proline. *Biochemistry* **10**, 1934-1942 (1971).

32. W. G. Miller, C. V. Goebel, Dimensions of protein random coils. *Biochemistry* **7**, 3925-3935 (1968).

33. S. C. Tang, M. Z. Wang, B. D. Olsen, Anomalous Self-Diffusion and Sticky Rouse Dynamics in Associative Protein Hydrogels. *J. Am. Chem. Soc.* **137**, 3946-3957 (2015).

34. Y. Harpaz, M. Gerstein, C. Chothia, Volume changes on protein folding. *Structure* **2**, 641-649 (1994).

35. V. N. Malashkevich, R. A. Kammerer, V. P. Efimov, T. Schulthess, J. Engel, The crystal structure of a five-stranded coiled coil in COMP: A prototype ion channel? *Science* **274**, 761-765 (1996).

*Chapter 3*

# VISCOELASTIC PHASE PATTERNING IN ARTIFICIAL PROTEIN HYDROGELS

## 3.1 Abstract

Viscoelastic forces can affect the dynamics of pattern formation during phase separation in polymeric materials. We programmed an artificial protein hydrogel to undergo viscoelastic phase separation above a critical temperature set point. Highly dynamic phase patterns that coarsened under the influence of a mechanical stress balance spontaneously emerged in these gels. Mild oxidative crosslinking promoted by photobleaching initialized the phase change locally, enabling patterning of non-equilibrium phase shapes into phase separating gels. Subsequent pattern evolution illustrated that a delicate balance of surface tension and viscoelastic stress controls pattern formation in viscoelastic materials.

## 3.2 Introduction

Phase separation can induce spontaneous pattern formation in polymeric materials (*1*). This provides a simple way to control material microstructure, enabling access to diverse and useful material properties (*2-4*). Simple solids and liquids develop either a bicontinuous or a droplet pattern in transition to a binary equilibrium state (*5*). Unique web- and sponge-like patterns can emerge in viscoelastic materials, which have dynamic properties intermediate between fluids and solids (*5-7*). Whereas pattern growth in simple mixtures is often scale invariant or “self-similar” (*8*), stress relaxation in viscoelastic materials can break the self-similarity or scale invariance of developing patterns (*9, 10*).

## 3.3 Results and Discussion

### 3.3.1 Sequence programmable phase separation in an artificial protein hydrogel

Thus far, viscoelastic effects on phase separation have been recognized in several isolated contexts (*6, 9, 11-14*), but remain difficult to predict and control. We hypothesized that artificial proteins could be programmed to routinely undergo viscoelastic phase separation by encoding them with two key features: *i*) the ability to self-assemble into a reversible network that stores and dissipates mechanical stress and *ii*) a phase transition temperature set point. Accordingly, we cloned and expressed a large (32 kDa), artificial protein polymer designated "PEP" that aimed to satisfy these criteria (**Figure 3.1A** and **Supplementary Table 3.1**). PEP comprises a flexible, water-soluble "E" midblock encoding 30 repeats of the elastin-like pentapeptide sequence $(VPGXG)_n$, where X is either V or E. This domain is flanked by two coiled-coil forming "P" endblocks (*15*) that promote reversible self-assembly of the protein monomer into a viscoelastic hydrogel (**Figure 3.1A** and **Supplementary Figure 3.1**) (*16-18*). We intended for the midblock to confer tunable phase behavior to these networks, owing to the thermally-induced phase transition above a lower critical solution temperature (LCST) that is a well-known property of elastins (*19-21*).

Based on the sequence of E, we predicted that PEP networks would display a simple, LCST-type phase transition at 70 °C (*21*). Surprisingly, cloud-point measurements were indicative of phase separation at much lower temperatures (*22*): at 38 °C, 5% (*w*/*v*) PEP gels separated into an aqueous phase (A) and a protein-rich coacervate phase (C) (**Figure**

**3.1B**). Moreover, the gels also exhibited reentrant behavior: continued heating above 64 °C completely restored protein miscibility, and a second cloud-point (UCST) became evident upon subsequent cooling. Similar measurements at other concentrations revealed an immiscibility loop in the *T*-$\varphi$ phase diagram and an apparent critical composition near 5% ($\phi_c$, **Figure 3.1C**). Phase diagrams of this class are rare (*23-27*), but are predicted from Flory theory when the polymer-solvent interaction parameter $\chi$ exceeds a critical value $\chi_c$ over a finite temperature range (*26*).

In an effort to understand this unexpected phase behavior, we performed cloud-point measurements on two additional engineered proteins (**Supplementary Table 3.1**). Concentrated solutions of a free, uncrosslinked "E" protein underwent phase separation near 85 °C, closer to the LCST predicted from sequence (**Supplementary Figure 3.2**). Using site-directed mutagenesis, we installed a single cysteine within this protein to promote disulfide crosslinking under oxidizing conditions. Dimerized solutions of this "$E_C$" protein displayed a depressed LCST at 63 °C (**Supplementary Figure 3.2**). These results imply that covalent and non-covalent interchain associations can significantly reduce the native transition temperature of elastins (*22, 23*). We attribute the reentrant behavior of PEP gels to gradual thermal unfolding of the P endblocks between 25 °C and 65 °C (*28*). Unfolding was evident from the mechanical softening of gels during heating (**Supplementary Figure 3.1**).

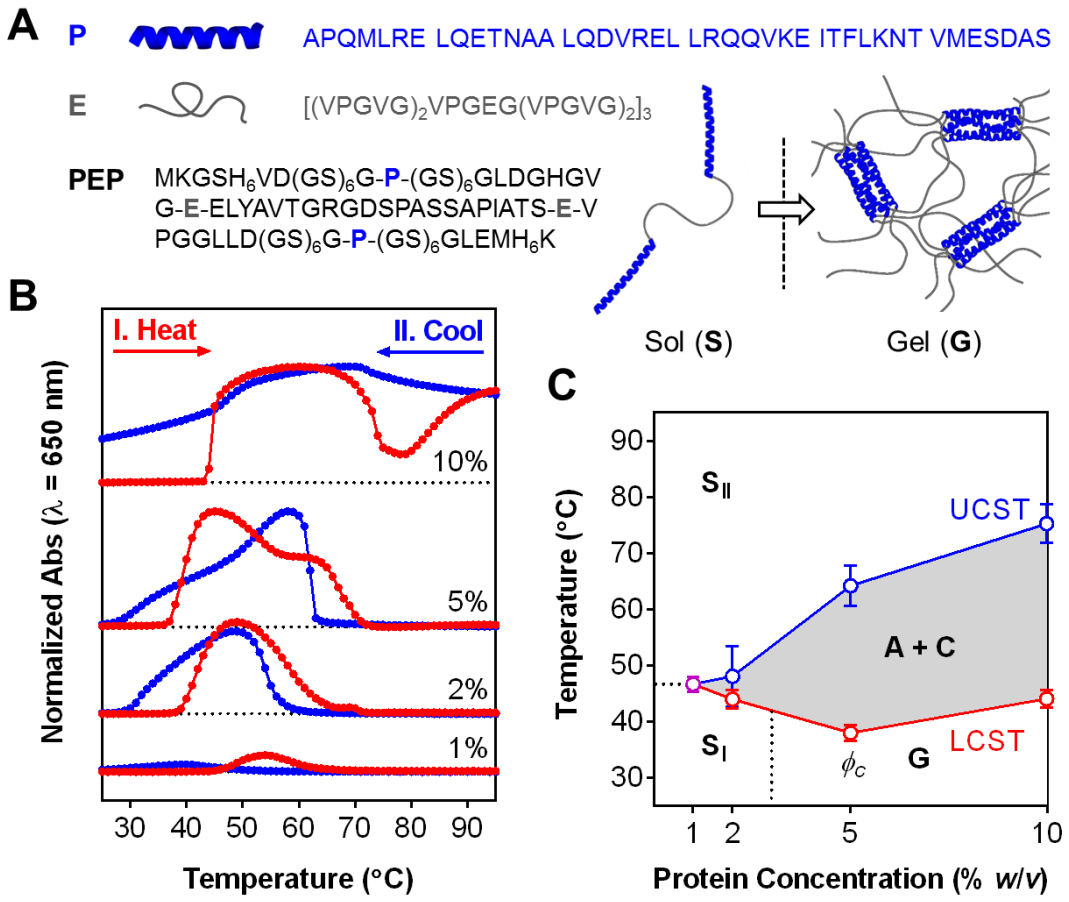


**Figure 3.1. Sequence programmable phase separation in an artificial protein hydrogel.** (**A**) Sequence of PEP. The protein comprises two coiled-coil forming "P" endblocks which flank a water soluble elastin-like "E" midblock. When swollen in aqueous buffer, the oligomerization of the endblocks drives reversible self-assembly into a viscoelastic gel. (**B**) Cloud-point measurements on PEP gels (pH 6.5) reveal phase separation and reentrant behavior (UCST > LCST). The gels were first heated then cooled over the range 25 °C to 95 °C at a rate of 3 °C $min^{-1}$. Gel turbidity was monitored at 650 nm. (**C**) The *T*-*φ* phase diagram of PEP contains an immiscibility loop: $S_I$, sol phase; G, reversible gel; A + C, aqueous phase (protein-poor) and coacervate phase (protein-rich); $S_{II}$, reentrant sol phase. Points represent mean ± SD ($n$ = 4).

### 3.3.2 Influence of viscoelastic stress on domain coarsening in PEP hydrogels

Next, we labeled PEP networks with a fluorescent, associative phase probe ($PE_CP$-*fm*, **Supplementary Figure 3.3**) in order to visualize pattern evolution during phase separation above the LCST. Following rapid heating to 50 °C, phase boundaries formed and the gel began to shrink. The developing coacervate (protein-rich) phase initially resisted this collapse by generating a transient, elastic restoring force. This caused the dramatic emergence of a highly interconnected, sponge-like structure that condensed as the stress relaxed (**Figure 3.2A**). Remarkably, coarsening by aqueous droplet coalescence internal to the coacervate completely reconfigured this early stage pattern over a period of several hours (**Figure 3.2B**). The resulting late stage pattern appeared to lack any characteristic length scale, as new aqueous droplets could still be seen nucleating within the coacervate.

This unusual type of pattern evolution is a hallmark of phase separation under the influence of viscoelastic stress (*29*). Tanaka has proposed that such web- and sponge-like patterns arise whenever the phase separation rate is faster than the internal stress relaxation rate of one of the phases (*6, 30*). Under these circumstances, early domain shape evolves to satisfy a mechanical force balance. Subsequent viscoelastic stress relaxation generates elastic instabilities that promote domain breakage. Simultaneously, regular coarsening modes (e.g., droplet ripening) erode the domains into circular architectures in order to minimize interfacial tension. The presence of multiple coarsening modes, each dominating at different times, breaks the self-similarity of the phase decomposition, producing irregular features with divergent length scales (*9, 10, 30*). Our results are in qualitative agreement with this picture.

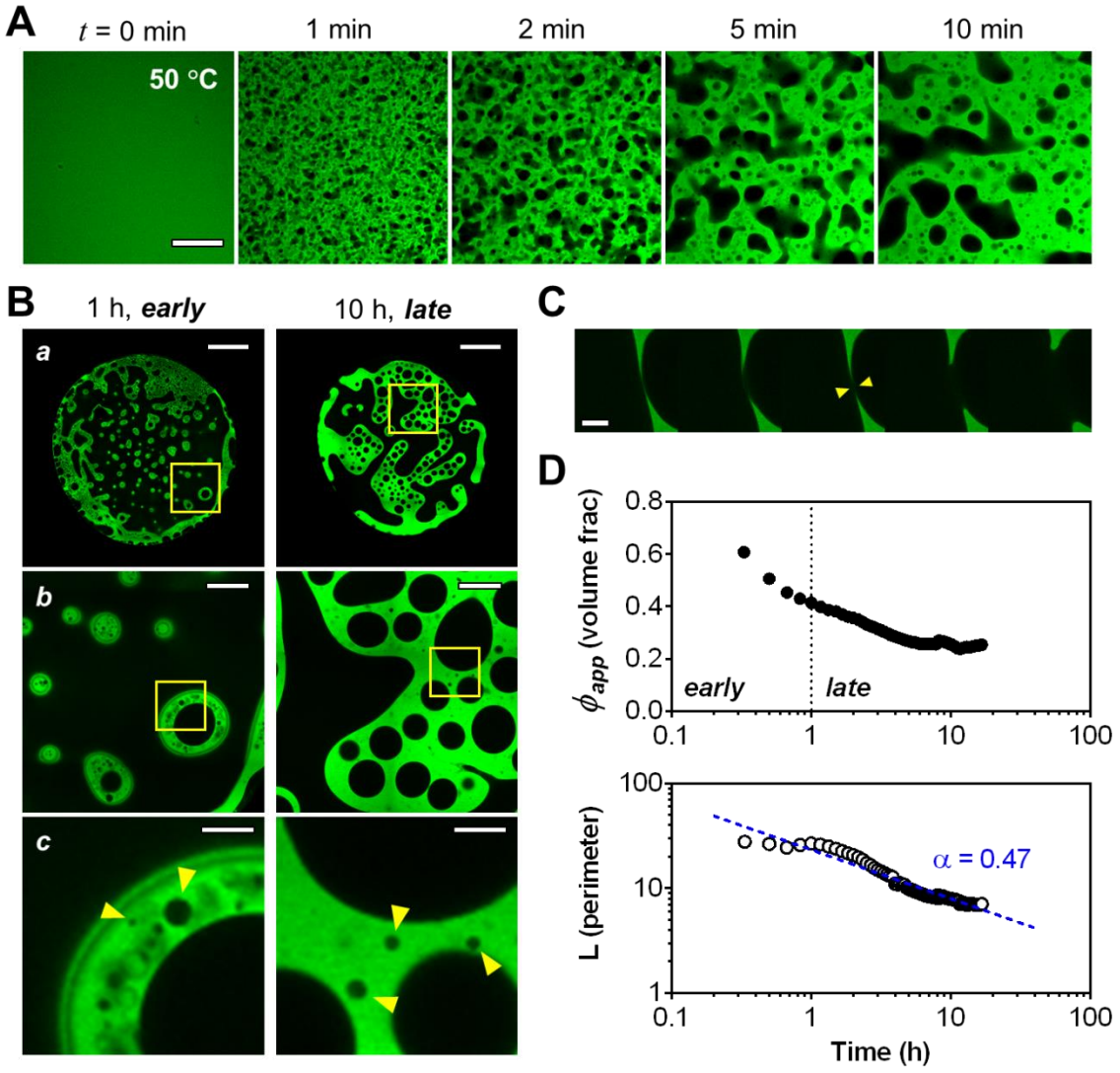


**Figure 3.2. Viscoelastic phase separation in PEP hydrogels.** (**A**) Rapid heating of 10% PEP gels to 50 °C promotes the emergence of a transient sponge-like phase within the first 10 min. Scale bar = 100 μm. (**B**) Overview images of early (1 h) and late (10 h) stage coarsening at several magnification levels reveal the absence of a characteristic length scale and the presence of multiple coarsening modes. Scale bars: (*a*) 1 mm, (*b*) 200 μm, (*c*) 50 μm. (**C**) Viscoelastic "breakage" events relaxed local domain configuration during the late stage (shown are five frames taken over 10 min, after 8 h of heating). Scale bar = 50 μm. (**D**) Quantitative analysis of pattern evolution. (*Top*) The volume fraction of the protein-rich coacervate phase decreased well into the late stage, violating a

prerequisite for self-similar domain growth. (*Bottom*) The interface line density (normalized total perimeter) obeyed an approximate power law of the form $L \sim t^{-\alpha}$ ($\alpha = 0.4 \pm 0.1$, $n = 4$).

---

Several additional features of late stage pattern evolution support the persistence of a viscoelastic coarsening mode. We routinely observed viscoelastic breakage events lasting several hours, in which slender coacervate tendrils "snapped" back to relax internal stress (**Figure 3.2C**). The apparent volume fraction of the coacervate phase obtained by image thresholding analysis decreased well into the late stage, implying a slowly changing phase composition (**Figure 3.2D**). This violates a prerequisite for scale invariant domain growth (*8, 9*), and suggests suppression of interphase diffusion by an elastic energy barrier. Finally, the total interfacial perimeter decayed following an approximate power law ($\alpha = 0.4 \pm 0.1$, **Figure 3.2D**). This is consistent with late stage growth dominated by either droplet ripening or fusion ($\alpha = ⅓$) (*30, 31*). Both growth mechanisms were clearly discernible by time-lapse microscopy, with aqueous droplet fusion visibly frustrated by the viscoelastic nature of the coacervate.

### 3.3.3 Photobleaching perturbs local phase domain morphology

We envisioned that our fluorescence-based phase visualization strategy might also lend itself to quantifying diffusion during phase separation via fluorescence recovery after photobleaching (FRAP). This technique has been widely used to characterize macromolecular transport within hydrogels (*32, 33*), and we recently applied it to study the mechanism of chain migration in PEP networks below the LCST (*18*). Consistent with our previous study, gels labeled with the associative phase probe $PE_CP$-*fm* (**Supplementary**

**Figure 3.3**) showed steady fluorescence recovery at 25 °C, implying diffusive chain migration through the network (**Figure 3.3A**).

In contrast to this simple diffusive behavior, the fluorescence recovery behavior of gels photobleached near the phase boundary was highly anomalous. During phase separation onset at 40 °C, photobleaching clearly perturbed the local domain structure, tending to induce the formation of thin coacervate spines around the bleach spot (**Figure 3.3A**). The rate of fluorescence recovery during the early stage appeared accelerated relative to the late stage (**Figure 3.3B**). Moreover, both the early and late stage recovery profiles were poorly fit by a standard FRAP model that attributes fluorescence recovery to simple diffusion (**Supplementary Figure 3.4**) (*34*).

To explore the origin of the anomalous recovery behavior, we performed photobleaching experiments with two, spectrally independent phase probes. Photobleaching of a green probe ($PE_CP$-*fm*, 490Ex/525Em) triggered diffusion of an unbleached red probe ($PE_CP$-*trm*, 596Ex/615Em) into the bleach spot (**Supplementary Figure 3.3A**). Fluorescein and rhodamine-based dyes are known to readily generate singlet oxygen (*35, 36*), a highly reactive oxygen species that that rapidly crosslinks proteins (*37-39*). We observed that prolonged irradiation of labeled gels promoted oxidative crosslinking of PEP chains *in situ* (**Supplementary Figure 3.3B**). Crosslinking and bleach spot enrichment were completely suppressed by sodium azide, a strong singlet oxygen quencher. Taken together, these results implicate mild oxidative crosslinking by photobleaching as the origin of the anomalous recovery behavior. Our cloud-point measurements (**Supplementary Figure 3.2**

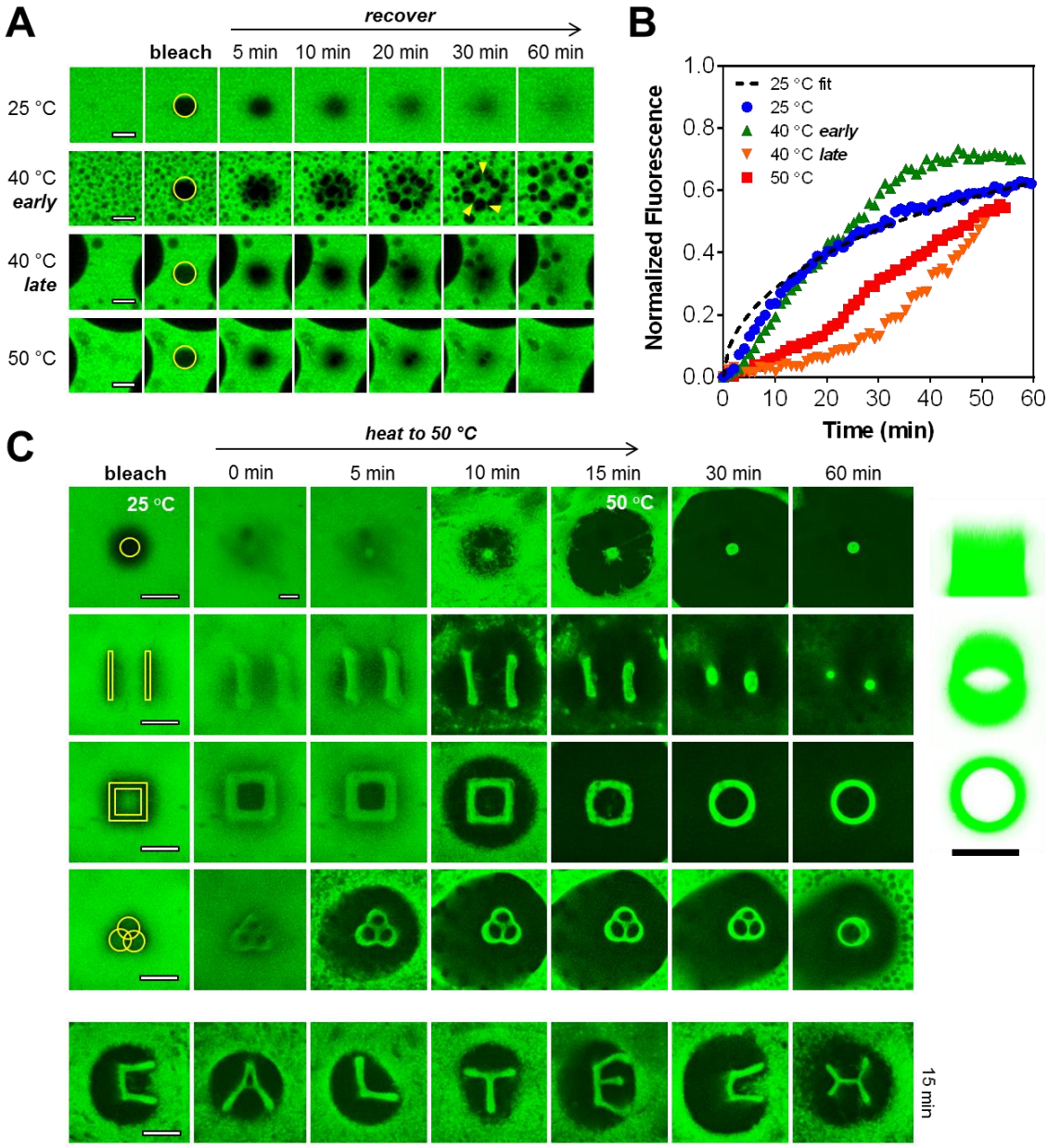


**Figure 3.3. Photobleaching enables patterning of dynamic phase shapes during phase separation onset**. (**A**) Fluorescence recovery after photobleaching (FRAP) was monitored in 10% gels at temperatures below (25 °C) and above (≥ 40 °C) the phase transition temperature (LCST). Photobleaching perturbed local domain structure in gels recently heated to this temperature (40 °C *early*, 30 min). Scale bars = 20 μm. (**B**) Anomalous fluorescence recovery behavior above 40 °C. (**C**) Heating of 5% gels after photobleaching matured the photobleached regions into dynamic

coacervate domains. The patterned domains evolved under the control of interfacial tension and a quickly relaxing mechanical stress, gradually producing (equilibrium) cylindrical and droplet phase architectures. Scale bars = 100 μm.

---

and **Figure 3.1B**) argue that crosslinked chains can have a depressed LCST (*19*). Crosslinking by photobleaching is apparently sufficient to trigger a local phase change below the global phase transition temperature, with subsequent chain enrichment in the bleach spot in order to equalize the chemical potential at the bleach spot boundary.

Photobleaching prior to the onset of phase separation had a pronounced effect on the local phase domain morphology (**Figure 3.3C**). After a brief recovery period, heating to 50 °C induced early maturation of the bleach spots into patterned coacervate domains. Rapid contraction of the global coacervate above the network LCST then caused viscoelastic tearing around the bleach spot, which isolated the patterns in a wide depletion zone. During this period, the patterns behaved as soft elastic bodies and appeared stretched by a radially symmetric stress that pulled them towards the receding coacervate boundary. This tended to create non-equilibrium coacervate structures exhibiting mild distension along concentric lines (e.g., the equiangular vertices of a photobleached “H” character). Ongoing stress relaxation and volume shrinking subsequently collapsed the patterns into symmetrical droplet and cylindrical structures that were gradually absorbed by the global coacervate.

### 3.4 Conclusion

We programmed an artificial protein hydrogel with viscoelastic phase behavior. The ability of the network to both store and dissipate mechanical stress induces unusual sponge-like

phase patterns, and causes a breakdown in the scale invariance of the phase decomposition. Pattern evolution is governed by a delicate balance of surface tension and viscoelastic stress, and mild oxidative crosslinking can perturb this balance in a striking manner. In light of the ability to tune the stress relaxation dynamics of artificial protein networks using protein engineering (*40*), it will be interesting to explore the extent to which such patterning can be further controlled by changes to protein sequence.

### 3.5 Acknowledgements

The assistance of Andres Collazo of the Beckman Imaging Center at the California Institute of Technology is gratefully acknowledged. We also thank Cole DeForest, John Bagert, and Kai Yuet for helpful discussions during the preparation of this chapter. Support from the NSF is also very gratefully acknowledged.

## 3.6 Supporting Information

### 3.6.1 Materials and Methods

**Protein expression and purification.** Plasmids encoding the artificial proteins were transformed into BL21 or BL21 (DE3) chemically competent *E. coli*. After overnight culture, cells were inoculated (inoculation ratios of 1:50 – 1:100) into 1 L flasks containing Terrific Broth (TB) supplemented with 100 – 200 mg $ml^{-1}$ ampicillin. Cells were grown to an $OD_{600}$ of 0.8 – 1.0 and then induced with 1 mM final concentration of isopropyl β-D-1 thiogalactopyranoside (IPTG). After 4-5 h, bacterial cultures were harvested by centrifugation for 5-10 min at 10,000*g*, followed by lysis with 8 M urea. Cell lysates were freeze-thawed at least once before being subject to high-power tip sonication for homogenization (50 mL of lysate from a 1 L culture was typically treated with 30 – 50 W for 10 min in 0.5 s pulses). Homogenized lysate was clarified by high-speed centrifugation (>30,000*g* for 1 h) and then subject to standard His-tag purification over Ni-NTA agarose beads (Qiagen) under denaturing conditions (8 M urea).

**Protein dialysis and refolding.** Denatured, His-purified protein (50 – 100 mL in 8M urea and phosphate buffer) was dialyzed against 4 L of distilled water at 4 °C. The water was changed repeatedly (5 – 6X) over the course of several days. Typically, protein precipitation within the dialysate was used as the dialysis endpoint, after which point the aqueous suspensions were lyophilized. This procedure routinely gave gels that displayed cloud points near 40 °C (cf. **Figure 3.1C**). However, subtle changes to the refolding procedure (e.g. changes in dialysis temperature, buffer identity or exchange rate) could significantly shift

this transition temperature. A slow buffer exchange rate starting in urea and phosphate buffer could depress the LCST to below 25 °C. Fast dialysis starting in urea and Tris buffer made the temperature transition undetectable by turbidimetry. We infer that our observed LCST is not a simple function of elastin sequence E, but depends strongly on the folded state of the P endblocks, and on their interactions with E.

**Hydrogel preparation.** 100 mM phosphate buffer (pH 6.5 – 7.4) was added to lyophilized PEP protein and the suspension was placed on ice for 2 – 4 h to promote gelation. Fluorescent hydrogels were prepared by adding low concentrations of labeled $PE_CP$ to normal PEP networks (typically, $PE_CP$:PEP mass ratios of 1:50 and 1:100 were used). Dye conjugation to cysteine-containing probes was performed as described previously (*18*).

**Rheological analysis of gels.** Oscillatory shear rheology was performed on 10% (*w*/*v*) PEP hydrogels using an ARES-RFS strain-controlled rheometer (TA Instruments) equipped with a cone-and-plate geometry. The outer edge of the plate was coated with mineral oil in order to minimize evaporation from the exposed gel. Strain sweeps identified a linear regime between 0.1 – 10% strain at 10 rad $s^{-1}$. Frequency sweeps were performed at a fixed strain amplitude of 1% between 0.01 and 100 rad $s^{-1}$. Temperature data was collected at 1% strain and 10 rad $s^{-1}$, at 5 °C intervals between 25 °C and 60 °C.

**Cloud-point measurements.** Protein solutions were prepared at concentrations ranging from 1 to 10% (*w*/*v*) in 100 mM phosphate buffer, pH 6.5 – 7.4. Solutions of PEP above 2 – 3% formed viscoelastic gels, whereas below 2% the solutions flowed easily. Solutions and gels were loaded between the two halves of a disassembled quartz cuvette. The cuvette was

assembled by pressing the two halves together, which sandwiched the gel within a 0.1 cm thick cavity. Roughly 400 $\mu$L of gel was required to fill the cuvette. The absorbance at 650 nm in response to temperature was monitored continuously on a Cary 100 Bio UV-Vis spectrometer equipped with temperature control. Gels were typically heated from 25 °C to 95 °C, held at 95 °C for 5 min, then cooled to 5 °C. The heating and cooling rates were held constant at 1 – 3 °C $min^{-1}$, with minimal differences observed between the faster and slower rates. Prior to cloud-point measurements on the "$E_C$" protein, a 5% solution was placed at 4 °C on a rotator plate for 3 – 4 days to promote oxidative crosslinking of the thiol groups.

### 3.6.2 Development of Phase Patterns

Imaging of spontaneous pattern formation and phase separation in labeled PEP hydrogels was performed on a Zeiss LSM 880 confocal microscope (488 nm with 10 – 20X objectives) equipped with a "Delta T" heated stage programmed to cycle between 25 °C and 50 °C within 60 seconds (Bioptechs, Butler PA). Labeled gels were placed on an ITO-coated, thermally conductive Delta T culture dish and sealed beneath a coverslip using 120 μm Secure-Seal spacers (Life Technologies). Image analysis was performed in MATLAB. FRAP experiments were performed on a Zeiss LSM 880 equipped with a 25 mW Argon laser. Recovery curves were fit to an effective diffusion model using the MATLAB function *nlinfit* (*18, 34*).

Patterning experiments were performed on a Zeiss LSM 5 Exciter equipped with a 25 mW Argon laser (458, 488 and 514 nm) and a 25 mW Diode (405 nm) laser. All laser lines, at maximum power, were typically activated during the photobleach. Bleach spot sizes ranged

from 100 – 2000 μm$^2$. Bleaching of a 500 μm$^2$ ($a$ = 12.5 μm radius) circle at a scan rate of 4 μm s$^{-1}$ required roughly 2000 scans to ensure efficient bleaching of fluorescein. Bleaching of larger spot sizes (2000 μm$^2$, $a$ = 25 μm) was usually performed at a scan rate of 1 μm s$^{-1}$. Typical bleaching times varied from 2 – 10 min, depending on the size of the bleach spot and the total number of scans (2000 – 5000 scans). The total incident power emitted from the Argon laser during a typical fluorescein photobleach was measured to be ~1 mW using a power meter. At 1 mW incident power, the average irradiance (power density) was estimated to be 50 W cm$^{-2}$. After bleaching of the desired pattern, the sample was allowed to recover for 15 – 30 min. Gels were then slowly heated to 50 °C at rate of 2 – 3 °C min$^{-1}$ using a standard heated stage and an aluminum coverslip mount.

**Oxidative crosslinking studies.** Gels were prepared at 5% in 100 mM phosphate buffer pH 7, supplemented with 25 $\mu$M free fluorescein or Rose Bengal, with or without 100 mM $NaN_3$. Gels were sealed between two coverslips, separated by a 0.030 in sheet of PDMS. Sample irradiation was performed using a Coherent Innova 70 CW Ar-Ion laser. The total incident beam power at 488 nm was fixed at 250 – 300 mW using a circular beam spot with a diameter of roughly 0.8 cm. The irradiance (power density) was estimated to be 0.5 W cm$^{-2}$. Gels were irradiated for 2 h, then solubilized in 8 M urea and crosslinking was assessed by SDS-PAGE under non-reducing conditions.

### 3.6.3 Supplementary Tables

**Supplementary Table 3.1. Plasmids and amino acid sequences of phase programmable proteins.** Protein coding sequences were confirmed by double-stranded DNA sequencing. Each "P" domain is highlighted in blue, and the "E" domain is highlighted in gray. Cysteine residues are highlighted in red.

| Plasmid | Protein | Molecular Weight (Da) |
|---|---|---|
| *pET15b-PEP* | PEP | 32,047 |
| MKGSHHHHHHHVDGSGSGSGSGSGSGAPQMLRELQETNAALQDVRELLRQ QVKEITFLKNTVMESDASGSGSGSGSGSGSGLDGHGVGVPGVGVPGVGVPG EGVPGVGVPGVGVPGVGVPGVGVPGEGVPGVGVPGVGVPGVGVPGVGVPG EGVPGVGVPGVGELYAVTGRGDSPASSAPIATSVPGVGVPGVGVPGEGVPGV GVPGVGVPGVGVPGVGVPGEGVPGVGVPGVGVPGVGVPGVGVPGEGVPGV GVPGVGVPGGLLDGSGSGSGSGSGSGAPQMLRELQETNAALQDVRELLRQQ VKEITFLKNTVMESDASGSGSGSGSGSGLEMHHHHHHK* | | |
| *pET15b-PE$_C$P* | PE$_C$P | 32,151 |
| MKGSHHHHHHHVDGSGSGSGSGSGSGAPQMLRELQETNAALQDVRELLRQ QVKEITFLKNTVMESDASGSGSGSGSGSGSGLDGHGVGVPGVGVPGVGVPG EGVPGVGVPGVGVPGVGVPGVGVPGEGVPGVGVPGVGVPGVGVPGVGVPG EGVPGVGVPGVGELCYAVTGRGDSPASSAPIATSVPGVGVPGVGVPGEGVPG VGVPGVGVPGVGVPGVGVPGEGVPGVGVPGVGVPGVGVPGVGVPGEGVPG VGVPGVGVPGGLLDGSGSGSGSGSGSGAPQMLRELQETNAALQDVRELLRQ QVKEITFLKNTVMESDASGSGSGSGSGSGLEMHHHHHHK* | | |
| *pQE80L-E* | E | 17,670 |
| MKGSSHHHHHHVDGHGVGVPGVGVPGVGVPGEGVPGVGVPGVGVPGVGVP GVGVPGEGVPGVGVPGVGVPGVGVPGVGVPGVGVPGEGVPGVGVPGVGELYAVTG RGDSPASSAPIATSVPGVGVPGVGVPGEGVPGVGVPGVGVPGVGVPGVGVP GEGVPGVGVPGVGVPGVGVPGVGVPGVGVPGEGVPGVGVPGVGVPGVGVPGGLLEWKKM* | | |
| *pQE80L-E$_C$* | E$_C$ | 17,706 |
| MKGSSHHHHHHVDGHGVGVPGVGVPGVGVPGEGVPGVGVPGVGVPGVGVP GVGVPGEGVPGVGVPGVGVPGVGVPGVGVPGVGVPGEGVPGVGVPGVGELYAVTG RGDSPACSAPIATSVPGVGVPGVGVPGEGVPGVGVPGVGVPGVGVPGVGVP GEGVPGVGVPGVGVPGVGVPGVGVPGVGVPGEGVPGVGVPGVGVPGVGVPGGLLEWKKM* | | |

### 3.6.4 Supplementary Figures

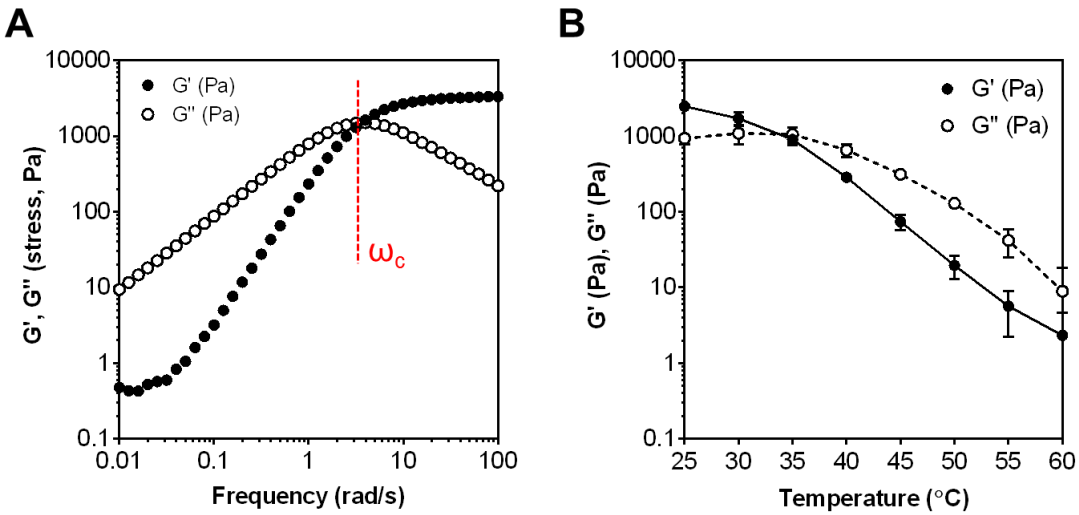


**Supplementary Figure 3.1. Temperature-dependent rheology of PEP hydrogels.** (**A**) Frequency sweep of 10% (*w*/*v*) gels prepared in 100 mM phosphate buffer at a fixed strain amplitude of 1% (25 °C). The network behaves as a viscous liquid at low frequencies ($G' < G''$) but transitions to elastic-dominated behavior at high frequencies ($G' > G''$). This transition occurs at a critical frequency $\omega_c$, corresponding to the dominant stress relaxation mode of the physical network. (**B**) Storage ($G'$) and loss ($G''$) moduli were measured for a 10% gel at 1% strain, 10 rad $s^{-1}$ at various temperatures ($n$ = 2, mean ± SD). Although the viscous loss modulus dominates at high temperatures, weak crosslinking is still evident.

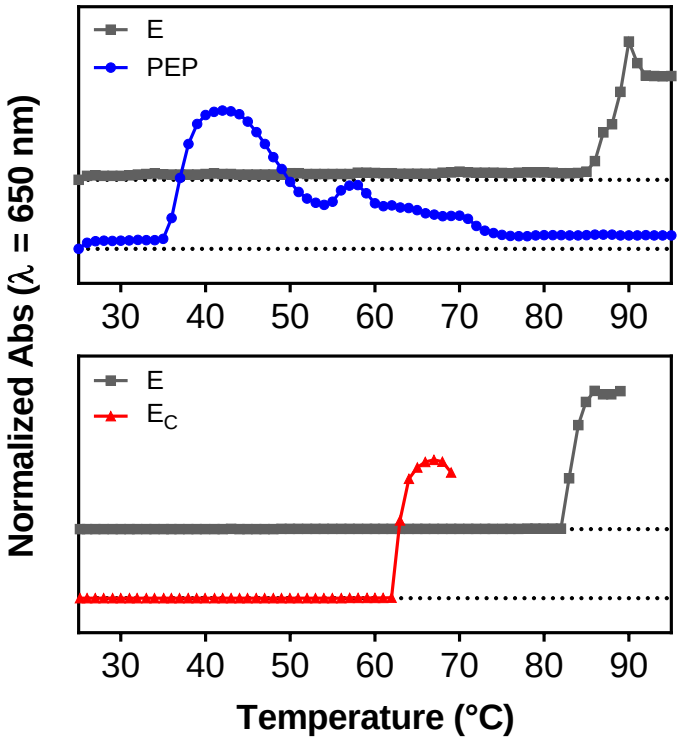


**Supplementary Figure 3.2. Crosslinking affects the LCST of elastin-like proteins.** Proteins were dissolved at a concentration of 5% in 100 mM phosphate buffer (pH 6.5 – 7.4) and heated to 95 °C at a rate 1 °C min$^{-1}$. The onset of turbidity was monitored at 650 nm. (*Top*) The predicted LCST of E based on its repeat sequence (70 °C) is close to its observed transition temperature (80 - 90 °C), whereas the transition temperature of gelled PEP is much lower (38 °C). (*Bottom*) The presence of an oxidized thiol (dimerization) in $E_C$ depresses its LCST by ~20 °C relative to E.

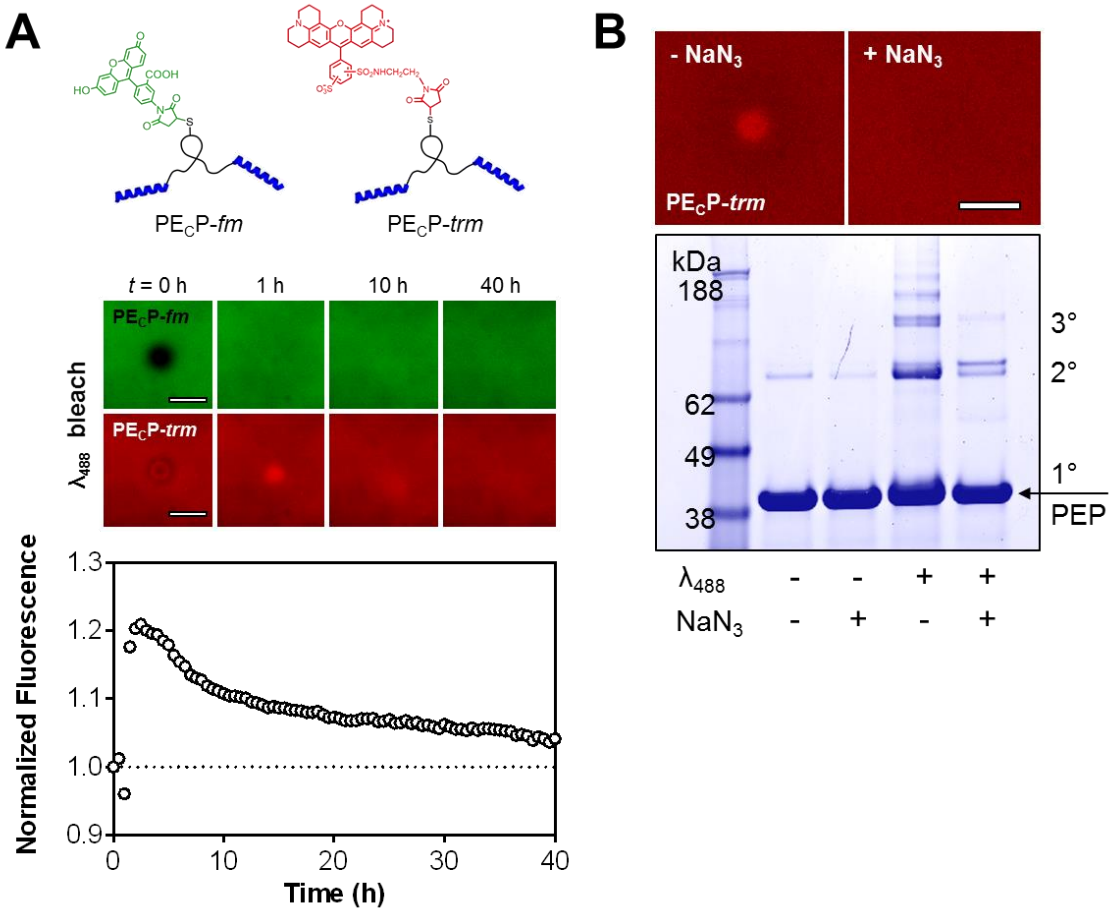


**Supplementary Figure 3.3. Photobleaching promotes covalent interchain crosslinking and subsequent probe enrichment in bleach spots.** (A) 5% gels were labeled with green ($PE_CP$-*fm*, 490Ex/525Em) and red ($PE_CP$-*trm*, 596Ex/615Em) probes and photobleached (spot radius $a$ = 25 µm, $\lambda_{488}$ bleach). Fluorescence recovery was monitored at 25 °C. Red probes diffused into photobleached volumes and remained enriched for several hours. Scale bar = 100 µm. (B) (*Top*) Photobleaching promotes covalent interchain crosslinking by singlet oxygen generation. The presence of 100 mM $NaN_3$, a strong singlet oxygen quencher, prevented probe enrichment in 5% gels labeled with red and green probes ($\lambda_{488}$ bleach). (*Bottom*) Bulk irradiation of 5% gels (488 nm, 500 mW $cm^{-2}$) containing 25 µM free fluorescein promoted covalent multimer formation of PEP chains. Multimerization was suppressed by the presence of 100 mM $NaN_3$. Similar results were obtained with Rose Bengal, a highly efficient singlet oxygen generator, in place of fluorescein. All scale bars = 100 µM.

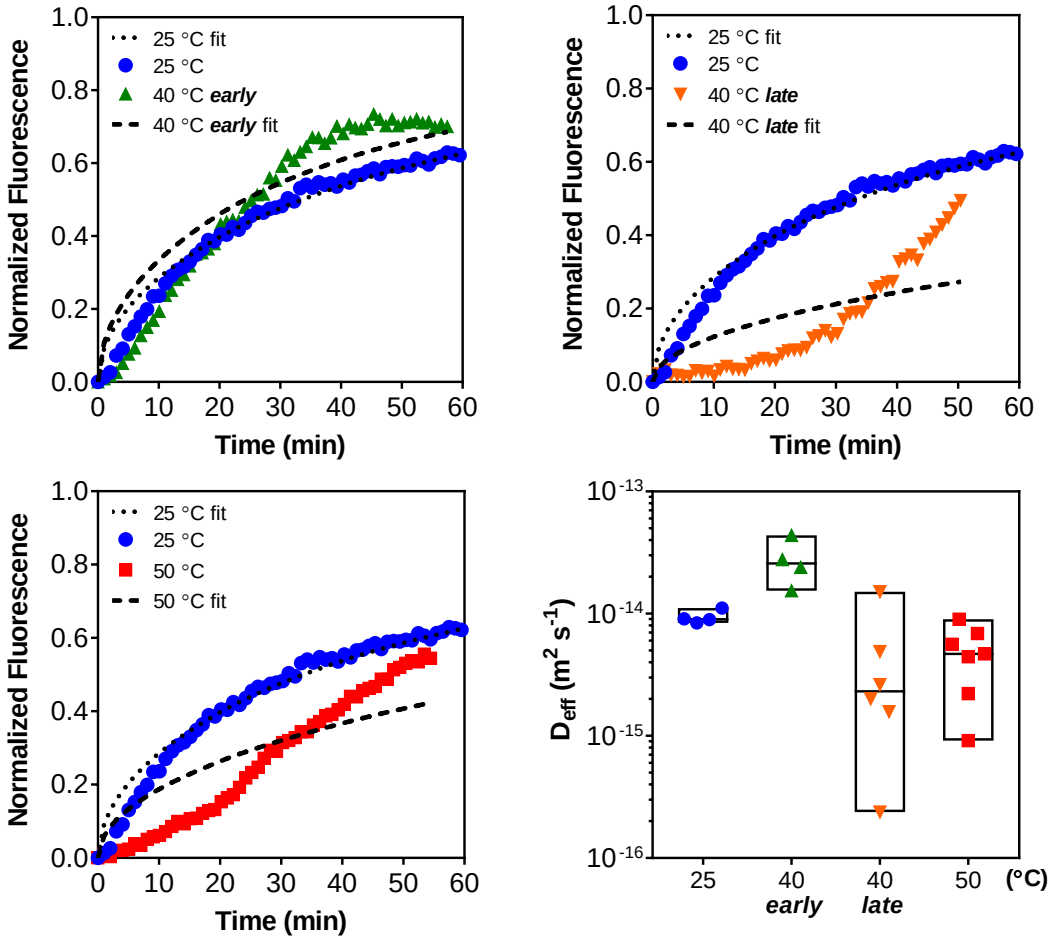


**Supplementary Figure 3.4. Anomalous FRAP behavior above the LCST is poorly fit by standard FRAP models**. Shown are representative FRAP traces acquired in a 10% PEP gel at 40 °C and 50 °C, along with their corresponding fits assuming Fickian diffusion (dashed black lines). Poor fits and the highly heterogenous nature of phase separated samples made reliable determination of the effective diffusion coefficient ($D_{eff}$) difficult.

### 3.7 References and Notes


1. F. S. Bates, Polymer-Polymer Phase-Behavior. *Science* **251**, 898-905 (1991).

2. B. de Boer *et al.*, Supramolecular self-assembly and opto-electronic properties of semiconducting block copolymers. *Polymer* **42**, 9097-9109 (2001).

3. K. Sivula, Z. T. Ball, N. Watanabe, J. M. J. Fréchet, Amphiphilic Diblock Copolymer Compatibilizers and Their Effect on the Morphology and Performance of Polythiophene:Fullerene Solar Cells. *Adv. Mater.* **18**, 206-210 (2006).

4. G. B. Wei, P. X. Ma, Structure and properties of nano-hydroxyapatite/polymer composite scaffolds for bone tissue engineering. *Biomaterials* **25**, 4749-4757 (2004).

5. H. Tanaka, Formation of Network and Cellular Structures by Viscoelastic Phase Separation. *Adv. Mater.* **21**, 1872-1880 (2009).

6. H. Tanaka, Unusual Phase-Separation in a Polymer-Solution Caused by Asymmetric Molecular-Dynamics. *Phys Rev Lett* **71**, 3158-3161 (1993).

7. T. Taniguchi, A. Onuki, Network Domain Structure in Viscoelastic Phase Separation. *Phys Rev Lett* **77**, 4910-4913 (1996).

8. W. W. Mullins, The Statistical Self-Similarity Hypothesis in Grain-Growth and Particle Coarsening. *J Appl Phys* **59**, 1341-1349 (1986).

9. H. Tanaka, Universality of viscoelastic phase separation in dynamically asymmetric fluid mixtures. *Phys Rev Lett* **76**, 787-790 (1996).

10. A. J. Wagner, J. M. Yeomans, Breakdown of Scale Invariance in the Coarsening of Phase-Separating Binary Fluids. *Phys Rev Lett* **80**, 1429-1432 (1998).

11. S. Tanaka, M. Ataka, K. Ito, Pattern formation and coarsening during metastable phase separation in lysozyme solutions. *Phys Rev E* **65**, (2002).

12. H. Tanaka, Y. Nishikawa, Viscoelastic Phase Separation of Protein Solutions. *Phys Rev Lett* **95**, 078103 (2005).

13. T. Hajime, N. Yuya, K. Takehito, Network-forming phase separation of colloidal suspensions. *Journal of Physics: Condensed Matter* **17**, L143 (2005).

14. S. Tanaka *et al.*, Kinetics of phase separation and coarsening in dilute surfactant pentaethylene glycol monododecyl ether solutions. *J Chem Phys* **135**, (2011).

15. V. N. Malashkevich, R. A. Kammerer, V. P. Efimov, T. Schulthess, J. Engel, The crystal structure of a five-stranded coiled coil in COMP: A prototype ion channel? *Science* **274**, 761-765 (1996).

16. L. J. Dooling, M. E. Buck, W. B. Zhang, D. A. Tirrell, Programming Molecular Association and Viscoelastic Behavior in Protein Networks. *Adv Mater* **28**, 4651-4657 (2016).

17. B. D. Olsen, J. A. Kornfield, D. A. Tirrell, Yielding Behavior in Injectable Hydrogels from Telechelic Proteins. *Macromolecules* **43**, 9094-9099 (2010).

18. P. B. Rapp *et al.*, Analysis and Control of Chain Mobility in Protein Hydrogels. *J. Am. Chem. Soc.* **139**, 3796-3804 (2017).

19. D. E. Meyer, A. Chilkoti, Quantification of the effects of chain length and concentration on the thermal behavior of elastin-like polypeptides. *Biomacromolecules* **5**, 846-851 (2004).

20. R. A. McMillan, V. P. Conticello, Synthesis and characterization of elastin-mimetic protein gels derived from a well-defined polypeptide precursor. *Macromolecules* **33**, 4809-4821 (2000).

21. D. W. Urry, Physical Chemistry of Biological Free Energy Transduction As Demonstrated by Elastic Protein-Based Polymers. *The Journal of Physical Chemistry B* **101**, 11007-11028 (1997).

22. Subtle changes to the refolding procedure employed during protein purification could significantly shift this first transition temperature (see Materials and Methods). We take this as further evidence that the LCST depends on the crosslinked state.

23. T. Luo, K. L. Kiick, Noncovalent Modulation of the Inverse Temperature Transition and Self-Assembly of Elastin-b-Collagen-like Peptide Bioconjugates. *J. Am. Chem. Soc.* **137**, 15362-15365 (2015).

24. F. G. Quiroz, A. Chilkoti, Sequence heuristics to encode phase behaviour in intrinsically disordered protein polymers. *Nat Mater* **14**, 1164-1171 (2015).

25. J. S. Haghpanah *et al.*, Artificial Protein Block Copolymers Blocks Comprising Two Distinct Self-Assembling Domains. *ChemBioChem* **10**, 2733-2735 (2009).

26. C. B. Qian, S. J. Mumby, B. E. Eichinger, Phase-Diagrams of Binary Polymer-Solutions and Blends. *Macromolecules* **24**, 1655-1661 (1991).

27. E. L. Cheluget, M. E. Weber, J. H. Vera, Modifications of the Flory-Huggins-Goldstein Model for Accurate Description of Closed-Loop Phase-Diagrams. *Chem Eng Sci* **48**, 1415-1426 (1993).

28. S. K. Gunasekar *et al.*, N-Terminal Aliphatic Residues Dictate the Structure, Stability, Assembly, and Small Molecule Binding of the Coiled-Coil Region of Cartilage Oligomeric Matrix Protein. *Biochemistry* **48**, 8559-8567 (2009).

29. H. Tanaka, T. Araki, T. Koyama, Y. Nishikawa, Universality of viscoelastic phase separation in soft matter. *J Phys-Condens Mat* **17**, S3195-S3204 (2005).

30. H. Tanaka, Viscoelastic phase separation. *J Phys-Condens Mat* **12**, R207-R264 (2000).

31. S.-W. Song, J. M. Torkelson, Coarsening Effects on Microstructure Formation in Isopycnic Polymer Solutions and Membranes Produced via Thermally Induced Phase Separation. *Macromolecules* **27**, 6389-6397 (1994).

32. Y. A. Li *et al.*, Mobility of lysozyme inside oxidized starch polymer microgels. *Soft Matter* **7**, 1926-1935 (2011).

33. P. Gribbon, T. E. Hardingham, Macromolecular diffusion of biological polymers measured by confocal fluorescence recovery after photobleaching. *Biophys J* **75**, 1032-1039 (1998).

34. B. L. Sprague, R. L. Pego, D. A. Stavreva, J. G. McNally, Analysis of binding reactions by fluorescence recovery after photobleaching. *Biophys J* **86**, 3473-3495 (2004).

35. A. K. Gaigalas, L. Wang, K. D. Cole, E. Humphries, Photodegradation of fluorescein in solutions containing n-propyl gallate. *J Phys Chem A* **108**, 4378-4384 (2004).

36. F. Stracke, M. Heupel, E. Thiel, Singlet molecular oxygen photosensitized by Rhodamine dyes: correlation with photophysical properties of the sensitizers. *J Photochem Photobiol A* **126**, 51-58 (1999).

37. H. R. Shen, J. D. Spikes, P. Kopeckova, J. Kopecek, Photodynamic crosslinking of proteins .2. Photocrosslinking of a model protein-ribonuclease A. *J Photochem Photobiol B* **35**, 213-219 (1996).

38. M. P. Sheetz, D. E. Koppel, Membrane Damage Caused by Irradiation of Fluorescent Concanavalin-A. *Proc Natl Acad Sci USA* **76**, 3314-3317 (1979).

39. M. J. Davies, Singlet oxygen-mediated damage to proteins and its consequences. *Biochem Bioph Res Co* **305**, 761-770 (2003).

40. L. J. Dooling, D. A. Tirrell, Engineering the Dynamic Properties of Protein Networks through Sequence Variation. *ACS Central Science* **2**, 812-819 (2016).